

The Chemistry of Europa
and Venus, and
Characterization of Earth-
like Exoplanets

Thesis by
Jiazheng Li

In Partial Fulfillment of the Requirements for
the degree of
Doctor of Philosophy

The logo for the California Institute of Technology (Caltech), featuring the word "Caltech" in a bold, orange, sans-serif font.

CALIFORNIA INSTITUTE OF TECHNOLOGY
Pasadena, California

2022
(Defended May 23rd, 2022)

© 2022

Jiazheng Li

ORCID: 0000-0002-2563-6289

ACKNOWLEDGEMENTS

I would like to thank my advisor Prof. Yuk Yung for bringing me to the beautiful path of planetary science. He is a great advisor, who is always patient and supportive. I not only learnt science from him, but also the philosophy of life.

I would also like to thank my thesis advisory committee, Prof. Andy Ingersoll, Prof. Katherine de Kleer, and Prof. Mike Brown for their great comments and suggestions.

I also want to thank everyone who has been or currently is in Yuk's army including Siteng, Tianhao, Pushkar, Yangcheng, Danica, Stuart, Run-Lie, Zhao-Cheng, Yuan, etc. They have created a great environment for me and provided me with great help on my research.

I would also like to thank all my collaborators including Dr. Murthy Gudipati, Dr. Jonathan Jiang, Dr. Renyu Hu, Dr. Vijay Natraj, Prof. Dorian Abbot, Prof. Joe Pinto, etc. They are of vital importance to the work in this thesis.

Finally, I would like to thank my wife, Shaoshuang Yang. I could not have achieved any of these without her.

ABSTRACT

This thesis contains three parts of work, including oxidant sources on Europa, sulfur chemistry on Venus, and the characterization of Earth-like exoplanets. In the first part, we build two chemical-transport models to study the various oxidant-generation processes that occur in both Europa's atmosphere and surface ice. The atmospheric model focuses on the role that water plumes play in the formation of Europa's ionosphere. The simulation results, which show that the ionization reactions are initiated by electron-impact ionization and photoionization of water and continued by charge transfer between water and oxygen molecules, have successfully reproduced the observations. This model has also been used to study the dissociation processes of water molecules from the plumes, which can be regarded as an alternative source for the oxygen in the atmosphere. The chemical-transport model on Europa's surface ice is built to simulate chemical processes occurring in the ice during irradiation by electrons and to describe how the chemical species of interest (oxidants) are formed, transported, and distributed in the ice. This model also has implications for the chemical composition of Europa's subsurface ocean. Since the availability of oxidants could be the limiting factor for biologically useful chemical energy on Europa, the proposed research may give us insight into Europa's habitability.

The second part of this thesis focuses on the unknown ultraviolet (UV) absorber(s) in the atmosphere of Venus. Ever since the detection of the enigmatic ultraviolet absorption in the upper atmosphere of Venus, questions have been raised about the identity of the unknown UV-visible absorber(s) and how it is formed on Venus. Our recent photochemical modelling study suggests that SO dimers may not be the major UV absorber(s) in Venus' upper atmosphere. However, SO dimers are important intermediaries in the formation of more complex S species (e.g., S_n ($n = 1$ to 7)). Polysulfur aerosol, which is formed from the nucleation process of S_n ($n = 1$ to 7), is a possible candidate for the unknown UV absorber(s). In this work, we compute that the mixing ratio of polysulfur aerosol is $\sim 1.76 \times 10^{-14}$ in the upper atmosphere. By putting the polysulfur aerosol into the Spectral Mapping Atmospheric Radiative Transfer model (SMART), we find that the simulated spectrum of Venus agrees

well with the observations. This result provides useful constraints for unraveling the identity(ies) of the unknown UV-visible absorber(s) on Venus.

The third part of this thesis is devoted to the characterization of Earth-like exoplanets. In this part, we study the glints, a possible phenomenon on Earth-like exoplanets and the rotation period detection for Earth-like exoplanets. Small flashes of reflected light—called glints—are found in images taken by spacecraft observing the Earth and occur due to specularly reflected solar radiation. These glints have been found over both ocean and land. Using Deep Space Climate Observatory observations, we show that glints over land are due to specular reflection off horizontally oriented ice platelets floating in the air, while glints over ocean have contributions from reflection off either platelets floating above the ocean or a relatively smooth ocean surface. We use a radiative transfer model to simulate different kinds of glints and to explore their properties. This technique of comparing observations of terrestrial glints with model simulations may provide new information relevant to atmospheric dynamics and the search for habitable exoplanets. A terrestrial planet's rotation period is one of the key parameters that determines its climate and habitability. Here we demonstrate that, under certain conditions, the rotation period of an Earth-like exoplanet will be detectable using direct-imaging techniques. We use a global climate model that includes clouds to simulate reflected starlight from an Earth-like exoplanet and show that the rotation period of an Earth-like exoplanet is detectable using visible-wavelength channels with time-series monitoring at a signal-to-noise ratio (S/N) >20 with ~ 5 – 15 rotation periods of data, while the rotation period of a planet with full ocean coverage is unlikely to be detectable. To better detect the rotation period, one needs to plan the observation so that each individual integration would yield a S/N >10 , while keeping the integration time shorter than $1/6$ to $1/4$ of the rotation period of the planet. Our results provide important guidance for rotation period detection of Earth-like exoplanets in reflected light using future space telescopes.

PUBLISHED CONTENT AND CONTRIBUTIONS

1. Li, J. Z., Fan, S., Kopparla, P., Liu, C., Jiang, J. H., Natraj, V., & Yung, Y. L. (2019). Study of terrestrial glints based on DSCOVR observations. *Earth and Space Science*, 6(1), 166-173. <https://doi.org/10.1029/2018EA000509>.

J. L. participated in the conception of the project, processed the observational data, set up the model runs, analyzed the results, and wrote the manuscript.

2. Li, J., Gudipati, M. S., & Yung, Y. L. (2020). The influence of Europa's plumes on its atmosphere and ionosphere. *Icarus*, 352, 113999. <https://doi.org/10.1016/j.icarus.2020.113999>.

J. L. participated in the conception of the project, set up the model runs, analyzed the results and wrote the manuscript.

3. Li, J., Jiang, J. H., Yang, H., Abbot, D. S., Hu, R., Komacek, T. D., ... & Yung, Y. L. (2021). Rotation period detection for Earth-like exoplanets. *The Astronomical Journal*, 163(1), 27. <https://doi.org/10.3847/1538-3881/ac36ce>.

J. L. participated in the conception of the project, analyzed the results, and wrote the manuscript.

4. Li, J., Gudipati, M. S., Mishra, Y. N., Liang, M. C., & Yung, Y. L. (2022). Oxidant generation in the ice under electron irradiation: Simulation and application to Europa. *Icarus*, 373, 114760. <https://doi.org/10.1016/j.icarus.2021.114760>.

J. L. participated in the conception of the project, set up the model runs, analyzed the results, and wrote the manuscript.

TABLE OF CONTENTS

Acknowledgements.....	iii
Abstract	iv
Published Content and Contributions.....	vi
Table of Contents.....	vii
List of Illustrations.....	ix
Nomenclature.....	xiii
Part 1. Oxidant Sources on Europa	1
Chapter I: The influence of Europa’s Plumes on its Atmosphere and Ionosphere	2
1.1 Abstract.....	2
1.2 Introduction	3
1.3 Model Description.....	5
1.4 Simulation Results.....	8
1.5 Summary and Discussion.....	11
1.6 Acknowledgements	14
Chapter II: Oxidant Generation in the Ice Under Electron Irradiation: Simulation and Application to Europa.....	19
2.1 Abstract.....	19
2.2 Introduction	20
2.3 Model Setup.....	22
2.4 Simulation Results.....	27
2.5 Discussion and Future Studies	32
2.6 Conclusions and Applications to Europa.....	36
2.7 Acknowledgements	38
Part 2. Sulfur Chemistry on Venus.....	45
Chapter III: A Possible Candidate of the Enigmatic Ultraviolet Absorber(s) in the Upper Atmosphere of Venus.....	46
3.1 Abstract.....	46
3.2 Introduction	46
3.3 Methods	47
3.4 Results and Discussion.....	49
Part 3. Characterization of Earth-like Exoplanets.....	53
Chapter IV: Study of Terrestrial Glints Based on DSCOVR Observations	54
4.1 Abstract.....	54
4.2 Introduction	54
4.3 Glint Mechanism	55
4.4 Observations	57
4.5 Simulations	61
4.6 Summary and Discussion.....	64
4.7 Acknowledgements	66

Chapter V: Rotation Period Detection for Earth-like Exoplanets	69
5.1 Abstract.....	69
5.2 Introduction	70
5.3 ExoCAM GCM	72
5.4 Deriving the Rotation Period from Reflected Light Time Series	73
5.5 Sensitivity of the Detectability of the Rotation Period to Parameters .	76
5.5.1 Length of Observation.....	77
5.5.2 Rotation Period.....	77
5.5.3 Wavelength.....	78
5.5.4 Orbital Geometries	79
5.5.5 Time Resolution	79
5.5.6 Observational Error	80
5.5.7 Land Fraction.....	81
5.6 Conclusion and Discussion	81
5.7 Acknowledgements	85

LIST OF ILLUSTRATIONS

<i>Number</i>	<i>Page</i>
1.1 Density profiles of the major neutral species in the background (solid line) and plume-controlled (dashed lines) atmosphere.....	9
1.2 Density profiles of the major ionized species in the background (solid green line) and plume-controlled (dashed lines) atmosphere. One of the Galileo ionosphere observations is shown as the solid black line. ..	9
1.3 Reaction rate profiles of the major reactions in the plume-controlled atmosphere. H ₂ O-related reactions are shown in dashed lines and non-H ₂ O-related reactions are shown in solid lines. The reaction numbers (refer to Table 1) are written right next to the lines.	12
1.4 Comparison of the major neutral species between the background and plume-controlled atmosphere with different water column densities (the R in the legend represents a water column density of 1.5×10^{16} cm ⁻²).	13
1.5 Comparison of the major ionized species between the background and plume-controlled atmosphere with different water column densities (the R in the legend represents a water column density of 1.5×10^{16} cm ⁻²).	14
2.1 Calculations of the water dissociation. (a) The fraction of 10 keV electrons that penetrate a given depth. (b) The profile of the water dissociation rate in the ice shell.....	24
2.2 Density profiles of radiolytically produced species in water ice at 100 K upon 10 keV electron irradiation at 1.2×10^{12} electrons/cm ² /s flux.	28
2.3 The profiles of the reaction rates of the production (solid curve) and destruction (dashed) reactions related to H ₂ O ₂	29
2.4 The profiles of the reaction rates of the production (solid curves) and	

destruction (dashed) reactions related to O ₂	30
2.5 The profiles of the reaction rates of the production (solid curves) and destruction (dashed) reactions related to O ₃	31
2.6 Sensitivity tests of the upper boundary conditions. The solid lines represent the original run. The dashed lines represent the run with fixed-density upper boundary conditions adjusted upward by a factor of 5 while the dotted lines represent the upper boundary conditions adjusted downward by a factor of 5.	31
2.7 Sensitivity tests of the rate coefficients. The solid lines represent the original run. The dashed lines represent the run with rate coefficients adjusted upward by a factor of 10 while the dotted lines represent the rate coefficients adjusted downward by a factor of 10.....	32
2.8 Density profiles of all the chemical species in the simplified 1D-model representing 10 keV electron bombardment of Europa's water-ice surface. The depth is expanded from 5 μm to 1 m compared to Figure 2.2.	36
3.1 The profiles of the nucleation rate of S _n (n = 1 to 7) and the total transforming rate of elemental sulfur to polysulfur aerosol.....	48
3.2 The properties of the polysulfur aerosol in Venus' atmosphere. (a) The mixing ratio profile of polysulfur aerosol. (b) The absorption cross section spectrum of polysulfur aerosol.....	49
3.3 The spectrum of the atmosphere of Venus with 5 cases of UV absorber(s): (1) no unknown UV absorber(s); (2) the retrieved UV absorber(s) from Haus et al. (2015); (3) our estimated polysulfur aerosol; (4) polysulfur aerosol with the mixing ratio twice of the estimation; (5) polysulfur aerosol with the mixing ratio one twice of the estimation.	50
4.1 An illustration of the glint mechanism for (a) horizontal and (b) tilted reflecting materials. The small yellow circle represents the sun, the large blue circle is the Earth and the small brown rectangle represents	

the vehicle. The black dashed lines show the normal directions of the corresponding surfaces and the red solid lines show the rays of light. (c) Global distribution of glints.....	56
4.2 Comparison between SEV and SZA + VZA. (a) Comparison between SEV and SZA + VZA for land glints; (b) Same as (a) but for ocean glints; (c) Difference between SZA + VZA and SEV for land glints; (d) Same as (c), but for ocean glints.....	57
4.3 Spectra of the glints. (a) Spectra of red land glints; (b) Spectra of red ocean glints.	59
4.4 Comparison between SEV and SZA + VZA for two types of glints. (a) Comparison between SEV and SZA + VZA for land-type glints. (b) Same as (a) but for ocean-type glints; (c) Difference between SZA + VZA and SEV for land-type glints; (d) Same as (c), but for ocean-type glints.....	49
4.5 Simulation of glints. (a) An illustration of how pixels with different surface types are dealt with; (b) A virtual image of the Earth; (c) Difference between SZA + VZA and SEV for glints due to ice platelets; (d) Same as (c) but for glints due to ocean waves.	63
5.1 Two divergent sets of orbital geometries used in this study. On the top of each panel, the small diagram shows how we rotate the orbit to obtain different orbital geometries. The diagrams below show the correspondence between the angles and the orbital geometries. (a) The exoplanet is in an azimuthal-rotated edge-on orbit. (b) The exoplanet is in a polar-rotated orbit. The markers next to each diagram represent the orientation of the sunlit disc in the view of the observer.	73
5.2 How we derive the rotation period from a time series. (a) A simulated time series of reflected star light for the 1-day rotation period experiment. (b) The detrended time series. (c) Fourier transform of the detrended time series. (d) Signal-to-noise ratio as a function of period. The red line indicates the signal-to-noise threshold for 99%	

confidence.	76
5.3 The flowchart of the algorithm that is used to determine whether the rotation period of the exoplanet can be detected from a simulated time series.	76
5.4 As Figure 5.2, except the length of the time series is 4 days. The 99% confidence threshold in panel (d) is lower than the threshold in Figure 5.2d due to the shorter time series.	77
5.5 An example of the minimum length of observation needed to detect the rotation period as a function of wavelength. We combine 1- and 2-day period data here (see Section 5.5.2) and use a 99% confidence threshold. The orbital geometry is 180° of the azimuthal-rotated edge-on orbit, the time resolution 12 data points per period, and the observational error is 5%.	78
5.6 The minimum length of observation needed to detect the rotation period as functions of the wavelength and orbital geometry. We combine 1- and 2-day period data here (see Section 5.5.2) and use a 99% confidence threshold. The time resolution is 12 data points per period. The observational error is 5%. (a) Azimuthal-rotated edge-on orbital geometries (see Figure 5.1). (b) Polar-rotated orbital geometries. The color white indicates that the rotation period is not detectable.....	80
5.7 Exploration on time resolution. (a) Same as Figure 5.6a, except that the time resolution is 6 data points per period. (b) Same as Figure 5.6a, except that the time resolution is 4 data points per period. (c) Same as Figure 5.6a, except that the time resolution is 3 data points per period.	82
5.8 Exploration on S/N. (a) Same as Figure 5.6a, except that the S/N is 40. (b) Same as Figure 5.6a, except that the S/N is 10.	83

NOMENCLATURE

Part 1: Oxidant Sources on Europa

*Chapter I*THE INFLUENCE OF EUROPA'S PLUMES ON ITS ATMOSPHERE
AND IONOSPHERE

This chapter is adapted from work previously published as

Li, J., Gudipati, M. S., & Yung, Y. L. (2020). The influence of Europa's plumes on its atmosphere and ionosphere. *Icarus*, 352, 113999. <https://doi.org/10.1016/j.icarus.2020.113999>.

1.1 Abstract

Europa, one of the Galilean satellites, has a tenuous, oxygen-dominated atmosphere that is usually referred to as a collision-less exosphere. Coupled to the neutral atmosphere and in contact with Europa's surface, a tenuous ionosphere exists on Europa, whose presence has been revealed by multiple observations. Such an ionosphere is thought to be produced by solar photoionization and electron-impact ionization of the oxygen in the atmosphere. However, a recent study showed that the maximum ionosphere coincides with intermittent water plume on Europa, suggesting that water plays an important role in the formation of the ionosphere. Based on the assumption of horizontal uniformity in the middle of the plume, we use the Caltech/Jet Propulsion Laboratory one-dimensional KINETICS model to construct profiles of neutral and ionized species near the plume region. The simulation results, which show that the ionization reactions are initiated by water electron-impact ionization and photoionization and continued by charge transfer between water and oxygen molecules, have successfully reproduced the observations. We find that H_2O^+ is the dominant species only above the ionopause. Below the ionopause, the density of H_2O^+ is orders of magnitude lower than the density of O_2^+ , which is the major composition below the ionopause. Our model has also been used to study the dissociation processes of water molecules from the plumes, which can be regarded as an alternative source for the oxygen in the atmosphere.

1.2 Introduction

The atmosphere of Europa, which is tenuous and referred to as an exosphere or a surface boundary-layer atmosphere (Johnson et al., 2002), was first detected by Hall et al. (1995) using Hubble Space Telescope observations. Based on observations of oxygen's electronic excitation emissions, the dominant composition of the atmosphere is proposed to be molecular oxygen (Hall et al., 1995), which has been confirmed by several studies (Hall et al., 1995; Saur et al., 1998; Hansen et al., 2005; Smyth and Marconi, 2006; Roth et al., 2016). Atomic oxygen has also been proposed to be present in Europa's atmosphere with a column density of $4.7 \times 10^{12} \text{ cm}^{-2}$, which is two orders of magnitude lower than the O_2 dominated model (Shemansky et al., 2014). It is generally understood that the primary source of the oxygen in the atmosphere is ion sputtering of Europa's surface ice (Brown et al., 1984; Ip et al., 1996, 1998; Smyth and Marconi, 2006), as Europa is embedded within Jupiter's magnetosphere and experiencing an intense flux of charged particles (H^+ , O^+ , S^+ , e^-).

Using Galileo radio occultation observations, Kliore et al. (1997) found that a tenuous ionosphere exists on Europa. Observations have shown that the maximum electron density of about 10^4 cm^{-3} exists near the surface, which suggests that the ionosphere is in contact with Europa's surface (Kliore et al., 1997; McGrath and Sparks, 2017). The ionosphere is not uniform across Europa's surface, the ionosphere profiles of different sites may vary considerably (McGrath et al. 2009). The maximum ionosphere is found to be geographically coincident with the intermittent water plumes (McGrath and Sparks 2017), which have been detected to exist on Europa by Roth et al. (2014), Sparks et al. (2016), and Jia et al. (2018). This phenomenon implies that the water molecule plays an important role in the formation of Europa's ionosphere through multiple processes: photoionization, electron-impact ionization, charge transfer and a sequence of chemical reactions. Since the water column density is estimated to be $\sim 10^{16}$ to 10^{17} cm^{-2} (Roth et al., 2014; Sparks et al., 2017), the plumes would also result in efficient photolysis and electron-impact dissociation reactions of water molecules.

Based on a 1-D collisional Monte Carlo model, Shematovich and Johnson (2001) present the first simulation of the profile of Europa's tenuous oxygen atmosphere and build connection between the atmospheric composition and the surface source rate of O_2 . In an improved Monte Carlo model, Shematovich et al. (2005) include the surface source of H_2O and simulate the compositions of Europa's atmosphere including O_2 , H_2O , O and OH , which originate from a balance between sources from irradiation of the icy surface and losses induced by the magnetospheric plasma. Using a 2-D Direct Simulation Monte Carlo technique, Smyth and Marconi (2006) study all the water group species in Europa's atmosphere and their contribution to the gas torus. H_2 and O are found to be the major compositions of the torus and their asymmetric distributions near Europa's orbit are simulated (Smyth and Marconi 2006). Other than water group species, the distribution of trace constituents in Europa's atmosphere (e.g. Na , K , SO_2 , CO_2) and their potential implication on Europa's surface composition have been modeled by several studies (Johnson et al., 2002; Leblanc et al., 2002; Cassidy et al., 2009). Except for the regular surface sputtering sources, irregular eruption like the plumes may have huge impact on the local and global atmosphere. A recent study, Teolis et al. (2017) have evaluated the complex density and compositional structure of Europa's global exosphere under the influence of a south pole plume. Their results also provide potential guidance for future spacecraft flyby detections. However, no study has been conducted on the connection between plume and Europa's ionosphere and the influence of the ionized species on Europa's neutral atmosphere is not yet fully understood.

Due to the lack of studies on the ionization, photolysis, and radiolysis of water molecules from Europa's plumes, we focus on analyzing these processes in this paper. Here we use a one-dimensional chemistry-transport model to investigate the influence of the plumes on the formation of Europa's atmosphere and ionosphere and try to enrich our knowledge on the coupling of the ionized and neutral species in Europa's atmosphere.

1.3 Model Description

The model we applied to the atmosphere (ionosphere included) of Europa is the Caltech/JPL chemistry-transport model KINETICS (Allen et al., 1981, Yung & DeMore, 1999), which presented a stable solution for an atmosphere with surface pressures as low as $\sim 10^{-6}$ μbar (Yung & McElroy, 1977) on Ganymede. The details of the mechanism of the model can be found in Gladstone et al. (1996). The one-dimensional KINETICS model used in this study is modified from a more current version presented in Liang et al. (2005). Here we focus on simulating the atmosphere that is in the middle part of a steady plume, where horizontal diffusion of water molecules is assumed to be negligible and the time scale to reach the chemical equilibrium is less than the lifetime of the plume, so the one-dimensional model is suitable for our study. In the model, the atmosphere is divided into 50 layers, from the surface to an altitude of 500 km. The temperature of the atmosphere is set to be 1000 K with a scale height of ~ 200 km (McGrath et al., 2009). The chemical compositions in the modelled atmosphere are oxygen-containing and hydrogen-containing neutral particles and ions, e.g. H, O, O₂, H₂O, O₂⁺, and H₂O⁺. A quasi-neutral atmosphere is assumed in our model, in other words, the electron density always equals to the ion density.

Major chemical reactions and their rate coefficients are listed in Table 1, where minor reactions are not shown. The electron-impact ionization and dissociation reactions are primarily induced by the thermal electrons (temperature ~ 20 eV) from Jupiter's magnetosphere (marked as e* in Table 1) (Johnson et al., 2009). To better model the electron-impact reactions, we consider the existence of the ionopause, which is the position that external plasma flow from magnetosphere cannot further penetrate. Using a 3D hybrid model, Sittler et al. (2013) propose that an ionopause exists on Europa at the altitude of ~ 40 km. Above the ionopause, the density of e* is assumed to be 160 cm^{-3} , which is the median electron density near Europa's environment derived by Bagenal et al. (2015). Below the ionopause, since the plasma flow which carries the magnetospheric thermal electrons stops (Sittler et al., 2013), the density of the thermal electrons is assumed to be 0. Meanwhile, the O₂⁺ and H₂O⁺ that formed above the ionopause will be quickly lost due to the pickup effect

of the plasma flow that has a velocity of ~ 100 km/s. In our model, their lifetimes are set to be 2 seconds. Also, radicals (O, H and OH) from radiolytic and photolytic dissociation of O_2 and H_2O are likely to have kinetic energy of several eVs (Smyth and Marconi, 2006), which is higher than their escape velocity. Therefore, in the model they are assumed to have a 50% escape probability. For the photoionization and photolysis processes, their reaction rates are calculated from a radiative transfer model. Reaction 19, the charge-exchange reaction, describes the major loss mechanism for O_2 in the atmosphere (Lucchetti et al., 2016): a fast O_2^+ exchanges its charge with a slow neutral O_2 during a collision and forms a slow O_2^+ and a fast neutral O_2 , which has approximately the same energy as the original fast O_2^+ . If the original ion has the kinetic energy that is higher than the escape energy of Europa (~ 0.7 eV), the newly formed neutral O_2 will be able to escape the atmosphere. According to Fig.4 in Benyoucef and Yousfi (2014), the rate coefficient of this reaction is estimated to be $\sim 7.5 \times 10^{-10} \text{ cm}^3 \text{ s}^{-1}$. However, only a part of the O_2^+ population has enough energy to complete this process. If the original ion does not have enough energy, this reaction will not change the composition of the atmosphere. Therefore, for the whole O_2^+ population, the rate coefficient of reaction 19 should be lower than $7.5 \times 10^{-10} \text{ cm}^3 \text{ s}^{-1}$. Here we assume that about 10% of the O_2^+ are energetic ones and the rate coefficient is estimated to be $\sim 7.5 \times 10^{-11} \text{ cm}^3 \text{ s}^{-1}$ (please refer to Section 1.5 for rationale for this estimate). The solar flux values are obtained from Mount and Rottman (1983), Torr and Torr (1985), and World Meteorological Organization (1985). Since the values from those references are corresponding to the Earth, which is 1 astronomical unit (AU) from the Sun, the solar flux values at Europa are scaled according to the mean distance between the Sun and Europa, which is ~ 5.2 AU. The solar zenith angle is set as 80° .

Reactions	Rate Coefficients ^a	References ^b
1. $\text{O}_2 + h\nu \rightarrow 2\text{O}$	1.6×10^{-8}	1, 2
2. $\text{O}_2 + h\nu \rightarrow \text{O} + \text{O} (^1\text{D})$	1.1×10^{-8}	1, 2
3. $\text{O}_2 + h\nu \rightarrow \text{O}_2^+ + e^-$	4.1×10^{-9}	2
4. $\text{O}_2 + h\nu \rightarrow \text{O}^+ + \text{O} + e^-$	3.2×10^{-10}	2
5. $\text{O} + h\nu \rightarrow \text{O}^+ + e^-$	7.4×10^{-10}	1, 2
6. $\text{O}^+ + \text{O}_2 \rightarrow \text{O}_2^+ + \text{O}$	1.7×10^{-11}	1, 2
7. $\text{O}^+ + e^- \rightarrow \text{O}$	$1.4 \times 10^{-10} \text{T}^{-0.7}$	1, 2
8. $\text{O}_2^+ + e^- \rightarrow 2\text{O}$	$1.1 \times 10^{-5} \text{T}^{-0.7}$	2, 3
9. $\text{H}_2\text{O} + h\nu \rightarrow \text{H} + \text{OH}$	2.3×10^{-7}	1, 2
10. $\text{H}_2\text{O} + h\nu \rightarrow 2\text{H} + \text{O}$	1.0×10^{-8}	1, 2
11. $\text{OH} + h\nu \rightarrow \text{H} + \text{O}$	3.7×10^{-7}	1
12. $\text{O} + \text{OH} \rightarrow \text{O}_2 + \text{H}$	$2.2 \times 10^{-11} e^{120/\text{T}}$	1, 2
13. $\text{H}_2\text{O} + h\nu \rightarrow \text{H}_2\text{O}^+ + e^-$	3.1×10^{-9}	1, 2
14. $\text{H}_2\text{O}^+ + e^- \rightarrow \text{O} + 2\text{H}$	2.9×10^{-7}	4, 5, 6
15. $\text{H}_2\text{O}^+ + e^- \rightarrow \text{O} + \text{H}_2$	4.7×10^{-8}	4, 5, 6
16. $\text{H}_2\text{O}^+ + e^- \rightarrow \text{OH} + \text{H}$	8.9×10^{-8}	4, 5, 6
17. $2\text{OH} \rightarrow \text{O} + \text{H}_2\text{O}$	$4.2 \times 10^{-12} e^{-240/\text{T}}$	1
18. $\text{H}_2\text{O}^+ + \text{O}_2 \rightarrow \text{O}_2^+ + \text{H}_2\text{O}$	5.0×10^{-9}	7
19. $\text{O}_2^+ + \text{O}_2 \rightarrow \text{O}_2 (\text{escape}) + \text{O}_2^+$	7.5×10^{-11}	estimated
20. $\text{O}_2 + e^* \rightarrow \text{O} + \text{O}$	1.3×10^{-8}	8
21. $\text{O}_2 + e^* \rightarrow \text{O}_2^+ + e^-$	2.4×10^{-8}	8
22. $\text{H}_2\text{O} + e^* \rightarrow \text{OH} + \text{H}$	3.8×10^{-8}	8
23. $\text{H}_2\text{O} + e^* \rightarrow \text{H}_2\text{O}^+ + e^-$	2.3×10^{-8}	8

^aUnits are s^{-1} for photochemical reactions and cm^3s^{-1} for two-body reactions. For photochemical reactions, their reaction rates are calculated from a radiative transfer model, their rate coefficients are given at the top of the model atmosphere.

^bReferences: 1. see references of Moses et al. (2000); 2. see references of Yung and DeMore (1999); 3. Sheehan and St.-Maurice (2004); 4. Datz et al. (2000); 5. Mul et al. (1983); 6. Vejby-Christensen et al. (1997); 7. Le Teuff et al. (2000); 8. Johnson et al. (2009).

Table 1.1. A list of major reactions in our modelled atmosphere, including their rate coefficients and references. In this table, T represents the temperature of the atmosphere. e^- represents the electrons generated locally and e^* represents the thermal electrons from the magnetosphere.

To evaluate the influence of water plume to the atmosphere, we first use KINETICS to construct a background O_2 -dominated atmosphere. For building this background atmosphere, the key boundary condition for the model is the net flux of O_2 at the surface, which represents the intensity of the oxygen source and determines the O_2 concentration in the atmosphere. In this study, the background O_2 column density is set to be $\sim 3.5 \times 10^{14} \text{cm}^{-2}$ (Roth et al., 2014), corresponding to an O_2 surface net flux of $\sim 1.9 \times 10^9 \text{cm}^{-2}\text{s}^{-1}$. Since the

influence of the plume to the intensity of the oxygen source at surface is negligible, we fix the O_2 surface net flux and put water vapor into our model to construct plume-controlled atmosphere. The H_2O column density is set to be $\sim 1.5 \times 10^{16} \text{ cm}^{-2}$ (Roth et al., 2014), which corresponds to an H_2O density of $\sim 2.2 \times 10^9 \text{ cm}^{-3}$ at the surface. Comparing the profiles of neutral and ionized species between the background atmosphere and the plume-controlled atmosphere, we can examine the influence of the plume to Europa's atmosphere.

1.4 Simulation Results

The density profiles of major neutral and ionized constituents in our model are shown in Figure 1.1 and Figure 1.2, respectively. In both figures, each solid line represents the profile of a constituent in the background atmosphere while each dashed line represents the profile of the same constituent in the plume-controlled atmosphere. Figure 1.1 shows that in the plume-controlled atmosphere, H_2O is the dominant species and O_2 becomes a minor species. Compared to the background atmosphere, O_2 density increases by less than a factor of 2, which is consistent with the oxygen observation at the plume region described by Roth et al. (2014), who report no significant increase of O_2 concentration near the plume. As for ionized species, Figure 1.2 shows that in both background and plume-controlled atmosphere, the highest ion density emerges near the surface, suggesting that the ionosphere is in contact with the surface. The surface ion density of the background atmosphere ($\sim 4 \times 10^3 \text{ cm}^{-3}$) is consistent with the minimum surface electron density ($\sim 5 \times 10^3 \text{ cm}^{-3}$) of the average ionosphere profile derived from the Galileo occultation observations (Kliore et al., 1997). In the plume-controlled atmosphere, the O_2^+ is still the dominant ion species but only below 40 km. The ion density at the surface is $\sim 1 \times 10^4 \text{ cm}^{-3}$, which is about a factor of 2.5 larger than the O_2^+ density in the background atmosphere. The shape of the modelled ionosphere profile is in good agreement with one of the maximum ionosphere profiles of Galileo occultation observations (shown as the black line in Figure 1.2), which is detected near a potential plume location (McGrath and Sparks, 2017). Another interesting phenomenon found in our simulated plume-controlled atmosphere is that even though H_2O is the dominant constituent, the H_2O^+ concentration at the lower atmosphere is several orders of magnitude lower than

the O_2^+ concentration. The H_2O^+ becomes the dominant species at higher altitude. The peak of the H_2O^+ concentration, as well as the peak of the total ion density, appear at about 40 km, instead of the surface. After carefully examining the chemical reactions happening in the atmosphere (as discussed below), this phenomenon can be understood.

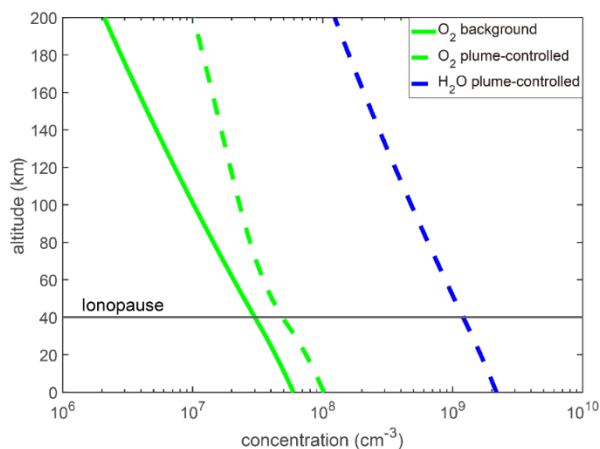


Figure 1.1: Density profiles of the major neutral species in the background (solid line) and plume-controlled (dashed lines) atmosphere.

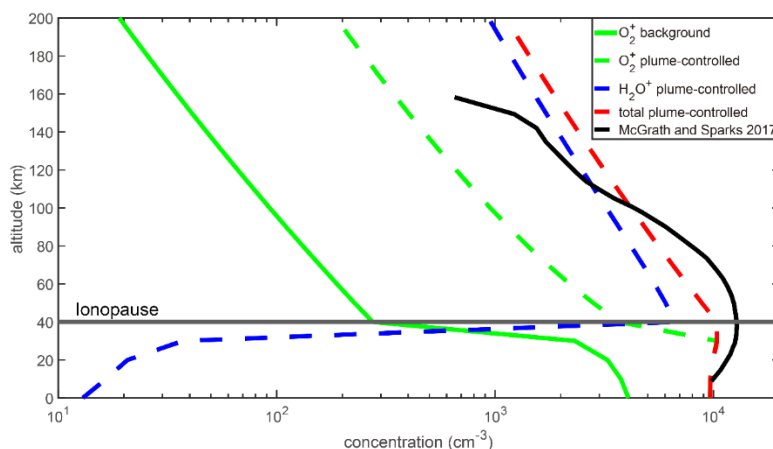


Figure 1.2: Density profiles of the major ionized species in the background (solid green line) and plume-controlled (dashed lines) atmosphere. One of the Galileo ionosphere observations is shown as the solid black line.

Figure 1.3 shows the reaction rate profiles of the most important reactions in the plume-controlled atmosphere. In the higher atmosphere, the electron-impact dissociation and ionization reactions are the dominant reactions for both O_2 and H_2O , whose reaction rates are at least one order of magnitude higher than the rates of photolysis and photoionization.

Photolysis and photoionization only dominate at lower altitude since the density of the magnetospheric thermal electron decrease abruptly at lower altitude. At lower altitude, the charge exchange reaction between H_2O^+ and O_2 (Reaction 18), which is shown as the pink dashed line in Figure 1.3, is the major H_2O^+ loss mechanism. This reaction suggests that the formation of the ionosphere is initiated by water photoionization and continued by charge transfer between water and oxygen molecules. Due to the large O_2 density at the lower atmosphere, the lifetime of the water ion is very short, which explains the existence of the relatively low H_2O^+ concentration at the lower atmosphere. Compared to the O_2 photoionization reaction (Reaction 3, shown as the orange solid line in Figure 1.3), the charge exchange reaction has a much higher reaction rate, which suggests that the charge exchange reaction is also the major O_2^+ production mechanism. At higher altitude, because the ionization rate of H_2O is much higher than the ionization rate of O_2 and the charge exchange reaction is depressed due to the decreasing O_2 concentration, H_2O^+ becomes the dominant ion species. In regard to the formation of oxygen molecules, the water dissociation processes (Reactions 9 and 22, shown as the dashed blue and green lines in Figure 1.3) release a huge amount of OH into the atmosphere and accelerates the oxygen production reaction (Reaction 12, shown as the solid cyan line in Figure 1.3). Although the existence of the plume increases the H_2O^+ and O_2^+ density in the atmosphere, which enhances the O_2 loss through the two charge transfer reactions (Reactions 18 and 19), the O_2 concentration still increases due to the water dissociation processes.

To understand the sensitivity of the atmosphere to the water concentration, we test two more cases with water column density of $\sim 5.0 \times 10^{15} \text{ cm}^{-2}$ and $\sim 4.5 \times 10^{16} \text{ cm}^{-2}$ (one third and three times of the column density derived by Roth et al. (2014)). The results of our sensitivity test are shown in Figure 1.4 and Figure 1.5. The density profiles of the neutral atmosphere show that in the upper atmosphere, the O_2 concentration is positively correlated to the water concentration, although the difference of O_2 concentration between different cases are much less obvious than the difference of water concentration. In the lower atmosphere, the variation of the O_2 concentration is considerably small and insensitive to the variation of the water concentration. The mechanism behind this phenomenon is intuitive: while the

production of O_2 is enhanced (depressed) by the increasing (decreasing) H_2O dissociation, the O_2 loss processes are also enhanced (depressed) by the increasing (decreasing) H_2O ionization, so that the O_2 concentration is not sensitive to different water concentrations. For the ionosphere profiles, we could see that at higher altitude, where the ionosphere is dominated by H_2O^+ ions, the ion density is proportional to the H_2O density. In the case with excess water molecules, the maximum ion density appears at 40km, which is the same as the original case. However, in the lower altitude, both H_2O^+ and O_2^+ densities of this case are lower than the original case. That's because in this case, the water plume is optically thick for the solar radiation so that the water photoionization rate decreases with decreasing altitude near the surface. In the case with less water molecules, because of the lower water concentration compared to the original case, the H_2O^+ density depresses at higher altitude so that the maximum ion density exists at the surface instead of 40km. The comparison between these three cases confirms that the water molecule is the determinant species for the ionosphere profile.

1.5 Summary and Discussion

Ever since the detection of intermittent water plumes on Europa, questions have been raised about the influence that the abrupt emergence of a huge amount of water would have on Europa's neutral atmosphere and ionosphere. In this study, we use the 1D chemical-transport model KINETICS to investigate the role that water vapor plays in Europa's atmosphere. Our simulation results show that the existence of water plume can increase the O_2 concentration by about a factor of 2 due to water dissociation. Meanwhile, plume-generated water molecules are ionized by solar radiation and magnetospheric electrons. Charge transfer happens between oxygen molecules and water ions increases the O_2^+ concentration to about 10^4 cm^{-3} near the surface. The simulated neutral atmosphere and ionosphere are both generally consistent with the observation, which implies the validity of our model.

To set up the background O_2 atmosphere, we choose an O_2 surface net flux in order to fit the observed atmosphere column density. The O_2 surface net flux, which represents how many oxygen molecules are formed at the surface by ion sputtering processes, has been studied

even before the detection of Europa's atmosphere (Johnson, 1990; Ip et al., 1998; Shematovich et al., 2005; Smyth and Marconi, 2006; Oza et al., 2018; Vorburger & Wurz, 2018). However, due to the lack of information about microscopic structure of surface ice and incoming ions, the intensity of the oxygen source at the surface is poorly constrained. Additionally, electrons, secondary electrons and photons produced by the incoming electrons (Gudipati et al., 2017) can penetrate into the surface ice, dissociate water molecules and produce radicals (H, O, OH) inside the ice. These radicals can induce further chemical reactions inside the ice and form extra O_2 which can diffuse out of the ice and form a part of the neutral atmosphere, providing us a second source of the oxygen other than the ion sputtering. Since the gravitational field of Europa is relatively weak, the oxygen atoms/molecules produced by ion sputtering are likely to escape into the magnetosphere, therefore the diffusion from the subsurface ice may be a stronger oxygen source than the ion sputtering. To the best of our knowledge, we are not aware of any published laboratory measurements that have quantified the emission of radicals (H, O, OH) from ice under radiolysis. Studies on the oxygen-generation-related physical and chemical processes inside the ice are needed in the future to better constrain our modelling work on atmosphere.

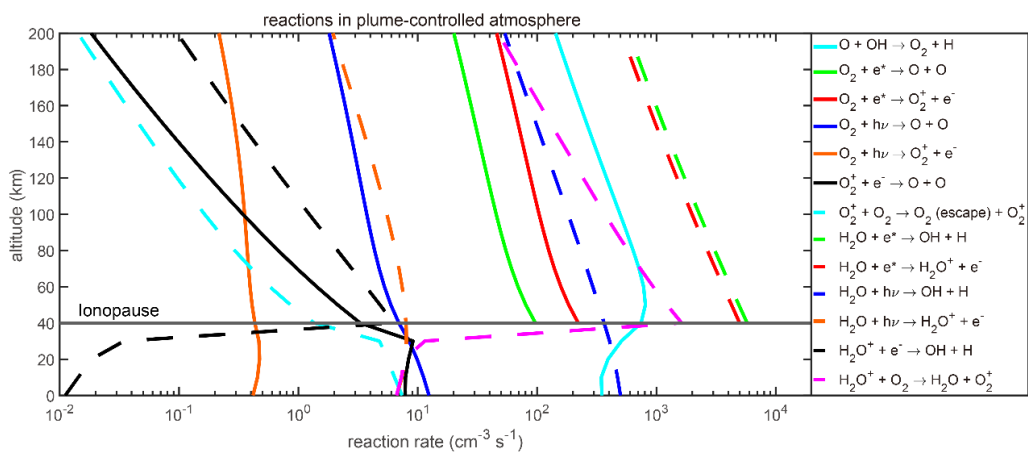


Figure 1.3: Reaction rate profiles of the major reactions in the plume-controlled atmosphere. H_2O -related reactions are shown in dashed lines and non- H_2O -related reactions are shown in solid lines. The reaction numbers (refer to Table 1) are written right next to the lines.

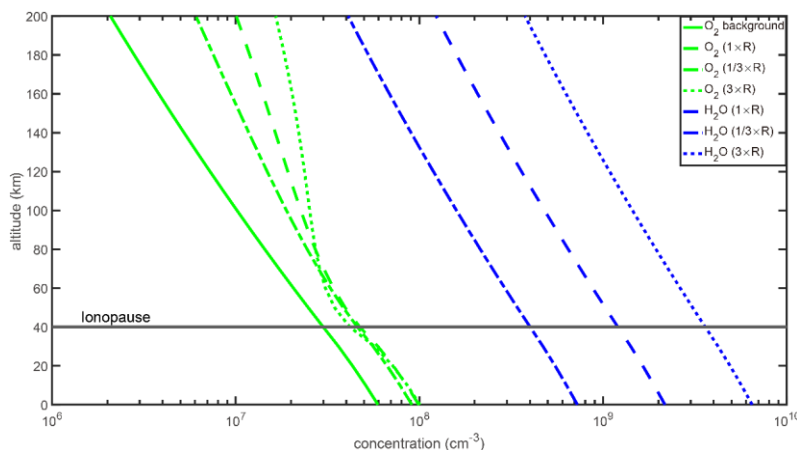


Figure 1.4: Comparison of the major neutral species between the background and plume-controlled atmosphere with different water column densities (the R in the legend represents a water column density of $1.5 \times 10^{16} \text{ cm}^{-2}$).

Even though the simulation results agree well with the observations, further investigations are needed to improve our model. Reaction 19, the major O_2 loss mechanism, is an important reaction in our model. Because O_2^+ is formed in the atmosphere and subsequently accelerated in the local fields of Europa (Sittler et al., 2013; Lucchetti et al., 2016) and only a part of these ions attains escape energy of 0.7 eV. While we do not have any better estimates of O_2^+ velocity distribution near the surface, we take these studies as starting assumptions, based on which we estimate that about 10% of the O_2^+ are energetic enough for charge exchange driven O_2 escape from the atmosphere, hence the rate coefficient of reaction 19 in Table 1 is assumed to be $\sim 7.5 \times 10^{-11} \text{ cm}^3 \text{ s}^{-1}$. Since this rate coefficient is strongly related to the energy distribution of O_2^+ , which is unknown and probably changes with altitude, our rate coefficient estimation might be different from the real value. However, we have tested different values for the O_2 escape efficiency (1%, 10%, and 100%) and found that the influence of this rate on the overall O_2 and O_2^+ budget in the atmosphere of Europa is limited. Also, the sticking of radicals like OH, O and H on Europa's surface is not considered in our model. Although there is no evidence that those radicals have high sticking coefficients on water ice, we should not exclude this possibility. If those radicals would stick effectively on the surface, their concentration on the atmosphere will be significantly depressed so that they will react on the surface rather than in the atmosphere. Despite the fact that our model is oversimplified in some aspects, our results successfully fit the previous Europa observations and show the

interpretational power of the model. Future work considering those issues will help us build a more realistic model.

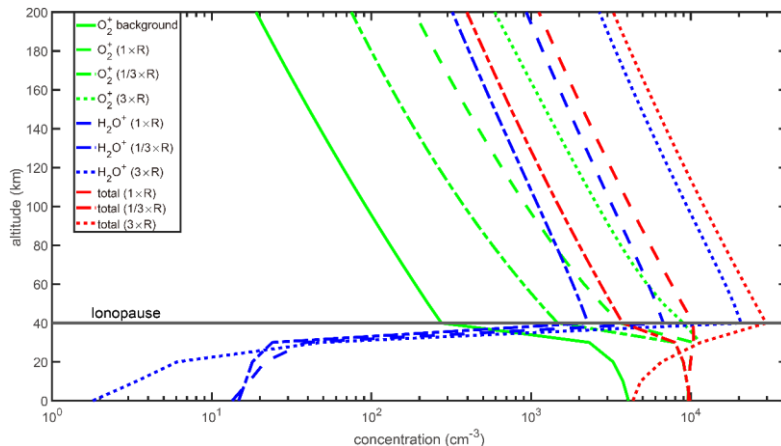


Figure 1.5: Comparison of the major ionized species between the background and plume-controlled atmosphere with different water column densities (the R in the legend represents a water column density of $1.5 \times 10^{16} \text{ cm}^{-2}$).

It should be noted that the plumes on Europa are intermittent, localized (Roth et al., 2014; Sparks et al., 2016) and models show that they have a specific umbrella-like canopy structure (Berg et al., 2016). Since we focus on the plume-controlled atmosphere, use a constant water column density and look for a stable solution, our model basically describes the atmosphere at the center of the water plume during its stable eruption time and our results rely on the assumption that all the chemical species are horizontally uniformly distributed in the middle part of the plume. The edge of the plume and the horizontal transport processes of the water molecules cannot be simulated by our current model. Therefore, a 2-D or 3-D chemical transport model, which will be developed in the future studies, is crucial to verify whether the assumption of horizontal uniformity is valid and to understand the influence of water plumes on the global atmosphere.

1.6 Acknowledgements

We thank D. Shemansky for useful discussions. This research was supported in part by an NSF grant to Caltech. M. S. G. thanks JPL for support through the JPL-Campus JROC program.

References

- Allen, M., Yung, Y. L., & Waters, J. W. (1981). Vertical transport and photochemistry in the terrestrial mesosphere and lower thermosphere (50–120 km). *Journal of Geophysical Research: Space Physics*, 86, 3617.
- Bagenal, F., Sidrow, E., Wilson, R. J., et al. (2015). Plasma conditions at Europa's orbit. *Icarus*, 261, 1.
- Benyoucef, D., & Yousfi, M. (2014). Ar⁺/Ar, O₂⁺/O₂ and N₂⁺/N₂ elastic momentum collision cross sections: Calculation and validation using the semi-classical model. *Plasma Science and Technology*, 16, 588.
- Berg, J. J., Goldstein, D. B., Varghese, P. L., et al. (2016). DSMC simulation of Europa water vapor plumes. *Icarus*, 277, 370.
- Brown, W. L., Augustyniak, W. M., Marcantonio, K. J., et al. (1984). Electronic sputtering of low temperature molecular solids. *Nuclear Instruments and Methods in Physics Research Section B: Beam Interactions with Materials and Atoms*, 1, 307.
- Cassidy, T. A., Johnson, R. E., & Tucker, O. J. (2009). Trace constituents of Europa's atmosphere. *Icarus*, 201, 182.
- Datz, S., Thomas, R., Rosén, S., et al. (2000). Dynamics of three-body breakup in dissociative recombination: H₂O⁺. *Physical Review Letters*, 85, 5555.
- Gladstone, G. R., Allen, M., & Yung, Y. L. (1996). Hydrocarbon photochemistry in the upper atmosphere of Jupiter. *Icarus*, 119, 1.
- Hall, D. T., Strobel, D. F., Feldman, P. D., et al. (1995). Detection of an oxygen atmosphere on Jupiter's moon Europa. *Nature*, 373, 677.
- Gudipati, M., Henderson, B., & Bateman, F. (2017). Effect of MeV Electron Radiation on Europa's Surface Ice Analogs. *AAS/Division for Planetary Sciences Meeting*, Abstracts# 49.
- Hansen, C. J., Shemansky, D. E., & Hendrix, A. R. (2005). Cassini UVIS observations of Europa's oxygen atmosphere and torus. *Icarus*, 176, 305.
- Ip, W. H. (1996). Europa's oxygen exosphere and its magnetospheric interaction. *Icarus*, 120, 317.
- Ip, W. H., Williams, D. J., McEntire, R. W., et al. (1998). Ion sputtering and surface erosion at Europa. *Geophysical Research Letters*, 25, 829.

- Jia, X., Kivelson, M. G., Khurana, K. K., et al. (2018). Evidence of a plume on Europa from Galileo magnetic and plasma wave signatures. *Nature Astronomy*, 2, 459.
- Johnson, R. E. (1990). *Energetic charged-particle interactions with atmospheres and surfaces* (Vol. 19). Springer Science & Business Media.
- Johnson, R. E., Leblanc, F., Yakshinskiy, B. V., et al. (2002). Energy distributions for desorption of sodium and potassium from ice: The Na/K ratio at Europa. *Icarus*, 156, 136.
- Johnson, R. E., Burger, M. H., Cassidy, T. A., et al. (2009). Composition and detection of Europa's sputter-induced atmosphere. *Europa, University of Arizona Press, Tucson*, 507.
- Kliore, A. J., Hinson, D. P., Flasar, F. M., et al. (1997). The ionosphere of Europa from Galileo radio occultations. *Science*, 277, 355.
- Le Teuff, Y. H., Millar, T. J., & Markwick, A. J. (2000). The UMIST database for astrochemistry 1999. *Astronomy and Astrophysics Supplement Series*, 146, 157.
- Leblanc, F., Johnson, R. E., & Brown, M. E. (2002). Europa's sodium atmosphere: An ocean source? *Icarus*, 159, 132.
- Liang, M. C., Lane, B. F., Pappalardo, R. T., et al. (2005). Atmosphere of Callisto. *Journal of Geophysical Research: Planets*, 110.
- Lucchetti, A., Plainaki, C., Cremonese, G., et al. (2016). Loss rates of Europa's tenuous atmosphere. *Planetary and Space Science*, 130, 14.
- McGrath, M. A., Hansen, C. J., & Hendrix, A. R. 2009, Europa, p.485. Edited by Robert T. Pappalardo, William B. McKinnon, Krishan K. Khurana, with the assistance of René Dotson with 85 collaborating authors. *University of Arizona Press, Tucson*.
- McGrath, M. A., & Sparks, W. B. (2017). Galileo ionosphere profile coincident with repeat plume detection location at Europa. *arXiv preprint arXiv:1711.03628*.
- Mul, P. M., McGowan, J. W., Defrance, P., et al. (1983). Merged electron-ion beam experiments. V. Dissociative recombination of OH⁺, H₂O⁺, H₃O⁺ and D₃O⁺. *Journal of Physics B: Atomic and Molecular Physics*, 16, 3099.
- Roth, L., Saur, J., Retherford, K. D., et al. (2014). Transient water vapor at Europa's south pole. *Science*, 343, 171.

- Roth, L., Saur, J., Retherford, K. D., et al. (2016). Europa's far ultraviolet oxygen aurora from a comprehensive set of HST observations. *Journal of Geophysical Research: Space Physics*, 121, 2143.
- Moses, J. I., Lellouch, E., Bézard, B., et al. (2000). Photochemistry of Saturn's atmosphere: II. Effects of an influx of external oxygen. *Icarus*, 145, 166.
- Mount, G. H., & Rottman, G. J. (1983). The solar absolute spectral irradiance 1150–3173 Å: May 17, 1982. *Journal of Geophysical Research: Oceans*, 88, 5403.
- Oza, A. V., Johnson, R. E., & Leblanc, F. (2018). Dusk/dawn atmospheric asymmetries on tidally-locked satellites: O₂ at Europa. *Icarus*, 305, 50.
- Saur, J., Strobel, D. F., & Neubauer, F. M. (1998). Interaction of the Jovian magnetosphere with Europa: Constraints on the neutral atmosphere. *Journal of Geophysical Research: Planets*, 103, 19947.
- Sheehan, C. H., & St.-Maurice, J. P. (2004). Dissociative recombination of N₂⁺, O₂⁺, and NO⁺: Rate coefficients for ground state and vibrationally excited ions. *Journal of Geophysical Research: Space Physics*, 109.
- Shemansky, D. E., Yung, Y. L., Liu, X., et al. (2014). A new understanding of the Europa atmosphere and limits on geophysical activity. *The Astrophysical Journal*, 797, 84.
- Shematovich, V. I., & Johnson, R. E. (2001). Near-surface oxygen atmosphere at Europa. *Advances in Space Research*, 27, 1881.
- Shematovich, V. I., Johnson, R. E., Cooper, J. F., et al. (2005). Surface-bounded atmosphere of Europa. *Icarus*, 173, 480.
- Sittler Jr, E. C., Cooper, J. F., Hartle, R. E., et al. (2013). Plasma ion composition measurements for Europa. *Planetary and Space Science*, 88, 26.
- Smyth, W. H., & Marconi, M. L. (2006). Europa's atmosphere, gas tori, and magnetospheric implications. *Icarus*, 181, 510.
- Sparks, W. B., Hand, K. P., McGrath, M. A., et al. (2016). Probing for evidence of plumes on Europa with HST/STIS. *The Astrophysical Journal*, 829, 121.
- Sparks, W. B., Schmidt, B. E., McGrath, M. A., et al. (2017). Active cryovolcanism on Europa? *The Astrophysical Journal Letters*, 839, L18.

- Teolis, B. D., Wyrick, D. Y., Bouquet, A., et al. (2017). Plume and surface feature structure and compositional effects on Europa's global exosphere: Preliminary Europa mission predictions. *Icarus*, 284, 18.
- Torr, M. R., & Torr, D. G. (1985). Ionization frequencies for solar cycle 21: Revised. *Journal of Geophysical Research: Space Physics*, 90, 6675.
- Vejby-Christensen, L., Andersen, L. H., Heber, O., et al. (1997). Complete branching ratios for the dissociative recombination of H_2O^+ , H_3O^+ , and CH_3^+ . *The Astrophysical Journal*, 483, 531.
- Vorburger, A., & Wurz, P. (2018). Europa's ice-related atmosphere: The sputter contribution. *Icarus*, 311, 135.
- World Meteorological Organization (1985), *Atmospheric Ozone*, vol. 1, Rep. 16, Geneva.
- Yung, Y. L., & McElroy, M. B. (1977). Stability of an oxygen atmosphere on Ganymede. *Icarus*, 30, 97.
- Yung, Y. L., and W. B. DeMore (1999), Photochemistry of Planetary Atmospheres, pp. 258, *Oxford Univ. Press, New York*.

Chapter II

OXIDANT GENERATION IN THE ICE UNDER ELECTRON IRRADIATION: SIMULATION AND APPLICATION TO EUROPA

This chapter is adapted from work previously published as

Li, J., Gudipati, M. S., Mishra, Y. N., Liang, M. C., & Yung, Y. L. (2022). Oxidant generation in the ice under electron irradiation: Simulation and application to Europa. *Icarus*, 373, 114760. <https://doi.org/10.1016/j.icarus.2021.114760>.

2.1 Abstract

Electron irradiation of ice is an important process in the Solar System, especially for icy satellites (e.g., Europa) whose tenuous atmospheres originate from the thermal and radiation-induced outgassing of their icy surfaces. Laboratory experiments have been performed on the electron irradiation of water ice to study the volatile gases (e.g., H₂ and O₂) that leave the surface and the chemical compounds (e.g., H₂O₂) that are produced inside the ice. Semi-empirical models have also been developed to estimate the production of the chemical species in the ice during irradiation as functions of electron energy and ice temperature. In this study, we build a chemistry-transport model to simulate chemical processes occurring in the ice during irradiation by 10 keV electrons and to describe how the chemical species of interest are formed, transported, and distributed in the ice. The simulated H₂O₂ mixing ratio agrees well with experiments performed by Hand and Carlson (2011). Our model can be applied to the surfaces of icy satellites (e.g., Europa) to estimate the oxidant generation in the ice and to evaluate the potential habitability of those satellites. This study calls for further experimental studies on ice under electron irradiation to constrain critical parameters such as rate coefficients and diffusion coefficients of volatile species produced by radiation in the ice.

2.2 Introduction

Based on the theory of ion sputtering, the prediction of the principal component of the atmosphere of Europa (Brown et al., 1982), one of Jupiter's icy satellites, was made a decade earlier than the first detection of Europa's atmosphere using the Hubble Space Telescope (Hall et al., 1995). The primary composition of Europa's surface is water ice. Laboratory results show that when energetic ions bombard water ice, H_2 and O_2 are ejected (Brown et al., 1982; Bar-Nun et al., 1985). Since H_2 escapes more easily than O_2 , O_2 is retained as the principal component of Europa's atmosphere (Johnson et al., 2009). Besides the ions, electron irradiation of ice also contributes to the release of gases from the ice into the exosphere, the chemical alteration of the ice composition, and modification of the surface (Baragiola et al., 2002; Orlando and Sieger, 2003; Zheng et al., 2006; Galli et al., 2018; Nordheim et al., 2018; Vorburger and Wurz, 2018; Meier and Loeffler, 2020; Davis et al., 2021). Since high energy electrons dominate the surface irradiation environment on Galilean icy satellites (Cooper et al., 2001), understanding the influence of electron irradiation on ice is crucial for understanding the chemical composition of both the atmosphere and surface of these bodies. While near-surface processes of ice-irradiation are the major source of the atmosphere, radiation-induced processes deeper inside the ice would control the surface ice composition and its exchange with the interior.

Because of electrons' negligible mass, their irradiation of the surface is dominated by electronic excitation rather than by nuclear collisions. When electrons penetrate water ice, secondary electrons and Bremsstrahlung X-rays with lower energy are generated, which can dissociate water molecules and produce radicals (such as H, O, OH) inside the ice. The ice exists in both amorphous and crystalline forms in the low-temperature environment (Berdis et al., 2020; Ligier et al., 2016). For example, 100 K is the average surface temperature of Europa. Both amorphous and crystalline ice can have microscopic porosity between the grains, which in amorphous ice occurs at the molecular level as well. The porosity of ice provides sufficient space for chemical reactions to happen inside the cavities as well as better mobility of volatile atoms and molecules. Hence, the newly formed radicals will induce

further chemical reactions inside the ice and form other molecules (e.g. O₂, H₂, H₂O₂). While the ionization processes that are known to be efficient in ice (Cook et al., 2015; Gudipati, 2004; Gudipati and Allamandola, 2003) also compete with dissociation pathways, ionized species such as H₂O⁺, H⁺, O⁺, etc., would eventually capture electrons to form neutral species that dominate equilibrium chemistry.

In a recent study, Galli et al. (2018) conducted experimental studies on the yields of various molecular species from ice when irradiated with energetic electrons. For electron energies between 0.2 keV and 10 keV irradiating water ice, they detect the release of roughly 2:1 H₂ and O₂ and a relatively low abundance of H₂O₂. In another experiment, a considerable amount of H₂O₂ is found in the ice at 100 K with a mixing ratio of ~0.03 % under the irradiation of 10 keV electrons (Hand and Carlson, 2011). Meanwhile, numerical models have also been developed to estimate the production of the species of interest in the ice during electron and/or ion irradiation. Suggesting oxygen atom as the dominant precursor for the formation of molecular oxygen in the ice, Johnson et al. (2005) built an analytical model to describe the formation and destruction processes of O and O₂ in ice during irradiation. A simple kinetic model, built by Petrik et al. (2006), uses OH, H₂O₂ and HO₂ as the precursors of the O₂ production and qualitatively reproduces their experimental results. A semi-empirical model has also been developed to calculate the theoretical expectations of the production of H₂, O₂ and H₂O₂ in ice as functions of the electron energy and the ice temperature (Teolis et al., 2017a).

In spite of the significant modeling efforts described above, the existing models include only limited chemical species and reactions and are not designed to describe the transport processes of the species of interest in the ice, which we show in this paper are important for reactive species redistribution in the ice. In order to close these gaps, we build a new comprehensive chemistry-transport model to simulate the different processes occurring in the ice during electron irradiation. This model resolves how different chemical species, especially oxidants, are formed, transported and distributed in the ice.

In the next section, we will present our model setup. Section 2.4 shows the simulation results of our model and makes comparisons with the existing experiments. In Section 2.5, we will discuss the limitations of our model and the prospect of future studies. In Section 2.6, we will present our conclusions and discuss the applications of the model.

2.3 Model Setup

Our one-dimensional chemistry-transport model is developed based on the Caltech/JPL chemistry-transport model KINETICS (Allen et al., 1981; Yung & DeMore, 1999). The governing equation of KINETICS is the continuity equation for each species i

$$\frac{\partial n_i}{\partial t} + \frac{\partial \phi_i}{\partial z} = P_i - L_i, \quad (2.1)$$

in which n_i is the number density, ϕ_i is the vertical flux, P_i is the chemical production rate, and L_i is the chemical loss rate at depth z and time t . The goal of the model is to find the steady-state solution so that $\partial n_i / \partial t = 0$. More details of the mechanism of KINETICS can be found in Gladstone et al. (1996). KINETICS is originally designed to simulate the chemical reactions and transport processes in the atmospheres of planets and moons, which have a scale of tens to hundreds of kilometers. We report here our first attempt to modify KINETICS to deal with chemistry-transport problems in the solid-phase on a much smaller scale of microns. In the model, we consider an ice shell of 5 μm , needed for 10 keV electron irradiation simulation, providing sufficient depth beyond the 10 keV electron penetration depth of 2.5 μm (Figure 2.1). The shell is divided into 123 layers, with 10^{-8} cm (1 \AA) spacing from the depth of 0 (surface) to the depth of 3×10^{-7} cm (3 nm), 10^{-7} cm (1 nm) spacing from the depth of 3×10^{-7} cm (3 nm) to the depth of 10^{-6} cm (10 nm), 10^{-6} cm (10 nm) spacing from the 10^{-6} cm (10 nm) to the depth of 4×10^{-5} cm (400 nm) and 10^{-5} cm (0.1 μm) spacing from the depth of 4×10^{-5} cm (0.4 μm) to 5×10^{-4} cm (5 μm). The chemical species considered in the model are H_2O , H, O, O_2 , OH, H_2 , O_3 , HO_2 , and H_2O_2 . The number density of H_2O is fixed at 3×10^{22} cm^{-3} that corresponds to a bulk density of 0.9 g/cm^3 . The temperature of the ice shell is fixed to 100 K and not affected by water dissociation or chemical reactions.

The energy of the incident electrons is set to be 10 keV (same as the energy used in Hand and Carlson (2011)). Based on CASINO (Drouin et al., 2007) and ESTAR (Berger et al., 2005) simulations as well as laboratory studies on ice using <2 keV electrons, earlier studies indicate that the 10 keV electrons are completely stopped at a penetration depth of ~ 2.5 μm , while 50% of these electrons are stopped at 1.5 μm depths (Barnett et al. 2012). During the penetration, the energy of the electron will be deposited in the ice and contribute to the water dissociation. On average, the energy used per dissociation of one water molecule through water ionization is about 12.7 eV (Snow and Thomas, 1990). Therefore, every electron can dissociate roughly 787 water molecules. As shown in Figure 2 of Barnett et al. (2012), the fraction of electrons that penetrate a given depth can be approximated to a sigmoid function (see Figure 2.1a). To construct a reasonable profile for the water dissociation rate of electrons, we discretize the whole stopping process into 10 steps. Step i is defined as the process during which the energy of the electron decreases from $(11-i)$ keV to $(10-i)$ keV, where $i = 1, 2, \dots, 10$. To map the step to the depth, we assume that the length of step i is inversely proportional to the stopping power of the electron at the energy of $(11-i)$ keV since the stopping power describes the retarding force acting on the electron. Within each step, we additionally assume that the 1 keV energy will be uniformly dissipated in the length. In Table 2.1, we show the stopping power of the electrons at different energies (obtained from ESTAR) and the corresponding percentages of the penetration depth that the 1 keV energy will be dissipated in. In other words, for each electron, its ten 1-keV-energy will be dissipated along with its penetration depth according to the percentages shown in Table 2.1. For example, the dissipation of the first 1-keV-energy, which corresponds to step 1, happens throughout the top 16.1 % of its penetration depth near the surface and the next 1-keV-energy will be dissipated in the range of 16.1 % to 31.0 % of the penetration depth. Combining this with the sigmoid function suggested by Barnett et al. (2012), the profile of the water dissociation rate is constructed. Meanwhile, the dissociated species can react to reform water due to the cage effect in solids (Denisov, 1984; Schwentner et al., 1991; Tarasoca et al., 1993; Johnson and Quickenden, 1997). Here we reduce the water dissociation rate by 50% in consideration of the cage effect. In the model, we use a continuous supply of incident electrons with a flux of 1.2×10^{12} electrons/cm²/s (within the range of electron flux used in

Hand and Carlson (2011)). The corresponding water dissociation rate profile in the ice shell is shown in Figure 2.1b. Each water molecule can be dissociated into either an H atom and an OH or an H₂ and an O atom. Here, we assume that 78% of the water molecules are dissociated into H and OH and the remaining 22% are dissociated into H₂ and O (Teolis et al., 2009).

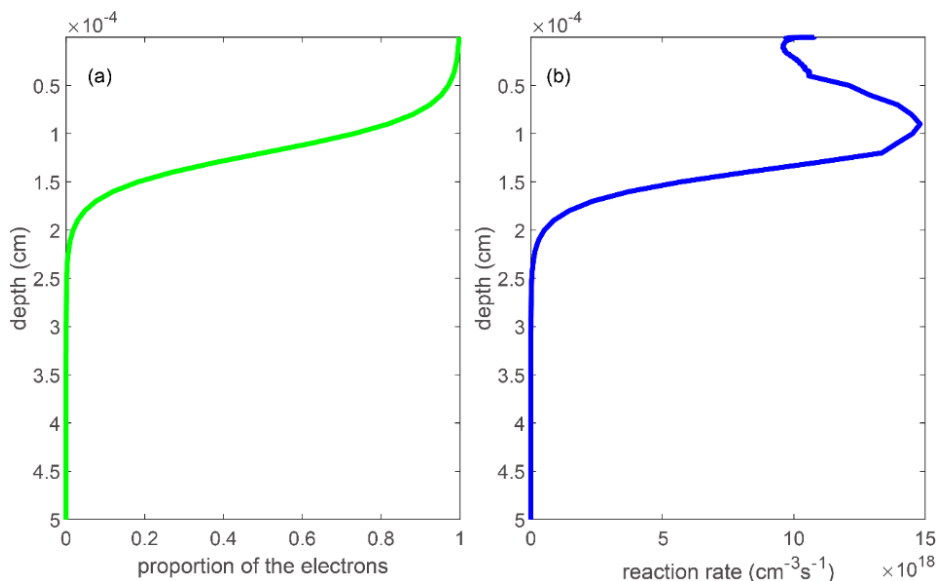


Figure 2.1: Calculations of the water dissociation. (a) The fraction of 10 keV electrons that penetrate a given depth. (b) The profile of the water dissociation rate in the ice shell.

Energy (keV)	10	9	8	7	6	5	4	3	2	1
Stopping power (MeV cm ² /g)	22.6	24.5	26.8	29.7	33.4	38.4	45.4	56.2	75.2	112
Percentage of the penetration depth (%)	16.1	14.9	13.6	12.3	10.9	9.5	8.0	6.5	4.9	3.3

Table 2.1: The stopping power of the electron (Berger et al., 2005) and its corresponding percentage of the penetration depth at different energy.

(a)

Reactions	Rate Coefficients ^a	References ^b
1. OH + OH + M ^c → H ₂ O ₂ + M	4.21×10^{-29}	1
2. OH + OH → O + H ₂ O	4.63×10^{-11}	2

3. $\text{OH} + \text{H}_2\text{O}_2 \rightarrow \text{HO}_2 + \text{H}_2\text{O}$	5.85×10^{-13}	3
4. $\text{OH} + \text{H} + \text{M} \rightarrow \text{H}_2\text{O} + \text{M}$	3.89×10^{-29}	4
5. $\text{O} + \text{H} + \text{M} \rightarrow \text{OH} + \text{M}$	1.30×10^{-31}	5
6. $\text{O} + \text{O} + \text{M} \rightarrow \text{O}_2 + \text{M}$	1.21×10^{-31}	6
7. $\text{O} + \text{HO}_2 \rightarrow \text{OH} + \text{O}_2$	2.17×10^{-10}	7
8. $\text{O} + \text{OH} \rightarrow \text{O}_2 + \text{H}$	7.30×10^{-11}	7
9. $\text{OH} + \text{HO}_2 \rightarrow \text{O}_2 + \text{H}_2\text{O}$	5.86×10^{-10}	7
10. $\text{O} + \text{H}_2 \rightarrow \text{OH} + \text{H}$	4.03×10^{-28}	7
11. $\text{OH} + \text{H}_2 \rightarrow \text{H} + \text{H}_2\text{O}$	5.84×10^{-21}	3
12. $\text{H} + \text{HO}_2 \rightarrow \text{OH} + \text{OH}$	7.30×10^{-11}	7
13. $\text{H} + \text{HO}_2 \rightarrow \text{O}_2 + \text{H}_2$	6.40×10^{-12}	7
14. $\text{H} + \text{H} + \text{M} \rightarrow \text{H}_2 + \text{M}$	1.80×10^{-32}	8
15. $\text{H} + \text{H}_2\text{O}_2 \rightarrow \text{OH} + \text{H}_2\text{O}$	1.49×10^{-13}	9
16. $\text{O}_2 + \text{H} \rightarrow \text{HO}_2$	1.16×10^{-33}	9
17. $\text{HO}_2 + \text{HO}_2 \rightarrow \text{H}_2\text{O}_2 + \text{O}_2$	1.16×10^{-15}	9
18. $\text{O} + \text{O}_2 + \text{M} \rightarrow \text{O}_3 + \text{M}$	9.33×10^{-35}	10
19. $\text{H} + \text{O}_3 \rightarrow \text{O}_2 + \text{OH}$	2.79×10^{-11}	11
20. $\text{O} + \text{O}_3 \rightarrow \text{O}_2 + \text{O}_2$	9.05×10^{-21}	7

^aUnits are $\text{cm}^3 \text{s}^{-1}$ for two-body reactions and $\text{cm}^6 \text{s}^{-1}$ for three-body reactions.

^bReferences: 1, Sangwan et al. (2012); 2, Altinay and Macdonald (2014); 3, Atkinson et al. (2004); 4, Javoy et al. (2003); 5, Tsang and Hampson (1986); 6, Campbell and Gray (1973); 7, see references of Yung and DeMore (1999); 8, Baulch et al. (1992); 9, see references of Roth and LaVerne (2011); 10, De Cobos and Troe (1984); 11, Chen et al. (1981);

^cHere M is H_2O .

(b)

Chemical composition	H	O	O_2	OH	H_2	O_3
Upper boundary condition ($\times 10^{13} \text{cm}^{-3}$)	0.5	0.2	2.5×10^4	0.2	2	2

(c)

Chemical composition	H	O	O_2	OH	HO_2	H_2O_2	H_2	O_3	H_2O
Column density ($\times 10^{15} \text{cm}^{-2}$)	1.08×10^{-6}	1.71×10^{-5}	1.26×10^{-1}	1.25×10^{-6}	9.61×10^{-4}	2.22	3.19×10^{-4}	5.52×10^{-4}	15000

Table 2.2: Reaction coefficients, boundary conditions, and column densities. (a) A list of reactions in our modeled ice shell, including their rate coefficients and references. (b) The fixed-density upper boundary conditions of H, O, O_2 , OH, H_2 and O_3 . Note that the H_2O density is fixed to be $3 \times 10^{22} \text{cm}^{-3}$. (c) The column densities of all the chemical species in the model.

Further reactions are initiated by these primary radicals and other secondary radicals produced in the ice. A total of 20 chemical reactions are considered in our model and their corresponding rate coefficients at 100 K are listed in Table 2.2a. Reaction rate coefficients that are not included in this table are either unknown or several orders of magnitude lower than those of competing reactions that are included in our model. Different from the environment where those rate coefficients are measured (usually in the gas-phase), the water ice provides a solid-state water environment that limits the mobility of atomic and molecular species in the ice (O, H, etc.) so that the actual rate coefficients are expected to be significantly lower than the coefficients measured in the laboratory under gas-phase conditions. So far, the reaction rates of these reactions are not experimentally measured in the ice environment. Without further knowledge about the reduction of the chemical reaction rates in the ice, here we assume that the rate coefficients in the ice are 1 % of the coefficients listed in Table 2.2a that are determined in the gas-phase. While this fraction may change, we assume that the relative rate coefficients of different reactions may not significantly vary from the gas-phase. Sensitivity tests are performed in the next section to show the influence of the rate coefficients on the simulation results. Except for HO₂, H₂O₂ and the host H₂O ice, the rest of the molecules/atoms are allowed to diffuse inside the ice. An experiment performed by Lee and Meuwly (2014) shows that the diffusion coefficient of O atoms in amorphous ice at 100 K is $1.74 \times 10^{-4} \text{ cm}^2 \text{ s}^{-1}$. The diffusion coefficients of other species are scaled with the diffusion coefficient of O and set to be proportional to the square root of their masses. Such a mass-based diffusion approximation may not hold good for different molecular species. For example, radicals such as H, O, OH are expected to interact with H₂O molecules strongly than the molecules such as H₂ and O₂, as a result diffusion coefficient of H₂ and O₂ could be higher than those coefficients derived from mass-based approximation only. In the present work, we did not look into varying these parameters further. For the upper boundary (surface) condition, the density of H, O, O₂, OH, H₂, and O₃ (the diffusive species) are fixed at values that are given in Table 2.2b. If there is a certain pressure of gas in the exosphere, there will be saturated gas density in the ice so that the flux of the gas at the surface is 0. If the actual gas density in the ice is higher than that, the gas will diffuse out from the surface and there will be a positive flux. Therefore, the fixed density boundary

condition serves as the density of these species in ice at the surface in contact with the exosphere. The fluxes of HO_2 and H_2O_2 are fixed to 0 at the upper boundary. The lower boundary condition is set to 0 flux for all species. Sensitivity tests for the upper boundary condition are also performed.

2.4 Simulation Results

The density profiles of the constituents constructed by our model are shown in Figure 2.2. The column densities of each species, accompanied by water molecules, are presented in Table 2.2c. It shows that the most concentrated species in the ice is H_2O_2 . The average mixing ratio of H_2O_2 in the ice shell is $\sim 0.015\%$. The simulated mixing ratio is close to the H_2O_2 mixing ratio ($\sim 0.029\%$) detected in electron irradiation experiments of Hand and Carlson (2011). O_2 and HO_2 are the next most concentrated species other than H_2O_2 , whose densities are about 1 and 2 orders of magnitude lower than that of H_2O_2 . Figure 2.2 shows that O_3 also exists in the ice but the density of O_3 is about 3 orders of magnitude lower than that of O_2 . To better understand the formation and destruction processes of the oxidants in the ice, the reaction rate profiles of the major formation and destruction reactions of H_2O_2 , O_2 and O_3 are shown in Figure 2.3, Figure 2.4 and Figure 2.5, respectively. In these figures, the solid lines represent the formation reactions, and the dashed lines represent the destruction reactions. Figure 2.3 shows that H_2O_2 is mainly formed from the three-body reaction of two OH radicals and destroyed by H and OH radicals. The rate of the reaction between two HO_2 radicals (Reaction 17), which occurs commonly in the gas-phase chemistry (Yung & DeMore, 1999), is comparable to the reaction rate of Reaction 1 only near the surface. It is worth mentioning that Reaction 3, OH reacting with H_2O_2 , is the major source of HO_2 , which is an important constituent for further reactions. In our model, H_2O_2 does not diffuse. As a result, the H_2O_2 profile (shown as the red line in Figure 2.2) reflects the balance between its production and destruction processes with depth. From Figure 2.1, the water dissociation rate decreases below 1 micron and becomes zero below 2.5 microns. The production rate of H_2O_2 reflects decreased production between 1 and 2.5 microns. Below 2.5 microns, H_2O_2 production and destruction are governed by the diffusion of OH (Reactions 1) and the

diffusion of H (Reaction 15). Figure 2.3 shows that the chemical production and loss rate of H_2O_2 is on the order of $10^{17} \text{ cm}^{-3}\text{s}^{-1}$. Since the H_2O_2 concentration is on the order of 10^{18} cm^{-3} , Figure 2.3 suggests that the time scale for H_2O_2 to reach equilibrium in our model is on the order of 10 seconds. To our surprise, we find that the mixing ratio of O_2 in ice is somewhat insensitive to depth due to the fact that the upper boundary condition O_2 density is very high compared to the rest of the species (see Table 2.2b). Figure 2.4 shows that besides the combination of two O atoms (Reaction 6), Reactions 7 (solid green line) and 10 (solid black line) are the other two major sources of O_2 in the ice, which indicate the crucial role that HO_2 plays in the O_2 formation. The primary O_2 destruction reactions, shown as the dashed blue line and dashed red line in Figure 2.4, are Reaction 16 and 18. Reaction 18 is also the main source of O_3 in the ice (see the solid blue line in Figure 2.5).

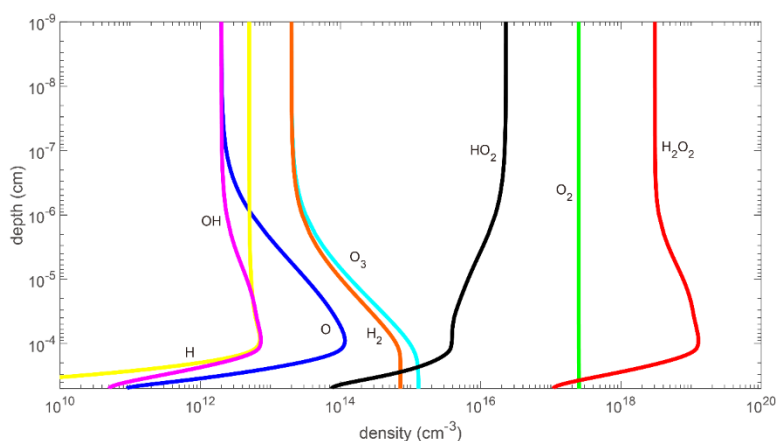


Figure 2.2: Density profiles of radiolytically produced species in water ice at 100 K upon 10 keV electron irradiation at 1.2×10^{12} electrons/ cm^2/s flux.

In real experiments and icy surface environment, the proper upper boundary conditions of the gas-phase molecules (e.g. H_2 , O_2) are constrained by two factors. The first one is the partial pressure of those molecules in the high vacuum environment above the surface. The second one is the relation between the dissolved densities of the gases in the ice without any electron irradiation and the partial pressures of the corresponding gases above the surface. The partial pressures are different across experiments and sometimes not provided by the authors. Meanwhile, we are not aware of any published work studying the dissolved densities of the gases in ice at 100 K. Therefore, the upper boundary conditions of these gases are hard

to constrain, particularly whether the ice is amorphous or crystalline, with low or high porosity. Both amorphous and crystalline ice can have microscopic porosity, which in amorphous ice also occurs at the molecular level. All of those ice properties may affect the upper boundary conditions. In the absence of these experimental data, we can test the model to different assumed boundary conditions. Hence, here we carry out sensitivity tests on the upper boundary conditions to evaluate their influences on our model results. We scale the fixed-density upper boundary conditions (the values shown in Table 2.2b) either down or up by a factor of 5, and the results are shown in Figure 2.6, along with the original run. We can see that the change of upper boundary conditions has considerable impact on the density profiles, especially in the first micron near the surface. However, the H_2O_2 profiles change very little in the bottom 4 microns, which suggests that the average mixing ratio of H_2O_2 in the ice shell is not sensitive to the boundary conditions. The mixing ratio of H_2O_2 remains around 0.013 % to 0.015 % in the sensitivity tests. As for other species, the density gradients at the surface, which correspond to the upward fluxes of the gases, are also changed with the upper boundary conditions. This phenomenon implies that the upward fluxes of the gases are sensitive to the boundary conditions.

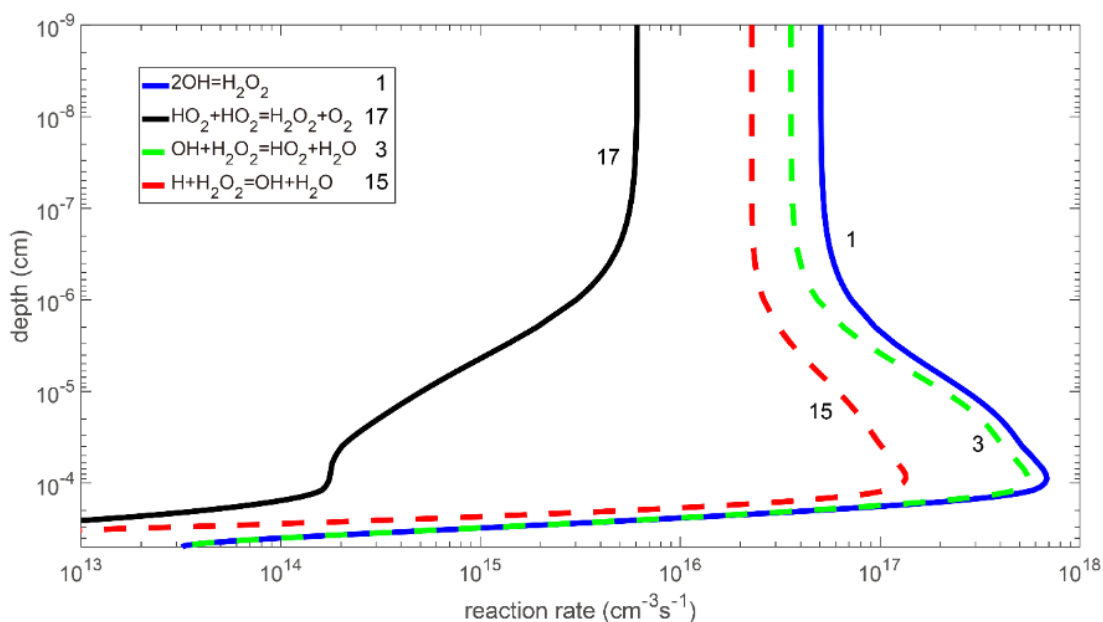


Figure 2.3: The profiles of the reaction rates of the production (solid curve) and destruction (dashed) reactions related to H_2O_2 .

As we state in the previous section, the real rate coefficients of the chemical reactions in ice are also not well constrained. Sensitivity tests are also done for all the rate coefficients by scaling the values in the ice either up or down by a factor of 10. The results are shown in Figure 2.7 together with the original run. With the rate coefficients going upward or downward by a factor of 10, the mixing ratio of H_2O_2 goes downward to $\sim 0.005\%$ or goes upward to $\sim 0.047\%$, which are still comparable to 0.029% from Hand and Carlson (2011). The densities of HO_2 , O , OH and O_3 change within one order of magnitude while the density of O_2 is controlled by the boundary condition and changes by less than 0.5% .

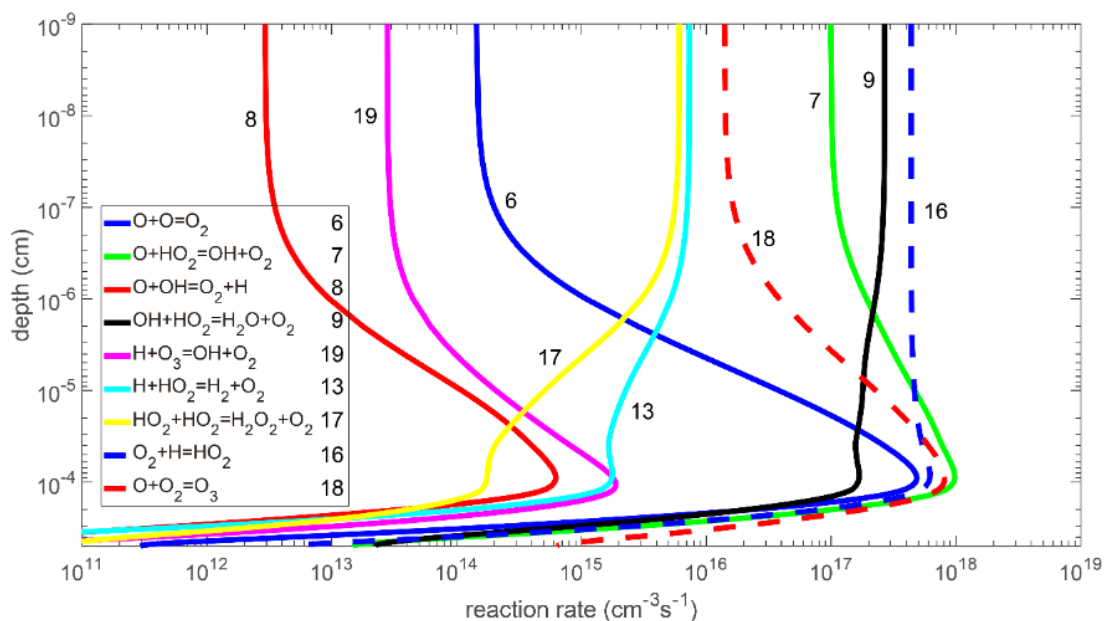


Figure 2.4: The profiles of the reaction rates of the production (solid curves) and destruction (dashed) reactions related to O_2 .

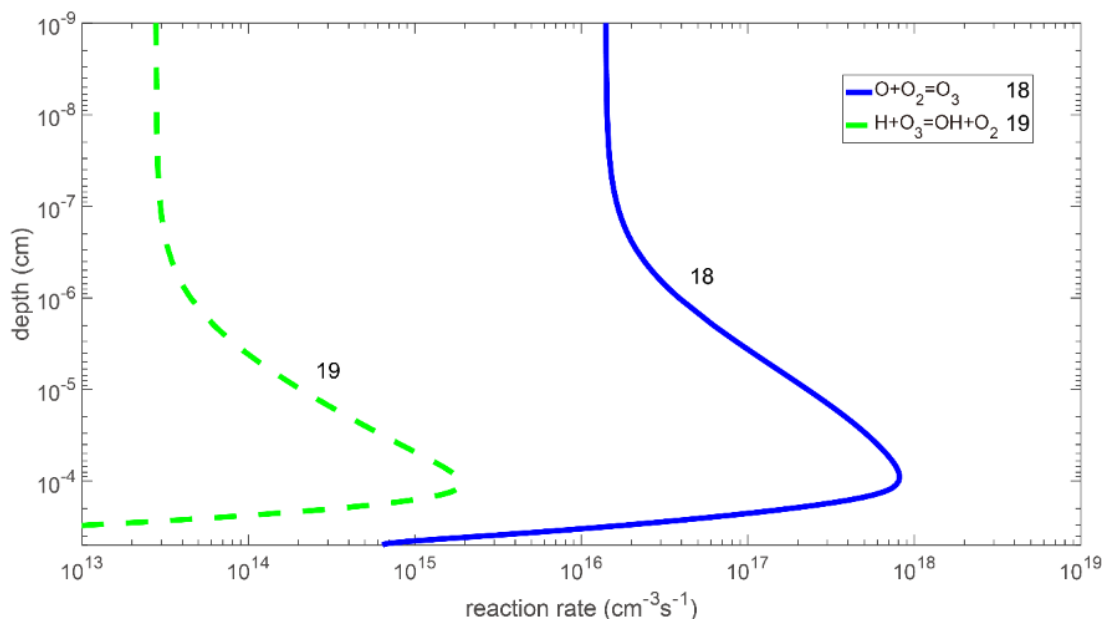


Figure 2.5: The profiles of the reaction rates of the production (solid curves) and destruction (dashed) reactions related to O_3 .

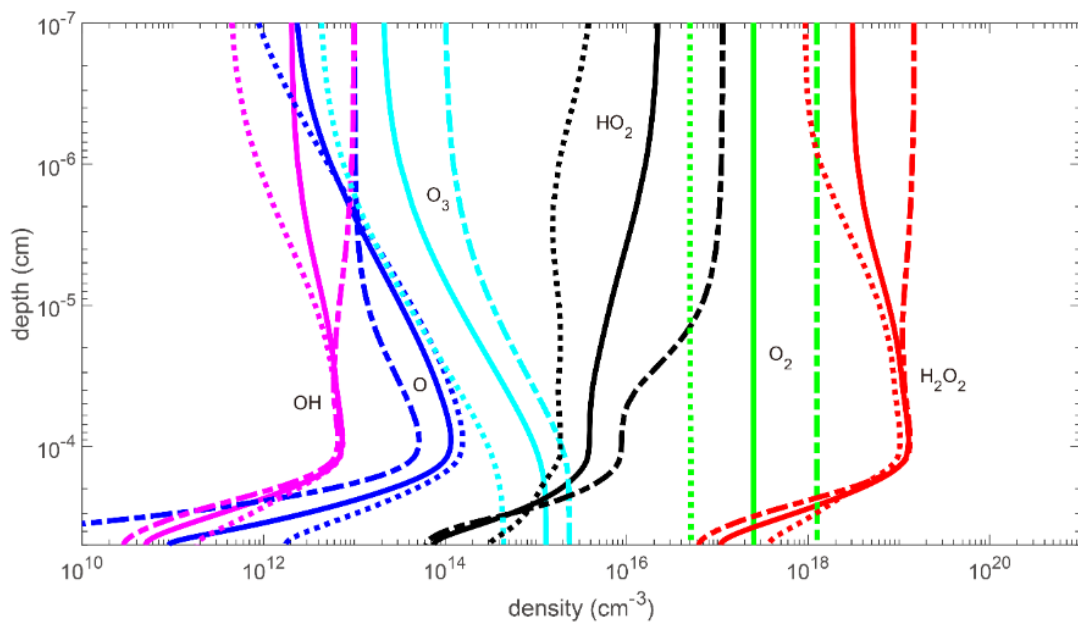


Figure 2.6: Sensitivity tests of the upper boundary conditions. The solid lines represent the original run. The dashed lines represent the run with fixed-density upper boundary conditions adjusted upward by a factor of 5 while the dotted lines represent the upper boundary conditions adjusted downward by a factor of 5.

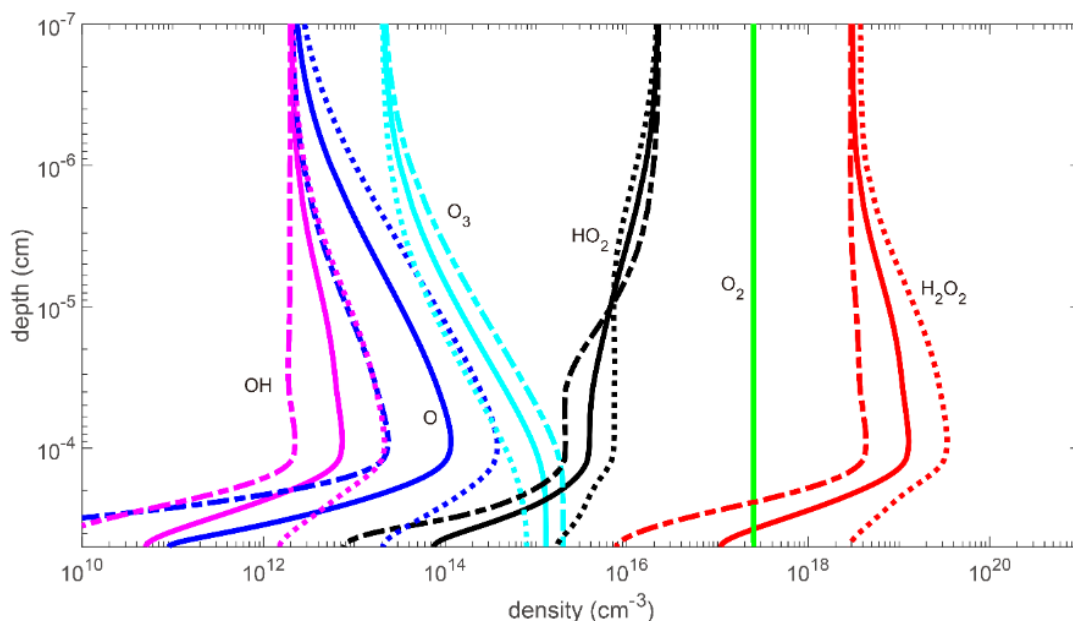


Figure 2.7: Sensitivity tests of the rate coefficients. The solid lines represent the original run. The dashed lines represent the run with rate coefficients adjusted upward by a factor of 10 while the dotted lines represent the rate coefficients adjusted downward by a factor of 10.

2.5 Discussion and Future Studies

The major drawback of our present model is that the O_2 profile does not reproduce the O_2 observed in experimental and observational studies. Teolis et al. (2010, 2017a) showed that the production of O_2 is most effective within the 30 \AA near the surface, which is not reproduced by our model. Additionally, experimental studies (Teolis et al., 2005, 2009; Meier and Loeffler, 2020) show that the concentration of O_2 builds up and maximizes within $\sim 150 \text{ \AA}$ near the surface and then steadily decreases with depth. Based on the ground-based observational data on $(O_2)_2$ absorptions at 577 nm and 627.5 nm by Spencer and Calvin (2002), Hand et al. (2006) estimated that O_2 mixing ratio should be between 1.2% and 4.6% of H_2O , at least an order of magnitude higher than the H_2O_2 mixing ratio observed. However, the O_2 concentration in our model is close to the concentration of H_2O_2 only at the bottom of the 5 \mu m ice shell. Near the surface, the concentration of O_2 is comparable to the concentration of H_2O_2 but about an order of magnitude lower. There are several possible explanations for this discrepancy. First, the experiments that support the most effective production of O_2 within the top 30 \AA are mostly ion irradiation experiments, i.e., contribution

of ion-irradiation for O₂ production is dominant. Since electrons penetrate much deeper than the ions, it is reasonable to find the highest O₂ production rate around 1 micron given in Figure 2.4. Meanwhile, recent electron-irradiation experiments (Davis et al., 2021) suggest electron-irradiated production of O₂ is significant, ruling out the lack of ion-irradiation in our model as the source of the discrepancy. Second, in our model, the density of water molecules is fixed to 0.9 g/cm³ under electron irradiation. However, in a more realistic scenario, the ice formed at such a low temperature may be highly porous with high containing ability and high diffusion coefficients of the gases. For example, the observations of Spencer and Calvin (2002) of Europa, Ganymede, and Callisto revealed high concentrations of O₂ in the surface ice, which could only be partly reproduced by earlier experimental work (Baragiola and Bahr, 1998). Meanwhile, the density of the ice and its microscopic structure will change due to the continuous electron bombardment (Johnson and Jesser 1997; Zheng et al., 2009; Loeffler et al., 2020; Behr et al., 2020). Those effects may influence the mixing ratios of the O₂ in the near-surface ice and will have to be considered in the future. Third, the sources and sinks of O₂ may not have been exhausted in our model and the source reaction rates may have been underestimated and sink reaction rates may have been overestimated. For example, Loeffler et al. (2006) suggest that the reaction $\text{HO}_2 + \text{H}_2\text{O}_2 \rightarrow \text{H}_2\text{O} + \text{OH} + \text{O}_2$ is an important source of O₂ in the ice. The reaction $\text{O} + \text{H}_2\text{O}_2 \rightarrow \text{H}_2\text{O} + \text{O}_2$ is also a possible source of O₂. However, we do not include those reactions in our model because there is no study giving an estimation of the rate coefficients at temperatures around 100 K. Denisova (2007) gives a rate coefficient of $5.26 \times 10^{-17} \text{ cm}^3 \text{ s}^{-1}$ for the reaction $\text{HO}_2 + \text{H}_2\text{O}_2 \rightarrow \text{H}_2\text{O} + \text{OH} + \text{O}_2$ at ~350 K. In a test run, we include this reaction to test the potential influence of this reaction on our model results. The test shows that the O₂ concentration in the ice changes by less than 0.1%. Further investigations on the O₂ generation mechanisms are needed to improve our model. Fourth, most of the rate coefficients in Table 2.2a are not directly measured at 100 K in the gas-phase but extrapolated to 100 K based on the rate coefficients determined at higher temperatures. Hence, the actual rate coefficients may be different from the coefficients used in our model. If the actual rate coefficients of the major formation reactions of O₂ (Reactions 6, 7 and 9) are higher than expected or the actual rate coefficients of the major destruction reactions of O₂ (Reactions 16 and 18) are lower than expected, a

higher O₂ concentration can be maintained in the ice. It is also possible that the uncertainty of the boundary condition of key species that are involved in the production or destruction of O₂ may influence the equilibrium O₂ concentration. For example, if H is decreased at the upper boundary of the model, the major O₂ destruction process will be suppressed, which will lead to higher O₂ concentration in the ice. Finally, diffusion rate of these species may not scale to the square root of their mass, but a combination of mass (hence size) and electronic interactions with H₂O host molecules. Species with smaller dipole or closed electronic structure may diffuse faster than those with larger dipole or radicals. Other non-equilibrium processes include potential clathration of O₂ may bring the mixing ratio in crystalline water ice to up to 4.6% as proposed by Hand et al. (2006). It is not clear which of these above discussed processes are critical and occurring on Europa's surface, but it is clear from our present modeling efforts that there is an O₂ anomaly between estimates based on observations and our modeling work. So far, we are not aware of experimental work that provides laboratory constraints on the O₂ mixing ratio in water ice caused by electron irradiation.

As we mentioned in the previous sections, the lack of knowledge about gas-ice interaction at the surface and in the bulk ice is limiting the application of our model. In order to get realistic representation, one needs both the dissolved densities of the gases in the ice and the partial pressures of the corresponding gases above the surface. Only then we can better predict reliable values of the upward fluxes of the gases at the surface because they are highly correlated to the upper boundary conditions. That is why we did not compare our model with the existing experiments that provide the values of H₂ and O₂ desorption only (e.g. Galli et al., 2018). Meanwhile, the limited knowledge of chemical reactions in ice also puts uncertainty in our model. In this model, we assume that the relative rate coefficients of different reactions in ice do not vary from the gas-phase. However, we are not aware of any quantitative studies that support or refute this assumption. If one or several major reactions are favored in the solid phase, the real density profiles will be different from the simulated results. Further, the electron-impact induced dissociative partitioning of H₂O is fixed in our present study to be 78% for H+OH, and 22% for H₂ + O. Any changes in this partitioning

could also influence equilibrium production of H_2O_2 and O_2 , which needs to be further investigated. In a test run, we set the partitioning of H_2O dissociation to be 50%/50% and as expected, the oxygen species O , O_2 , and O_3 slightly increased, while no significant change in the H_2O_2 mixing ratio was observed.

We wish our study will inspire the community to perform further experiments on H_2O ice radiation chemistry and quantify both the equilibrium ice composition and radiation-induced outgassing under similar conditions in order to constrain the crucial parameters in our model. For example, future experiments on H , O and OH surface fluxes combining with the existing experiments on H_2 and O_2 fluxes (Heide, 1984; Cassidy et al., 2010; Galli et al., 2018; Meier and Loeffler, 2020; Davis et al., 2021) may help us constrain the upper boundary conditions. With more realistic parameters, the upward fluxes of the gases derived from the model can also be used to construct the atmospheres above the icy surfaces (Shematovich et al., 2005; Smyth and Marconi, 2006; Teolis et al., 2017a, 2017b; Li et al., 2020), while downward fluxes of oxidants enable us to determine the oxidant transportation in ice and the surface-interior mixing.

Currently, we only consider chemical compositions that contain H and O atoms. In the real world, the surfaces of icy satellites are also experiencing an intense flux of energetic ions from the magnetosphere. Sulfur ions, which are an important component of the magnetosphere ions, will introduce more impurities in the ice (Moore, 1984; Carlson et al., 2002; Moore et al., 2007; Strazzulla et al., 2007; Loeffler et al., 2011). The experiments performed by Ding et al. (2013) find that hydrated sulfuric acid is produced in ice under sulfur ion implantation. More chemical compounds and reactions in the chemistry-transport model are needed in the future to better simulate the minor species in ice under irradiation. Additionally, high-energy (up to MeV) ions may have high electronic stopping powers (Gomis et al., 2004; Loeffler et al., 2006; Teolis et al., 2017a), which suggests that they are able to dissociate water molecules as the electrons do. The contribution of ion irradiation to the generation of oxidants in ice will be considered in the future studies.

2.6 Conclusions and Applications to Europa

In this study, we have built and demonstrated the applicability of a quantitative chemistry-transport model to simulate the formation, transport and distribution of chemical species produced in the ice during electron irradiation. Despite the discrepancies mentioned in the previous sections, our result for H_2O_2 equilibrium concentration in water-ice (0.015%) agrees well with the existing experiment (Hand and Carlson, 2011) at 0.029%, which implies the validity of our model. However, there still needs to be further laboratory work and tweaking of our model based on the refined laboratory data in order to closely reproduce concentrations of H_2O_2 observed on Europa's leading hemisphere to be 0.13% with respect to water (Hand and Brown, 2013). We could not reproduce estimated O_2 mixing ratios based on observational data in our model. More experimental work is necessary to constrain the input parameters of our model in order to improve our predictions. Analysis of the modeling results shows that HO_2 is an important intermediary in the formation of O_2 in ice. Laboratory data on the production and reaction rates of key intermediate species and their diffusion coefficients in the ice matrix are needed to better constrain our models and provide realistic predictions. We demonstrated how changing reaction rates and boundary conditions could alter the equilibrium concentrations of the species in ice.

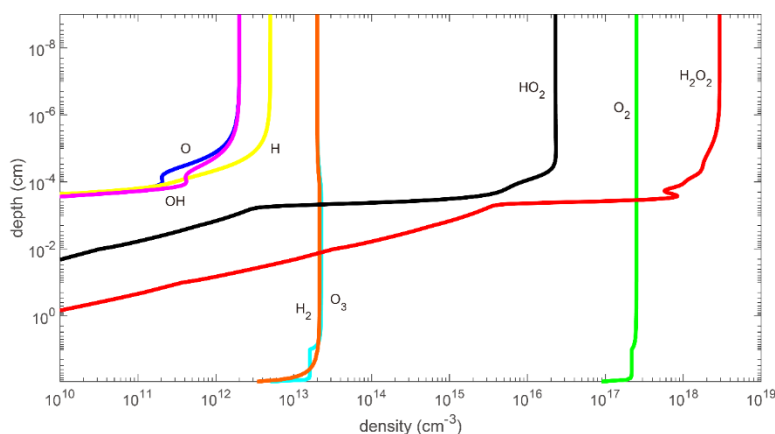


Figure 2.8: Density profiles of all the chemical species in the simplified 1D-model representing 10 keV electron bombardment of Europa's water-ice surface. The depth is expanded from 5 μm to 1 m compared to Figure 2.2.

Since icy satellites (e.g., Europa) in the Solar System are embedded in the magnetosphere of the Gas Giants, energetic electrons (with energy up to hundreds of MeV) constantly bombard the surfaces of the icy satellites (Cooper et al., 2001). In future studies, with the input of the local electron energy spectrum of an icy satellite and its corresponding water dissociation rate profile in the ice, we can expand the vertical range of our model and apply our model to the icy satellites to estimate the oxidants (H_2O_2 , O_2 , O_3 , etc.) generated on the surface of those satellites. Here we present a simplified example for Europa. The radiation flux at Europa is $\sim 8 \times 10^{13}$ eV/cm²/s (Cooper et al., 2001; Madey et al., 2002). Assuming that the radiation flux is solely contributed by electrons with the energy of 10 keV, then the corresponding electron flux is $\sim 8 \times 10^9$ electrons/cm²/s. We expand the vertical range of our model to 1 m and the lower boundary condition is set to 0 density for all species. With the updated water dissociation rate profile, we run the standard model and the density profiles are shown in Figure 2.8. While higher energy electrons above 10 keV (up to several tens of MeV) continue to produce radicals at the surface of Europa through several tens of cm deep, our model still applies at depths where radiation-induced production of radicals ceases to occur. Within the optical depth of H_2O_2 in the infrared channel (~ 50 μm according to Hand and Brown (2013)), the mixing ratio of H_2O_2 in the ice is $\sim 2.4 \times 10^{-6}$, which agrees with the extremely low concentration of H_2O_2 in the trailing hemisphere of Europa obtained by the Keck II observations (Hand and Brown, 2013). The column densities of all the chemical species in the 1 m range are shown in Table 2.3 (some numbers are much higher than the numbers in Table 2.2c due to the integration over a large depth of 1 m). Even though the current model setup is oversimplified, our model gives an order of magnitude estimation of the H_2O_2 that can be used as a reference for future studies. A more sophisticated prediction of the abundances of oxidants (including O, O_2 , O_3 , etc.) at the icy satellites' surfaces will be performed in the future. In a recent study, Howell and Pappalardo (2018) proposed that ice convection processes exist on Europa, which could transport the near-surface materials to the subsurface ocean in time scales of about 100 kyr to 1 Myr. Since the availability of oxidants is a significantly important factor for biologically useful chemical energy in the ocean of Europa (Johnson et al., 2003; Hand et al., 2007), our model can be used to estimate the transport of oxidants, in particular H_2O_2 , to the subsurface ocean of Europa (and other

icy satellites with similar convection mechanism) and give insight into Europa's habitability (Chyba, 2000; Parkinson et al., 2006).

Chemical composition	H	O	O ₂	OH	HO ₂	H ₂ O ₂	H ₂	O ₃
Column density ($\times 10^{15} \text{cm}^{-2}$)	1.61 $\times 10^{-7}$	6.36 $\times 10^{-8}$	2.03 $\times 10^4$	1.02 $\times 10^{-7}$	2.78 $\times 10^{-3}$	3.57 $\times 10^{-1}$	1.38	1.53

Table 2.3: The column densities of all the chemical species in the simplified 1D-model for Europa's surface ice.

2.7 Acknowledgements

This research was supported in part by an NSF grant to Caltech. M. S. G. thanks JPL for support through the JPL-Caltech JROC program and partial support from the NASA SSW program. Y. L. Y. acknowledges support by the Virtual Planetary Laboratory of the University of Washington. Y. N. M. gratefully acknowledges the Swedish Research Council for the financial support of the Project IPD 2018-06783.

References

- Allen, M., Yung, Y. L., & Waters, J. W. (1981). Vertical transport and photochemistry in the terrestrial mesosphere and lower thermosphere (50–120 km). *Journal of Geophysical Research: Space Physics*, 86, 3617.
- Atkinson, R., Baulch, D. L., Cox, R. A., et al. (2004). Evaluated kinetic and photochemical data for atmospheric chemistry: Volume I-gas phase reactions of Ox, HOx, NOx and SOx species. *Atmospheric Chemistry and Physics*, 4, 1461.
- Altinay, G., & Macdonald, R. G. (2014). Determination of the rate constant for the OH (X²Π) + OH (X²Π) → H₂O + O (3P) reaction over the temperature range 295 to 701 K. *The Journal of Physical Chemistry A*, 118, 38.
- Baragiola, R. A., & Bahr, D. A. (1998). Laboratory studies of the optical properties and stability of oxygen on Ganymede. *Journal of Geophysical Research: Planets*, 103, 25865.

- Baragiola, R. A., Atteberry, C. L., Dukes, C. A., et al. (2002). Atomic collisions in solids: astronomical applications. *Nuclear Instruments and Methods in Physics Research Section B: Beam Interactions with Materials and Atoms*, 193, 720.
- Barnett, I. L., Lignell, A., & Gudipati, M. S. (2012). Survival depth of organics in ices under low-energy electron radiation (≤ 2 keV). *The Astrophysical Journal*, 747, 13.
- Bar-Nun, A., Herman, G., Rappaport, M. L., et al. (1985). Ejection of H₂O, O₂, H₂ and H from water ice by 0.5–6 keV H⁺ and Ne⁺ ion bombardment. *Surface Science*, 150, 143.
- Baulch, D. L., Cobos, C., Cox, R. A., et al. (1992). Evaluated kinetic data for combustion modelling. *Journal of Physical and Chemical Reference Data*, 21, 411.
- Behr, P. R., Tribbett, P. D., Robinson, T. D., & Loeffler, M. J. (2020). Compaction of porous H₂O ice via energetic electrons. *The Astrophysical Journal*, 900, 147.
- Berdis, J. R., Gudipati, M. S., Murphy, J. R., et al. (2020). Europa's surface water ice crystallinity: Discrepancy between observations and thermophysical and particle flux modeling. *Icarus*, 341, 113660.
- Berger, M. J., Coursey, J. S., Zucker, M. A., et al. (2005), *ESTAR, PSTAR, and ASTAR: Computer Programs for Calculating Stopping-Power and Range Tables for Electrons, Protons, and Helium Ions* (version 1.2.3).
- Brown, W. L., Lanzerotti, L. J., & Johnson, R. E. (1982). Fast ion bombardment of ices and its astrophysical implications. *Science*, 218, 525.
- Campbell, I. M., & Gray, C. N. (1973). Rate constants for O (3P) recombination and association with N (4S). *Chemical Physics Letters*, 18, 607.
- Carlson, R. W., Anderson, M. S., Johnson, R. E., et al. (1999). Hydrogen peroxide on the surface of Europa. *Science*, 283(5410), 2062-2064.
- Carlson, R. W., Anderson, M. S., Johnson, R. E., et al. (2002). Sulfuric acid production on Europa: The radiolysis of sulfur in water ice. *Icarus*, 157, 456.
- Cassidy, T., Coll, P., Raulin, F., et al. (2010). Radiolysis and photolysis of icy satellite surfaces: experiments and theory. *Space Science Reviews*, 153, 299.
- Chyba, C. F. (2000). Energy for microbial life on Europa. *Nature*, 403, 381.
- Chen, M. M., Wetmore, R. W., & Schaefer III, H. F. (1981). Mechanism of the H⁺ O₃ reaction. *The Journal of Chemical Physics*, 74, 2938.

- Cook, A. M., Ricca, A., Mattioda, A. L., et al. (2015). Photochemistry of polycyclic aromatic hydrocarbons in cosmic water ice: The role of PAH ionization and concentration. *The Astrophysical Journal*, 799, 14.
- Cooper, J. F., Johnson, R. E., Mauk, B. H., et al. (2001). Energetic ion and electron irradiation of the icy Galilean satellites. *Icarus*, 149, 133.
- Davis, M. R., Meier, R. M., Cooper, J. F., et al. (2021). The contribution of electrons to the sputter-produced O₂ exosphere on Europa. *The Astrophysical Journal Letters*, 908, L53.
- De Cobos, A. C., & Troe, J. (1984). High-pressure range of the recombination O⁺ O₂ → O₃. *International Journal of Chemical Kinetics*, 16, 1519.
- Denisova, T. G. (2007). Kinetics and thermodynamics of the exchange reactions of peroxy radicals with hydroperoxides. *Kinetics and Catalysis*, 48, 609.
- Ding, J. J., Boduch, P., Domaracka, A., et al. (2013). Implantation of multiply charged sulfur ions in water ice. *Icarus*, 226, 860.
- Drouin, D., Couture, A. R., Joly, D., et al. (2007). CASINO V2. 42—a fast and easy-to-use modeling tool for scanning electron microscopy and microanalysis users. *Scanning: The Journal of Scanning Microscopies*, 29, 92.
- Galli, A., Vorburger, A., Wurz, P., et al. (2018). 0.2 to 10 keV electrons interacting with water ice: Radiolysis, sputtering, and sublimation. *Planetary and Space Science*, 155, 91.
- Gladstone, G. R., Allen, M., & Yung, Y. L. (1996). Hydrocarbon photochemistry in the upper atmosphere of Jupiter. *Icarus*, 119, 1.
- Gomis, O., Leto, G., & Strazzulla, G. (2004). Hydrogen peroxide production by ion irradiation of thin water ice films. *Astronomy & Astrophysics*, 420, 405.
- Gudipati, M. S. (2004). Matrix-isolation in cryogenic water-ices: Facile generation, storage, and optical spectroscopy of aromatic radical cations. *The Journal of Physical Chemistry A*, 108, 4412.
- Gudipati, M. S., & Allamandola, L. J. (2003). Facile generation and storage of polycyclic aromatic hydrocarbon ions in astrophysical ices. *The Astrophysical Journal Letters*, 596, L195.
- Hall, D. T., Strobel, D. F., Feldman, P. D., et al. (1995). Detection of an oxygen atmosphere on Jupiter's moon Europa. *Nature*, 373, 677.

- Hand, K. P., Chyba, C. F., Carlson, R. W., & Cooper, J. F. (2006). Clathrate hydrates of oxidants in the ice shell of Europa. *Astrobiology*, 6, 463.
- Hand, K. P., Carlson, R. W., & Chyba, C. F. (2007). Energy, chemical disequilibrium, and geological constraints on Europa. *Astrobiology*, 7, 1006.
- Hand, K. P., & Carlson, R. W. (2011). H₂O₂ production by high-energy electrons on icy satellites as a function of surface temperature and electron flux. *Icarus*, 215, 226.
- Hand, K. P., & Brown, M. E. (2013). Keck II observations of hemispherical differences in H₂O₂ on Europa. *The Astrophysical Journal Letters*, 766, L21.
- Heide, H. G. (1984). Observations on ice layers. *Ultramicroscopy*, 14, 271.
- Howell, S. M., & Pappalardo, R. T. (2018). Band formation and ocean-surface interaction on Europa and Ganymede. *Geophysical Research Letters*, 45, 4701.
- Javoy, S., Naudet, V., Abid, S., et al. (2003). Elementary reaction kinetics studies of interest in H₂ supersonic combustion chemistry. *Experimental Thermal and Fluid Science*, 27, 371.
- Johnson, R. E., & Jesser, W. A. (1997). O₂/O₃ microatmospheres in the surface of Ganymede. *The Astrophysical Journal Letters*, 480, L79.
- Johnson, R. E., Quickenden, T. I., Cooper, P. D., et al. (2003). The production of oxidants in Europa's surface. *Astrobiology*, 3, 823.
- Johnson, R. E., Cooper, P. D., Quickenden, T. I., et al. (2005). Production of oxygen by electronically induced dissociations in ice. *The Journal of Chemical Physics*, 123, 184715.
- Johnson, R. E., Burger, M. H., Cassidy, T. A., et al. (2009). Composition and detection of Europa's sputter-induced atmosphere. *Europa, University of Arizona Press, Tucson*, 507.
- Lee, M. W., & Meuwly, M. (2014). Diffusion of atomic oxygen relevant to water formation in amorphous interstellar ices. *Faraday Discussions*, 168, 205.
- Li, J., Gudipati, M. S., & Yung, Y. L. (2020). The influence of Europa's plumes on its atmosphere and ionosphere. *Icarus*, 352, 113999.
- Ligier, N., Poulet, F., Carter, J., et al. (2016). VLT/SINFONI observations of Europa: New insights into the surface composition. *The Astronomical Journal*, 151, 163.
- Loeffler, M. J., Raut, U., Vidal, R. A., Baragiola, R. A., & Carlson, R. W. (2006). Synthesis of hydrogen peroxide in water ice by ion irradiation. *Icarus*, 180, 265.

- Loeffler, M. J., Hudson, R. L., Moore, M. H., et al. (2011). Radiolysis of sulfuric acid, sulfuric acid monohydrate, and sulfuric acid tetrahydrate and its relevance to Europa. *Icarus*, 215, 370.
- Loeffler, M. J., Tribbett, P. D., Cooper, J. F., et al. (2020). A possible explanation for the presence of crystalline H₂O-ice on Kuiper Belt objects. *Icarus*, 351, 113943.
- Madey, T. E., Johnson, R. E., & Orlando, T. M. (2002). Far-out surface science: Radiation-induced surface processes in the solar system. *Surface Science*, 500, 838.
- Meier, R. M., & Loeffler, M. J. (2020). Sputtering of water ice by keV electrons at 60 K. *Surface Science*, 691, 121509.
- Moore, M. H. (1984). Studies of proton-irradiated SO₂ at low temperatures: Implications for Io. *Icarus*, 59, 114.
- Moore, M. H., Hudson, R. L., & Carlson, R. W. (2007). The radiolysis of SO₂ and H₂S in water ice: Implications for the icy jovian satellites. *Icarus*, 189, 409.
- Nordheim, T. A., Hand, K. P., & Paranicas, C. (2018). Preservation of potential biosignatures in the shallow subsurface of Europa. *Nature Astronomy*, 2, 673.
- Orlando, T. M., & Sieger, M. T. (2003). The role of electron-stimulated production of O₂ from water ice in the radiation processing of outer solar system surfaces. *Surface Science*, 528, 1.
- Parkinson, C. D., Liang, M. C., Hartman, H., et al. (2007). Enceladus: Cassini observations and implications for the search for life. *Astronomy & Astrophysics*, 463, 353.
- Petrik, N. G., Kavetsky, A. G., & Kimmel, G. A. (2006). Electron-stimulated production of molecular oxygen in amorphous solid water on Pt (111): Precursor transport through the hydrogen bonding network. *The Journal of Chemical Physics*, 125, 124702.
- Roth, O., & LaVerne, J. A. (2011). Effect of pH on H₂O₂ production in the radiolysis of water. *The Journal of Physical Chemistry A*, 115, 700.
- Sangwan, M., Chesnokov, E. N., & Krasnoperov, L. N. (2012). Reaction OH⁺ OH studied over the 298–834 K temperature and 1-100 bar pressure ranges. *The Journal of Physical Chemistry A*, 116, 6282.
- Shematovich, V. I., Johnson, R. E., Cooper, J. F., et al. (2005). Surface-bounded atmosphere of Europa. *Icarus*, 173, 480.

- Smyth, W. H., & Marconi, M. L. (2006). Europa's atmosphere, gas tori, and magnetospheric implications. *Icarus*, 181, 510.
- Snow, K. B., & Thomas, T. F. (1990). Mass spectrum, ionization potential, and appearance potentials for fragment ions of sulfuric acid vapor. *International Journal of Mass Spectrometry and Ion Processes*, 96, 49.
- Spencer, J. R., & Calvin, W. M. (2002). Condensed O₂ on Europa and Callisto. *The Astronomical Journal*, 124, 3400.
- Strazzulla, G., Baratta, G. A., Leto, G., et al. (2007). Hydrate sulfuric acid after sulfur implantation in water ice. *Icarus*, 192, 623.
- Teolis, B. D., Vidal, R. A., Shi, J., et al. (2005). Mechanisms of O₂ sputtering from water ice by keV ions. *Physical Review B*, 72, 245422.
- Teolis, B. D., Shi, J., & Baragiola, R. A. (2009). Formation, trapping, and ejection of radiolytic O₂ from ion-irradiated water ice studied by sputter depth profiling. *The Journal of Chemical Physics*, 130, 134704.
- Teolis, B. D., Jones, G. H., Miles, P. F., et al. (2010). Cassini finds an oxygen–carbon dioxide atmosphere at Saturn's icy moon Rhea. *Science*, 330, 1813.
- Teolis, B. D., Plainaki, C., Cassidy, T. A., et al. (2017a). Water ice radiolytic O₂, H₂, and H₂O₂ yields for any projectile species, energy, or temperature: A model for icy astrophysical bodies. *Journal of Geophysical Research: Planets*, 122, 1996.
- Teolis, B. D., Wyrick, D. Y., Bouquet, A., et al. (2017b). Plume and surface feature structure and compositional effects on Europa's global exosphere: Preliminary Europa mission predictions. *Icarus*, 284, 18.
- Tsang, W., & Hampson, R. F. (1986). Chemical kinetic data base for combustion chemistry. Part I. Methane and related compounds. *Journal of Physical and Chemical Reference Data*, 15, 1087.
- Vorburger, A., & Wurz, P. (2018). Europa's ice-related atmosphere: The sputter contribution. *Icarus*, 311, 135.
- Yung, Y. L., and W. B. DeMore (1999), Photochemistry of Planetary Atmospheres, pp. 258, *Oxford Univ. Press, New York*.

Zheng, W., Jewitt, D., & Kaiser, R. I. (2006). Temperature dependence of the formation of hydrogen, oxygen, and hydrogen peroxide in electron-irradiated crystalline water ice. *The Astrophysical Journal*, 648, 753.

Zheng, W., Jewitt, D., & Kaiser, R. I. (2009). On the state of water ice on Saturn's moon Titan and implications to icy bodies in the outer solar system. *The Journal of Physical Chemistry A*, 1130, 11174.

Part 2: Sulfur Chemistry on Venus

A POSSIBLE CANDIDATE OF THE ENIGMATIC ULTRAVIOLET ABSORBER(S) IN THE UPPER ATMOSPHERE OF VENUS

3.1 Abstract

Ever since the detection of the enigmatic ultraviolet (UV) absorption in the upper atmosphere of Venus, questions have been raised about the identity of the unknown UV-visible absorber(s) and how it is formed on Venus. The recent photochemical modelling study suggests that SO dimers may not be the major UV absorber(s) in Venus' upper atmosphere. However, SO dimers are important intermediaries in the formation of more complex S species (e.g., S_n (n = 1 to 7)). Polysulfur aerosol, which is formed from the nucleation processes of S_n (n = 1 to 7), is a possible candidate for the unknown UV absorber(s). In this work, we compute that the mixing ratio of polysulfur aerosol is $\sim 1.76 \times 10^{-14}$ in the upper atmosphere. By putting the polysulfur aerosol into the Spectral Mapping Atmospheric Radiative Transfer model (SMART), we find that the simulated spectrum of Venus agrees well with the observations. This result provides useful constraints for unraveling the identity(ies) of the unknown UV-visible absorber(s) on Venus.

3.2 Introduction

Venus has a high albedo due to the existence of clouds in its atmosphere. The image of Venus is featureless in the visible wavelength, but a high contrast of bright and dark features occurs in the ultraviolet wavelength (Yamazaki et al., 2018). It is generally understood that the UV absorption from 200 nm to 300 nm is due to the existence of SO₂ in Venus' atmosphere (Zasova et al., 1981). However, what chemical species absorb the photons from 300 nm to 500 nm is still an open question. Although there is no consensus on the species of the unknown UV absorber(s), people already know that the absorber(s) is mainly distributed in upper cloud region, which is around 58 to 72 km above Venus' surface. Hypothetical vertical profiles and the corresponding absorbing spectrum of the UV absorber(s) have been created by Haus et al. (2015). Ever since the detection of the UV absorption in the atmosphere of

Venus, people have done numerous studies trying to identify the absorber(s). The candidates for the UV absorption include S_3 (Toon et al., 1982), S_4 (Toon et al., 1982), S_8 (Hapke and Nelson, 1975), S_2O (Hapke and Graham, 1989), SO dimers (Frandsen et al., 2016), S_2Cl_2 (Krasnopolsky, 1986), $(NH_4)_2S_2O_5$ (Titov, 1983), $NOHSO_4$ (Watson et al., 1979), Cl_2 (Pollack et al., 1980), $FeCl_3$ (Krasnopolsky, 1985) and $C_5O_5H_2$ (Hartley et al., 1989). In this study, we propose that polysulfur aerosol is a possible candidate of the enigmatic UV absorber(s) in the atmosphere of Venus. In the next section, we will first calculate the generation rate profile of the polysulfur aerosol in Venus' atmosphere based on a chemical-transport model. We will estimate the mixing ratio of the polysulfur aerosol in the critical UV absorption region according to its generation rate profile. Then we will use a radiative transfer model to examine how well the optical properties of the polysulfur aerosol fit the spectrum of Venus.

3.3 Methods

In this study, we adopt the latest version of the Caltech/JPL one-dimensional chemical-transport model KINETICS from Pinto et al. (2021). This model includes the OSSO-related chemical and photochemical reactions. Since cis-OSSO is one of the major S_2 sources and cyclic-OSSO is one of the major S sources in Venus' upper atmosphere, SO dimers are important intermediaries in the formation of S_n ($n = 1$ to 7) in the atmosphere (Pinto et al., 2021). Polysulfur aerosols in the atmosphere are formed from the heterogeneous nucleation process of the elemental sulfur (S_n), whose reaction rate is calculated in our model. More details about how the nucleation rate constant is calculated can be found in Zhang et al. (2012).

To simplify the problem, we assume that the mixing ratio of polysulfur aerosol in the critical UV absorption region (58 to 72 km) is a constant. To calculate this mixing ratio, we first integrate the total transforming rate of elemental sulfur to polysulfur aerosol. The radius of an aerosol is assumed to be 0.1 micron, which contains $\sim 1.6 \times 10^8$ S atoms. Then the production rate of polysulfur aerosol can be calculated from the transforming rate of elemental sulfur. The major loss mechanism of polysulfur aerosol is the downward flow at

the lower boundary of the absorption region (58 km). The velocity of the downward flow is assumed to be the eddy velocity, which is defined as the ratio between the eddy diffusion coefficient and the scale height. The mixing ratio of polysulfur aerosol is estimated based on the balance between the production and the loss.

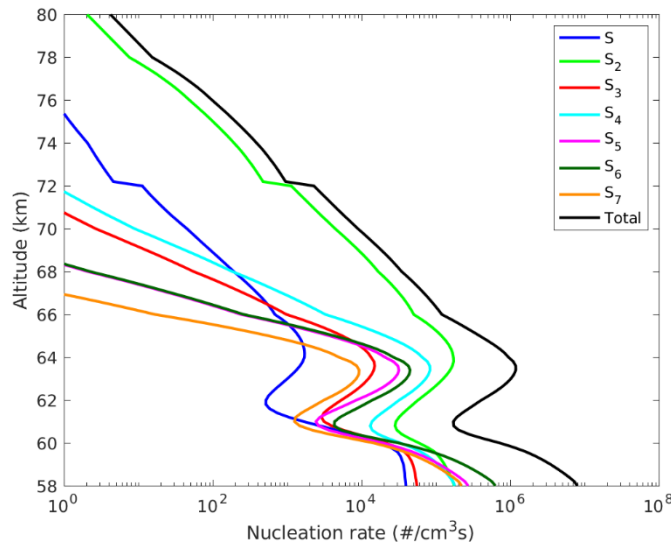


Figure 3.1: The profiles of the nucleation rate of S_n ($n = 1$ to 7) and the total transforming rate of elemental sulfur to polysulfur aerosol.

To examine the influence of polysulfur aerosol on the spectrum of Venus, we use the Spectral Mapping Atmospheric Radiative Transfer Model (SMART) to simulate the reflectance spectrum of Venus. SMART is a well-known one-dimensional, multiple scattering, line-by-line radiative transfer model. More details about the SMART can be found in Meadows and Crisp (1996). Here we consider 5 cases of the UV absorber(s) in the atmosphere of Venus: (1) no unknown UV absorber(s); (2) the retrieved UV absorber(s) from Haus et al. (2015); (3) our estimated polysulfur aerosol; (4) polysulfur aerosol with the mixing ratio twice of the estimation; (5) polysulfur aerosol with the mixing ratio one twice of the estimation. Comparing between case (2) and case (3), we can see if polysulfur aerosol is a possible candidate for the UV absorber(s). Cases (4) and (5) are used to test the sensitivity of the reflectance spectrum to the abundance of polysulfur aerosol in the atmosphere. The absorption cross section of polysulfur aerosol used in SMART is calculated based on the absorption coefficient of polymorphic sulfur by Hapke and Nelson (1975). Since the

absorption coefficient below 400 nm is missing in Hapke and Nelson (1975), we use the retrieved absorption cross section of the UV absorber(s) from Haus et al. (2015) to extrapolate the absorption cross section of polysulfur aerosol below 400 nm.

3.4 Results and Discussion

The profiles of the nucleation rate of S_n and the total transforming rate of elemental sulfur to polysulfur aerosol are shown in Figure 3.1. Integrating the transforming rate of elemental sulfur above 58 km and considering that an aerosol contains $\sim 1.6 \times 10^8$ S atoms, we obtain a polysulfur aerosol production rate of $\sim 7.5 \times 10^3 \text{ cm}^{-2}\text{s}^{-1}$. Consider that the eddy velocity is $\sim 4.75 \times 10^2 \text{ cm/s}$ at 58 km, we estimate that the density of polysulfur aerosol at 58 km is $\sim 1.58 \times 10^5 \text{ cm}^{-3}$, which corresponds to a mixing ratio of $\sim 1.76 \times 10^{-14}$. The mixing ratio profile of polysulfur aerosol and its absorption cross section spectrum are shown in Figure 3.2a and 3.2b, respectively.

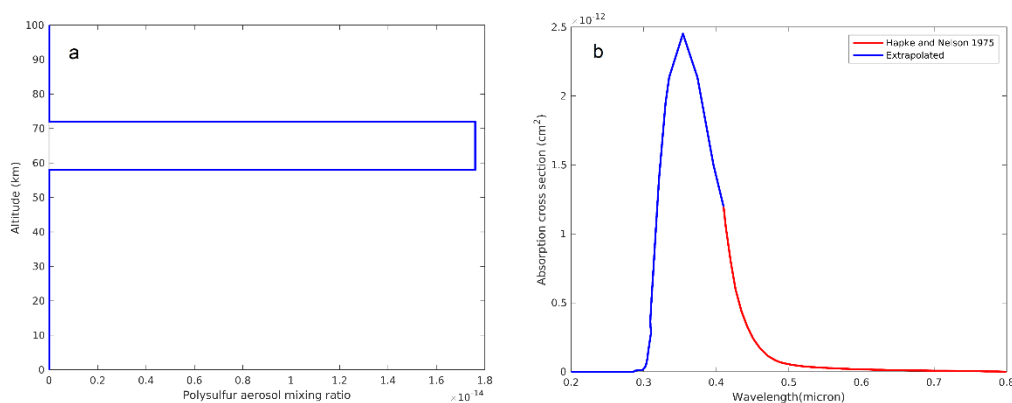


Figure 3.2: The properties of the polysulfur aerosol in Venus' atmosphere. (a) The mixing ratio profile of polysulfur aerosol. (b) The absorption cross section spectrum of polysulfur aerosol.

The simulated reflectance spectrum of the 5 cases is shown in Figure 3.3. Comparing the spectrum of the retrieved UV absorber(s) (red line) with polysulfur aerosol (green line), we can see that spectrum of polysulfur aerosol agrees well with the spectrum of the unknown UV absorber(s) in the upper atmosphere of Venus, especially in the wavelength below 450 nm. This suggests that polysulfur aerosol is a possible candidate of the enigmatic UV

absorber(s) in the atmosphere of Venus. Our sensitivity test shows that the spectrum of Venus' atmosphere is considerably sensitive to the abundance of polysulfur aerosol in the atmosphere. With the abundance going upward or downward by a factor of 2, the reflectance in the critical wavelength range (350-400 nm) goes downward or upward to 15%.

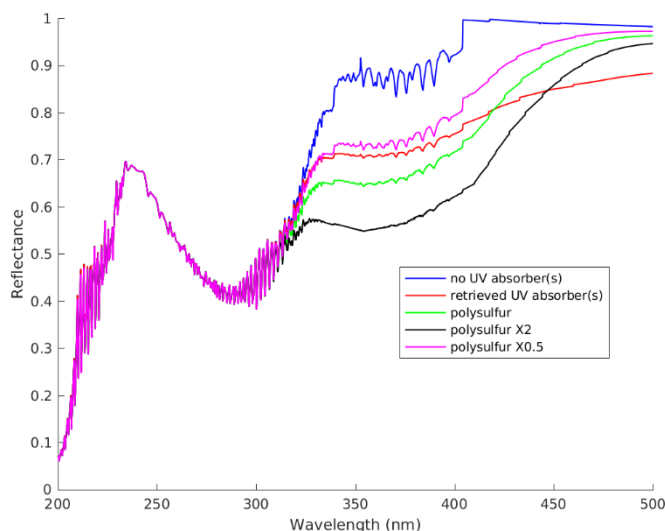


Figure 3.3: The spectrum of the atmosphere of Venus with 5 cases of UV absorber(s): (1) no unknown UV absorber(s); (2) the retrieved UV absorber(s) from Haus et al. (2015); (3) our estimated polysulfur aerosol; (4) polysulfur aerosol with the mixing ratio twice of the estimation; (5) polysulfur aerosol with the mixing ratio one twice of the estimation.

It should be noted that the absorption cross section of polysulfur aerosol below 400 nm is extrapolated. If the more comprehensive experimental study of the optical properties of polysulfur aerosol is available in the future, we will be able to obtain a more realistic simulation of the reflectance spectrum and better understand the influence of polysulfur aerosol on the spectrum of Venus. In this study, we only consider the heterogeneous nucleation processes above 58 km. The nucleation processes below 58 km and the homogeneous nucleation processes, which may also influence the mixing ratio of polysulfur aerosol in the atmosphere, need to be considered in the future study. We need to keep in mind that the enigmatic UV absorption in the upper atmosphere of Venus may not be caused by a single species. Although spectrum of the atmosphere that contains polysulfur aerosol agrees well with the enigmatic UV absorption, a combination of various condensed and gas phase

UV absorbing species (e.g., OSSO, FeCl₃) is more likely to be accounting for the UV absorption on Venus.

References

- Hapke, B., & Graham, F. (1989). Spectral properties of condensed phases of disulfur monoxide, polysulfur oxide, and irradiated sulfur. *Icarus*, 79(1), 47-55.
- Hapke, B., & Nelson, R. (1975). Evidence for an elemental sulfur component of the clouds from Venus spectrophotometry. *Journal of Atmospheric Sciences*, 32(6), 1212-1218.
- Hartley, K. K., Wolff, A. R., & Travis, L. D. (1989). Croconic acid: An absorber in the Venus clouds? *Icarus*, 77(2), 382-390.
- Haus, R., Kappel, D., & Arnold, G. (2015). Radiative heating and cooling in the middle and lower atmosphere of Venus and responses to atmospheric and spectroscopic parameter variations. *Planetary and Space Science*, 117, 262-294.
- Krasnopolsky, V. A. (1985). Chemical composition of Venus clouds. *Planetary and Space Science*, 33(1), 109-117.
- Krasnopolsky, V. A. (1986). *Photochemistry of the atmosphere of Mars and Venus*. Berlin: Springer-Verlag.
- Meadows, V. S., & Crisp, D. (1996). Ground-based near-infrared observations of the Venus nightside: The thermal structure and water abundance near the surface. *Journal of Geophysical Research: Planets*, 101(E2), 4595-4622.
- Pinto, J. P., Li, J., Mills, F. P., Marcq, E., Evdokimova, D., Belyaev, D., & Yung, Y. L. (2021). Sulfur monoxide dimer chemistry as a possible source of polysulfur in the upper atmosphere of Venus. *Nature Communications*, 12(1), 1-6.
- Pollack, J. B., Toon, O. B., Whitten, R. C., et al. (1980). Distribution and source of the UV absorption in Venus' atmosphere. *Journal of Geophysical Research: Space Physics*, 85(A13), 8141-8150.
- Titov, D. V. (1983). On a possibility of aerosol production in the chemical reaction between SO₂ and NH₃ in conditions of the Venus atmosphere. *Kosmicheskie Issledovaniya*, 21(3), 401-409.

- Toon, O. B., Turco, R. P., & Pollack, J. B. (1982). The ultraviolet absorber on Venus: Amorphous sulfur. *Icarus*, 51(2), 358-373.
- Watson, A. J., Donahue, T. M., Stedman, D. H., Knollenberg, R. G., Ragent, B., & Blamont, J. (1979). Oxides of nitrogen and the clouds of Venus. *Geophysical Research Letters*, 6(9), 743-746.
- Yamazaki, A., Yamada, M., Lee, Y. J., et al. (2018). Ultraviolet imager on Venus orbiter Akatsuki and its initial results. *Earth, Planets, and Space*, 70(1), 1-11.
- Zasova, L. V., Krasnopolsky, V. A., & Moroz, V. I. (1981). Vertical distribution of SO₂ in upper cloud layer of Venus and origin of UV-absorption. *Advances in Space Research*, 1(9), 13-16.
- Zhang, X., Liang, M. C., Mills, F. P., Belyaev, D. A., & Yung, Y. L. (2012). Sulfur chemistry in the middle atmosphere of Venus. *Icarus*, 217(2), 714-739.

*Chapter IV*STUDY OF TERRESTRIAL GLINTS BASED ON DSCOVER
OBSERVATIONS

This chapter is adapted from work previously published as

Li, J. Z., Fan, S., Kopparla, P., Liu, C., Jiang, J. H., Natraj, V., & Yung, Y. L. (2019). Study of terrestrial glints based on DSCOVER observations. *Earth and Space Science*, 6(1), 166-173. <https://doi.org/10.1029/2018EA000509>.

4.1 Abstract

Small flashes of reflected light, called glints, are found in images taken by spacecraft observing the Earth and occur due to specularly reflected solar radiation. These glints have been found over both ocean and land. Using Deep Space Climate Observatory (DSCOVER) observations, we show that glints over land are due to specular reflection off horizontally oriented ice platelets floating in the air, while glints over ocean have contributions from reflection off either platelets floating above the ocean or a relatively smooth ocean surface. We use a radiative transfer model to simulate different kinds of glints and to explore their properties. This technique of comparing observations of terrestrial glints with model simulations may provide new information relevant to atmospheric dynamics and the search for habitable exoplanets.

4.2 Introduction

Glints, small flashes of reflected light, found in images taken by spacecraft observing the Earth are generally believed to be due to specularly reflected solar radiation. The study of glints dates back to 1993, when Sagan et al. (1993) used the Galileo spacecraft's December 1990 fly-by of Earth to constitute a control experiment for the search for extraterrestrial life. It is evident from the Galileo images that glints occur over both ocean (Sagan et al., 1993) and land (Marshak et al., 2017). In a recent study on glints using the Earth Polychromatic

Imaging Camera (EPIC) on board the Deep Space Climate Observatory (DSCOVR) spacecraft, Marshak et al. (2017) further confirm that glints can be found over land. The glints over land are proposed to be due to horizontally oriented ice platelets floating in cirrus clouds (Marshak et al., 2017); existence of such platelets has been confirmed by prior atmospheric observations (Breon and Dubrulle, 2004; Noel and Chepfer, 2004, 2010; Zhou et al., 2012).

In this paper, we use DSCOVR observations to search for glints not only over land but also over the ocean. For glints over the ocean, there are two sources: ice platelets in the clouds above the ocean, and ocean waves. We discuss the properties of the two sources and separate glints with different sources based on their spectral properties. We also employ a radiative transfer (RT) model to simulate terrestrial glints and reproduce their signatures in the DSCOVR observations.

4.3 Glint Mechanism

For a glint to appear in an image taken by a spacecraft, the reflecting material needs to specularly reflect the incoming sunlight to the Vehicle (spacecraft). For this to happen, the reflecting material, the Sun and the Vehicle have to form a specific geometry that is determined by the orientation of the material. If the reflecting material is horizontal (i.e. perpendicular to the local surface normal) and has a smooth surface, the Vehicle can receive the glint signal only if the material is in the Sun-Earth-Vehicle plane (see Figure 4.1a). Since the distance between the Vehicle and the Earth is much larger than the radius of the Earth (DSCOVR observes the Earth from the first Lagrangian point at 1.5 million km away), the angle between the reflected sunlight ray and the line connecting the center of the Earth and the Vehicle is negligible. The same is also true for the angle between the incoming sunlight ray and the line connecting the Sun and the center of the Earth. Therefore, in this scenario, the sum of the solar zenith angle (SZA) and the vehicle zenith angle (VZA) must equal the Sun-Earth-Vehicle (SEV) angle.

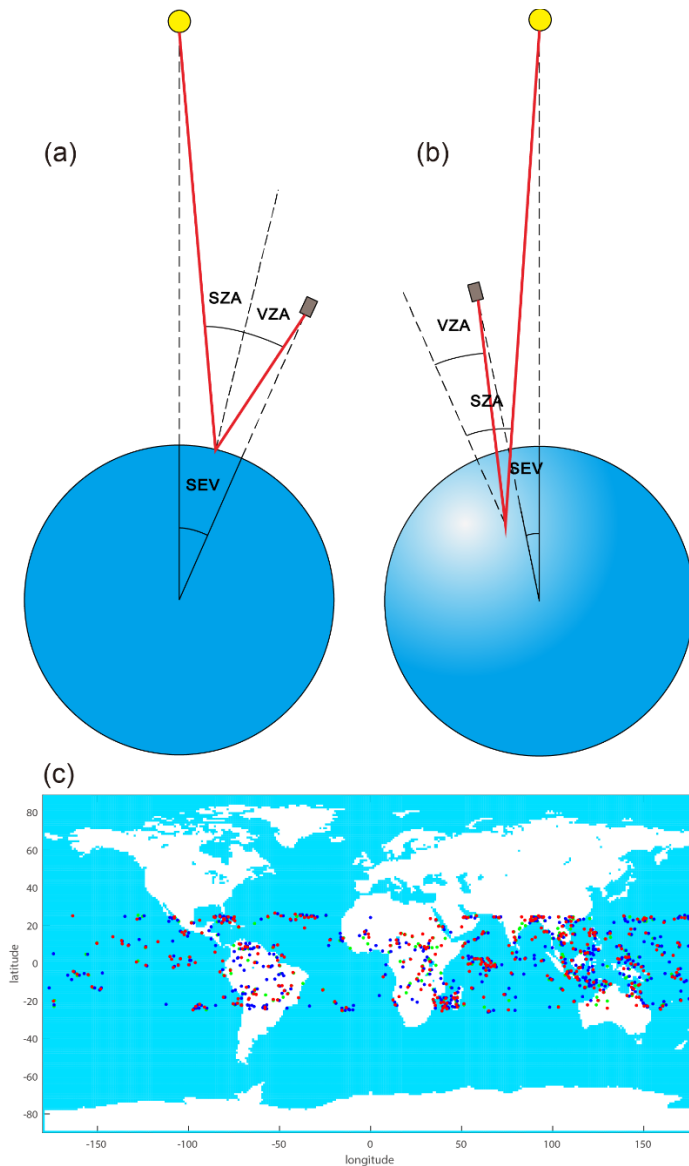


Figure 4.1: An illustration of the glint mechanism for (a) horizontal and (b) tilted reflecting materials. The small yellow circle represents the sun, the large blue circle is the Earth and the small brown rectangle represents the vehicle. The black dashed lines show the normal directions of the corresponding surfaces and the red solid lines show the rays of light. (c) Global distribution of glints.

If the reflecting material is not horizontal, for a glint to appear in an image taken by DSCOVER, the material needs to be out of the Sun-Earth-Vehicle plane (see Figure 4.1b). Since the material is out of the plane, the sum of SZA and VZA in this scenario is larger than the corresponding sum in the horizontal scenario. In other words, for a glint caused by tilted

reflecting material, $SZA + VZA > SEV$. Therefore, the orientation of the reflecting material can be determined from the relation between SZA , VZA , and SEV .

4.4 Observations

In this section, we use 20 months of data (July 2015–March 2017) from DSCOVR. EPIC, the spectroradiometer with 10 narrow bands (317.5 nm–779.5 nm) onboard DSCOVR, images the entire sunlit face of the Earth every 1–2 hours using a 2048×2048 pixel charged-coupled device (CCD) (Herman et al., 2018). The original data from EPIC is in units of counts s^{-1} ; we employ the EPIC calibration factors K from Geogdzhayev et al. (2017) to convert to reflectance units.

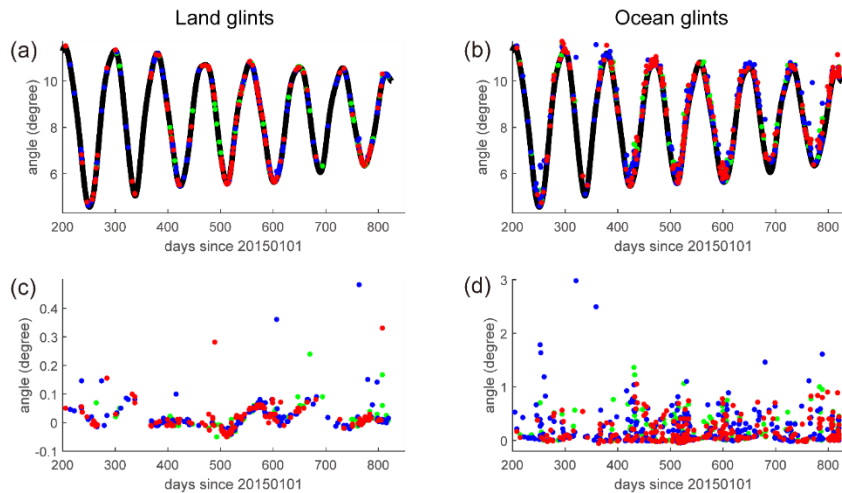


Figure 4.2: Comparison between SEV and $SZA + VZA$. (a) Comparison between SEV and the $SZA + VZA$ for land glints; (b) Same as (a) but for ocean glints; (c) Difference between $SZA + VZA$ and SEV for land glints; (d) Same as (c), but for ocean glints.

Although EPIC takes the Earth images in 10 channels, we only use three of them, *viz.* the blue (443 nm), green (551 nm) and red (680 nm) channels to search for glints because these channels are more sensitive to the existence of specularly reflecting materials and less sensitive to other factors such as ozone absorption and surface types compared to the other channels. Here we use the first ultraviolet channel (317.5 nm) as the baseline. In each image, if a pixel has a reflectance in at least one of the blue, green or red channels that is more than *three* times larger than the reflectance in the first ultraviolet channel, we regard it as a glint

pixel. Since EPIC uses a rotating filter wheel to take images of the Earth in 10 channels, the images at different wavelengths are taken at different times; therefore, the glints appear in different colors. The color code (blue, green, or red) of each glint pixel is specified by the channel with the highest reflectance of the three. Since the reflecting materials for one glint may be distributed over a large area on Earth and cover multiple pixels, there could be more than one glint pixel in each image. However, it should be noted that since each CCD pixel can only store a finite number of electrons, if the reflected sunlight in one pixel is very strong, that pixel will be saturated, and the extra electrons generated by the sunlight will spread to the nearby pixels. Here we assume that all of the contiguous glint pixels belong to one glint, and the properties of the glint (SZA, VZA, reflectance, etc.) are represented by the properties of the glint pixel that has the highest reflectance. Using the aforementioned method, we identify 967 blue glints, 562 green glints, and 586 red glints out of 6817 images of the Earth taken by DSCOVR. To avoid possible false positives in the glint signal, we eliminate all the glints that contain less than 10 pixels. This procedure yields 478 blue glints, 349 green glints, and 367 red glints. Their global distribution is shown in Figure 4.1c. The following analysis will be carried on for glints that contain at least 10 pixels.

Glints are separated into two groups based on their geographic positions: land glints and ocean glints. Figure 4.2 compares the sum of SZA and VZA with SEV for the two groups of glints. In Figures 4.2a and 4.2b, the black line represents the SEV as a function of time, while the abscissa and ordinate of each colored dot represent the time and the sum of SZA and VZA of a land/ocean glint, respectively. The difference between $SZA + VZA$ and SEV is retrieved for both land and ocean glints, and the results are shown in Figures 4.2c and 4.2d, respectively. For most of the land glints, the difference between $SZA + VZA$ and SEV is close to zero, which suggests that the reflecting materials are nearly horizontal. For the ocean glints, however, the difference could reach relatively large values of up to ~ 3 degrees, suggesting that the reflecting materials could tilt $\sim 2\text{--}3$ degrees away from the horizontal orientation.

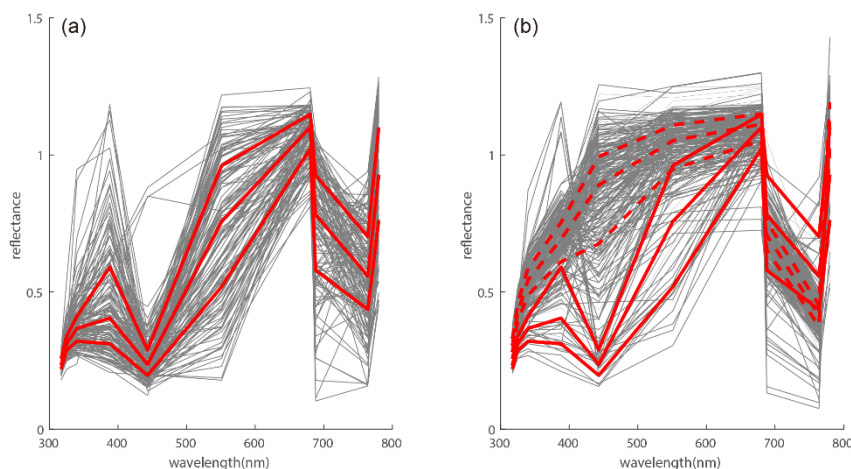


Figure 4.3: Spectra of the glints. (a) Spectra of red land glints; (b) Spectra of red ocean glints.

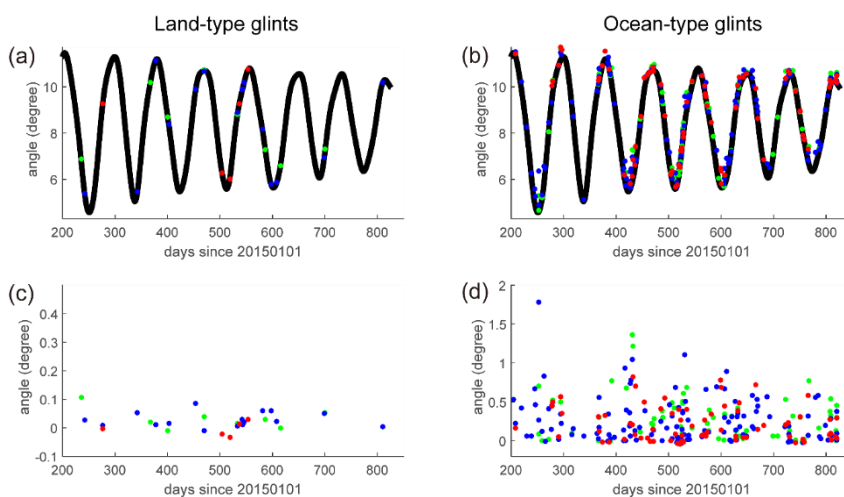


Figure 4.4: Comparison between SEV and SZA + VZA for two types of glints. (a) Comparison between SEV and SZA + VZA for land-type glints; (b) Same as (a) but for ocean-type glints; (c) Difference between SZA + VZA and SEV for land-type glints; (d) Same as (c) but for ocean-type glints.

Note that land glints do not correspond to known water bodies (lakes, rivers, etc.); it is most likely that they are due to specular reflection off horizontally oriented ice platelets. This can be confirmed (Marshak et al., 2017) by calculating the ratio of EPIC reflectances from absorbing and nonabsorbing channels of O_2 , which gives an estimate of scattering layer height. However, ocean glints have two sources. Some of the glints come from the ocean surface, and others from ice platelets in cirrus clouds over the ocean. Glint spectra can be used to separate the two sources. Taking red glints as an example, spectra of land and ocean

glints (gray lines) are shown in Figures 4.3a and 4.3b, respectively. The 10 discrete values in each spectrum denote the reflectance in the EPIC channels. The three solid red lines in Figure 4.3a represent the lower quartile, median and upper quartile of the land glint spectra. The dotted red lines in Figure 4.3b denote the same, but for ocean glint spectra. Clearly, spectra of ocean glints are significantly different from those of land glints. Results for blue and green glints (not shown) show the same behavior. Some of the ocean glints have spectra that are similar to those of land glints, while some do not. All ocean glints that have reflectance between the lower and upper quartiles of land glint spectra in at least *seven* channels are identified as “land-type” glints, while those that have reflectance between the lower and upper quartiles of ocean glint spectra in at least *seven* channels are referred to as “ocean-type glints.” Figure 4.4 compares SZA + VZA with SEV for land-type glints and ocean-type glints, and is organized in the same manner as Figure 4.2. The distinct similarity between the land glints and the land-type ocean glints implies that reflection off horizontally oriented ice platelets indeed happens over the ocean as well.

It should be noted that the spectral difference between land and ocean glints is caused by the way EPIC operates and due to the different properties of ice platelets and water. The EPIC images at different wavelengths are taken at different times. For example, the image in the green channel is taken ~3 min later than that in the blue channel and ~1 min sooner than that in the red channel. Since the position of the reflecting material is basically fixed on Earth, the local surface normal changes as the Earth rotates. For glints caused by ice platelets, since the platelets are very flat, the glint geometry will disappear in a few minutes due to the change of local surface normal. If DSCOVER receives a glint signal in the red channel, we can still see a weaker signal in the nearby green channel; however, there is no discernible signal in the blue channel (see Figure 4.3a). For glints caused by the ocean, since the ocean is continuous, the change of local surface normal will not strongly weaken the glint signal; therefore, glint signals can be found in several channels (see Figure 4.3b).

4.5 Simulations

To better understand the previous results, the RT model developed by Kopparla et al. (2016) is adopted to reproduce the characteristics of terrestrial glints. We employ 16 computational quadrature angles (streams) for the RT calculations. Note that single scattering is treated exactly, using all moments of the scattering phase function. The reduced number of streams is only for the multiple scattering contribution. The core of the simulation is the one-dimensional vector RT model VLIDORT (Spurr, 2006). The Earth's surface is divided into a grid of boxes based on a quadrature scheme (Horak, 1950). At each point, the RT simulation is performed using a plane parallel Rayleigh scattering atmosphere (illustrated in Figure 4.5a). We use the real land-ocean distribution of the Earth in our simulation. For simplicity, we assume that land is a Lambertian surface with a reflectance of 0.2. If a point is not covered by cloud, then the surface type of this point is denoted as land or ocean (according to the land-ocean distribution) and the optical depth of the atmosphere is set to 0.1 (estimated based on results from Bodhaine et al. (1999) for the green channel). If a point is covered by cloud, the surface type of this point is denoted as cloud and the optical depth of the atmosphere is set to 0.05 (due to the fact that the atmospheric pressure is about 0.5 bar at the typical cirrus cloud altitude of 5.5 km).

Using EPIC measurements of absorption in oxygen A and B bands, Marshak et al. (2017) suggest that clouds that are responsible for glints have low optical depths ($\sim 1-3$) and that their heights are around 5–8 km, implying that they are made of ice. Using Cloud-Aerosol Lidar and Infrared Pathfinder Satellite Observation (CALIPSO) measurements, Noel and Chepfer (2010) and Zhou et al. (2012) find that horizontally oriented ice crystals commonly exist in warm ice clouds (-30°C to -10°C). In our model, we adopt randomly distributed cirrus clouds in the tropical area of the Earth with an occurrence rate of 25% (estimated from Figure 1 in Sassen et al. (2008)). We assume that half of the clouds are warm cirrus clouds with horizontal ice platelets and the other half are cold clouds without platelets. The cloud optical depth is assumed to be 2. Viewing from the top of the cloud, if $A\%$ of the ice particles in the clouds are horizontally oriented, then about $\int_0^2 A\% * e^{-\tau} d\tau \approx 0.865A\%$ of the cloud

area is covered by horizontal ice platelets. We assume the occurrence of ice platelets is uniformly distributed between 0% and 5%; then about 0% to 4.33% of the cloud area is covered by ice platelets and rest of the area is assumed to be a Lambertian surface with a reflectance of 0.3. It should be noted that the precise way to deal with ice cloud RT is to use the full phase matrix of oriented ice particles to describe their scattering properties (Yang et al., 2005; Bi et al., 2011; Zhou et al., 2012). However, this method is computationally expensive and beyond the scope of our study. Therefore, for the sake of simplicity, we treat the horizontally oriented ice platelets together as a large reflector rather than as multiple small particles to avoid using the full phase matrix of oriented ice particles. The proportion of the horizontally oriented ice platelets adopted in our model (0-5%) is consistent with Noel et al. (2010) (below 5%) but slightly larger than the proportion obtained by Zhou et al. (2012] (0-3%). To calculate the reflected sunlight from the cloud area covered by horizontal ice platelets, we simply adopt the Cox-Munk ocean reflection glint surface model (Cox and Munk, 1954), with a refractive index of 1.31 (corresponding to ice) and a surface wind speed of ~ 0.5 m/s (corresponding to a standard deviation of $\sim 1^\circ$). The output intensity of reflected sunlight from the point can be obtained as a linear combination of the intensity of the ice platelet and Lambertian portions.

To calculate the reflection off the ocean, we also adopt the Cox-Munk glint model, but with a refractive index of 1.333 (corresponding to water). Figure 2 in Monahan (2006) displays ocean surface wind speed data from SeaWinds, SSM/I, ERA-40, and NCEP-NCAR reanalysis datasets. An averaged mean wind velocity of ~ 7 m/s and an averaged standard deviation of ~ 3 m/s are estimated from that figure. For simplicity, we use a Gaussian distribution with the same mean and standard deviation to represent the ocean surface wind speed distribution. For each point whose surface type is ocean, we randomly generate a surface wind speed according to the distribution.

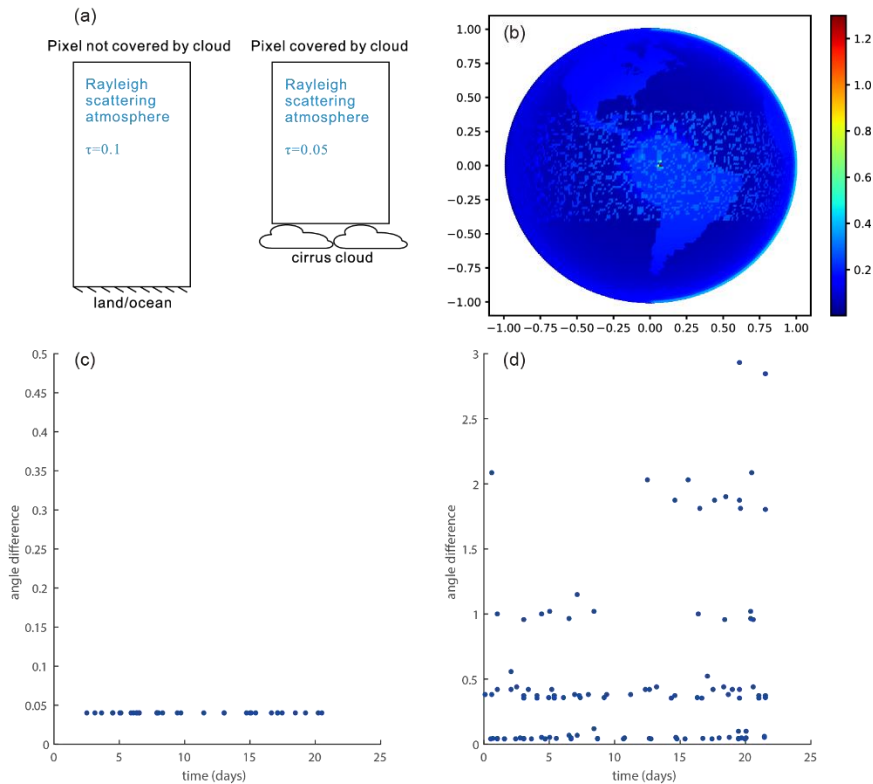


Figure 4.5: Simulation of glints. (a) An illustration of how pixels with different surface types are dealt with; (b) A virtual image of the Earth; (c) Difference between SZA + VZA and SEV for glints due to ice platelets; (d) Same as (c), but for glints due to ocean waves.

We set the SEV at 10 degrees to reproduce DSCOVR viewing geometry. The surface of the Earth is divided into 200×200 grids; the intensity and polarization of reflected sunlight at each grid point is calculated by employing the RT model described above. We then use the quadrature scheme described above to form images of the virtual Earth. An example of virtual images of the intensity (in reflectance units) is shown in Figure 4.5b. A very bright spot can be found in the middle part of Figure 4.5b; that is a land glint caused by horizontally oriented ice platelets. Since the polarization properties of ice clouds are not included in our model and since DSCOVR does not have a polarimeter onboard, the polarized part of the RT model is actually not used in this study. Polarization signals from ice clouds, ocean and ice platelets will be considered in future studies.

The rotation period of the Earth is considered in our simulations. We simulate reflected sunlight from the virtual Earth every 2.1 hours and for a total of ~ 21 days; ~ 250 virtual

images of the intensity are obtained. We select all points that have a reflectance higher than 1.2 from those images and define them as glints. Based on the reflecting material, the glints are divided into two groups: ice glints and ocean glints. The difference between $SZA + VZA$ and SEV is calculated for both ice and ocean glints and shown in Figures 4.5c and 4.5d, respectively. In Figure 4.5c, it is evident that the angle difference for ice glints is very close to 0, which is consistent with Figures 4.2c and 4.4c. The angle difference is not exactly equal to 0 because of the finite grid size in our simulation. The angle difference for ocean glints, however, shows a broad distribution from 0 degree to 3 degrees, which is consistent with Figures 4.2d and 4.4d. The consistency between simulations and observations suggests that the characteristics of terrestrial glints can be reproduced by our RT model despite its simplicity.

4.6 Summary and Discussion

This paper utilizes DSCOVR observations of the Earth to study the characteristics of terrestrial glints. Glints can be found over both land and ocean. We show that glints over land are due to horizontally oriented ice platelets in the cirrus cloud, while glints over ocean are due to both platelets floating above the ocean and ocean waves. Based on the glint geometry, we find that ocean, as a reflecting material for the glints, is often rough and tilted. Glints caused by the platelets have different type of spectra from those caused by the ocean; this distinction can help us separate ocean glints with two different sources and verify the global existence of the horizontal ice platelets.

Using a RT model, we construct a simple model to reproduce the terrestrial glints. Despite the fact that our cloud distribution, ice platelet and ocean surface models are very simple, the simulation results are generally consistent with the observations, which enables us to further understand the properties of reflecting materials on Earth. The ocean surface, acting as an enormous mirror on Earth, is usually very rough due the existence of surface winds. The ocean surface can be tilted up to several degrees and reflects sunlight over a broad spatial extent. The ice platelets in the cirrus clouds, on the other hand, are very flat and can only reflect sunlight in a narrow spatial region. Although the existence of horizontal ice crystals

in cirrus and mixed-phase clouds has been known for more than a decade, there is still limited understanding on the mechanisms behind their formation. This study motivates further research on the dynamics of ice crystals in clouds.

Although our simulation results (Figures 4.5c, and 4.5d) are generally consistent with the observations, they generate both ice and ocean glints more frequently than the observations. For the ice glints, the inconsistency may be due to our overestimation of warm cloud occurrence rate. It could also be due to the unrealistic uniform distribution of the proportion of horizontal ice platelets. Further studies on ice crystals in clouds are needed to improve our model. For the ocean glints, the high frequency may be due to the fact that we only consider a cirrus cloud distribution with an occurrence rate of 25%. If other kinds of clouds are considered, they could cover a larger fraction of the ocean surface and lower the occurrence rate of the ocean glints. Further, the cloud and surface wind speed distributions and surface albedo in our model are oversimplified. Using more realistic Earth observation datasets, e.g. using SeaWinds scatterometer observations for surface wind speed distribution, Moderate Resolution Imaging Spectroradiometer (MODIS) observations for cloud and surface albedo distribution, could further improve our simulations.

Our work on terrestrial glints also has potential applications to exoplanet studies. Kopparla et al. (2018) show that due to polarized reflected starlight from the ocean, the polarization signal of an exoplanet can be very strong if the exoplanet has widespread oceans. Using a global climate model, Yang et al. (2013) show that a tidally locked exoplanet could have a thick, planet-sized cloud near the substellar location. If horizontally oriented ice crystals broadly exist in clouds, the disk-integrated phase curves of the exoplanet could be prominently altered. Jiang et al. (2018) shows that cloud changes can cause significant variation of single-pixel, disk-integrated light from potential exoplanet observations. Since the size of terrestrial glints is very small compared to the size of the Earth and since we only have single-pixel, disk-integrated exoplanet observations at present, it is currently not possible to determine the existence of glint signals from current observations. With the development of new observing techniques, we might have multi-pixel, direct imaging

exoplanet observations in the future, which could possibly enable us to find glint signals on exoplanets. The detection of specularly reflecting materials is critical in the search for liquid water and possible life on exoplanets.

4.7 Acknowledgements

The DSCOVR data can be downloaded from the following site https://eosweb.larc.nasa.gov/project/dscovr/dscovr_epic_11a_2. This study was partly supported by the Exoplanetary Science Initiative at the Jet Propulsion Laboratory, California Institute of Technology, under a contract with NASA. P. K. and Y. L. Y. acknowledge support by the Virtual Planetary Laboratory, University of Washington. We acknowledge the DSCOVR project science team for support, especially Dr. Jay Herman for help with SEV calculations.

References

- Bi, L., Yang, P., Kattawar, G. W., and Kahn, R. (2010). Modeling optical properties of mineral aerosol particles by using nonsymmetric hexahedra. *Applied optics*, 49(3), 334-342.
- Bodhaine, B. A., Wood, N. B., Dutton, E. G., and Slusser, J. R. (1999). On Rayleigh optical depth calculations. *Journal of Atmospheric and Oceanic Technology*, 16(11), 1854-1861.
- Breon, F.-M., and B. Dubrulle (2004), Horizontally oriented plates in clouds. *Journal of the atmospheric sciences*, 61, 2888–2898.
- Cox, C., and Munk, W. (1954), Measurement of the roughness of the sea surface from photographs of the sun's glitter. *Journal of the atmospheric sciences*, 44(11), 838-850.
- Geogdzhayev, I. V., and Marshak, A. (2018), Calibration of the DSCOVR EPIC visible and NIR channels using MODIS Terra and Aqua data and EPIC lunar observations. *Atmospheric Measurement Techniques*, 11(1), 359-368.
- Herman, J., Huang, L., McPeters, R., Ziemke, J., Cede, A., and Blank, K. (2018), Synoptic ozone, cloud reflectivity, and erythemal irradiance from sunrise to sunset for the whole earth as viewed by the DSCOVR spacecraft from the earth–sun Lagrange 1 orbit. *Atmospheric Measurement Techniques*, 11(1), 177.

- Horak, H. G. (1950). Diffuse reflection by planetary atmospheres. *The Astrophysical Journal*, 112, 445-463
- Jiang, J.H. et al. (2018), Using Deep Space Climate Observatory measurements to study the Earth as an exoplanet. *Astronomical Journal*, 156, 10.3847/1538-3881/aac6e2.
- Kopparla, P., Natraj, V., Zhang, X., Swain, M. R., Wiktorowicz, S. J., and Yung, Y. L. (2016), A multiple scattering polarized radiative transfer model: Application to HD 189733b. *The Astrophysical Journal*, 817(1), 32-43.
- Kopparla, P., Natraj, V., Crisp, D., Bott, K., Swain, M. R., Yung, Y. L. (2018), Observing oceans in tightly packed planetary systems: Perspectives from polarization modeling of the TRAPPIST-1 system. *The Astrophysical Journal*, accepted.
- Marshak, A., Várnai, T., and Kostinski, A. (2017), Terrestrial glint seen from deep space: Oriented ice crystals detected from the Lagrangian point, *Geophysical Research Letters*, 44, 5197–5202, doi:10.1002/2017GL073248.
- Monahan, A. H. (2006), The probability distribution of sea surface wind speeds. Part II: Dataset intercomparison and seasonal variability. *Journal of Climate*, 19(4), 521-534.
- Noel, V., and H. Chepfer (2004), Study of ice crystal orientation in cirrus clouds based on satellite polarized radiance measurements. *Journal of the Atmospheric Sciences*, 61, 2073–2081.
- Noel, V., and H. Chepfer (2010), A global view of horizontally oriented crystals in ice clouds from Cloud-Aerosol Lidar and Infrared Pathfinder Satellite Observation (CALIPSO). *Journal of Geophysical Research: Atmospheres*, 115, D00H23, doi:10.1029/2009JD012365.
- Sagan, C., W. R. Thompson, R. Carlson, D. Gurnett, and C. Hord (1993), A search for life on Earth from the Galileo spacecraft. *Nature*, 365, 715–721.
- Sassen, K., Wang, Z., and Liu, D. (2008). Global distribution of cirrus clouds from CloudSat/Cloud-Aerosol lidar and infrared pathfinder satellite observations (CALIPSO) measurements. *Journal of Geophysical Research: Atmospheres*, 113(D8).
- Spurr, R. J. (2006), VLIDORT: A linearized pseudo-spherical vector discrete ordinate radiative transfer code for forward model and retrieval studies in multilayer multiple scattering media. *Journal of Quantitative Spectroscopy and Radiative Transfer*, 102(2), 316-342.

Yang, J., Cowan, N. B., and Abbot, D. S. (2013), Stabilizing cloud feedback dramatically expands the habitable zone of tidally locked planets. *The Astrophysical Journal Letters*, 771(2), L45-50.

Yang, P., Wei, H., Huang, H. L., Baum, B. A., Hu, Y. X., Kattawar, G. W., Mishchenko, M. I. and Fu, Q. (2005). Scattering and absorption property database for nonspherical ice particles in the near-through far-infrared spectral region. *Applied optics*, 44(26), 5512-5523.

Zhou, C., Yang, P., Dessler, A. E., Hu, Y., and Baum, B. A. (2012), Study of horizontally oriented ice crystals with CALIPSO observations and comparison with Monte Carlo radiative transfer simulations. *Journal of Applied Meteorology and Climatology*, 51(7), 1426-1439.

ROTATION PERIOD DETECTION FOR EARTH-LIKE EXOPLANETS

This chapter is adapted from work previously published as

Li, J., Jiang, J. H., Yang, H., Abbot, D. S., Hu, R., Komacek, T. D., Bartlett, S. J., & Yung, Y. L. (2021). Rotation period detection for Earth-like exoplanets. *The Astronomical Journal*, 163(1), 27. <https://doi.org/10.3847/1538-3881/ac36ce>.

5.1 Abstract

A terrestrial planet's rotation period is one of the key parameters that determines its climate and habitability. Current methods for detecting the rotation period of exoplanets are not suitable for terrestrial exoplanets. Here we demonstrate that, under certain conditions, the rotation period of an Earth-like exoplanet will be detectable using direct-imaging techniques. We use a global climate model that includes clouds to simulate reflected starlight from an Earth-like exoplanet and explore how different parameters (e.g., orbital geometry, wavelength, time resolution) influence the detectability of the planet's rotation period. We show that the rotation period of an Earth-like exoplanet is detectable using visible-wavelength channels with time-series monitoring at a signal-to-noise ratio >20 with ~ 5 to 15 rotation periods of data, while the rotation period of a planet with full ocean coverage is unlikely to be detectable. To better detect the rotation period, one needs to plan the observation so that each individual integration would yield a $S/N > 10$, while keeping the integration time shorter than $1/6$ to $1/4$ of the rotation period of the planet. Our results provide important guidance for rotation period detection of Earth-like exoplanets in reflected light using future space telescopes.

5.2 Introduction

Since the rotation rate of a planet determines the magnitude of its Coriolis force, and therefore strongly influences its atmospheric and oceanic circulation, it is one of the key parameters that determines the climate of a planet (Showman et al., 2013; Forget and Leconte, 2014; Kaspi and Showman, 2015; Komacek and Abbot, 2019). Moreover, as a result of cloud feedbacks, previous simulations suggest that a slowly rotating Earth-like planet could maintain a habitable climate at nearly twice the incident stellar flux as Earth, which implies a strong dependence of the inner edge of the habitable zone on planetary rotation rate (Yang et al., 2014; Way et al., 2016). Therefore, detecting the rotation period of an exoplanet is crucial for evaluating its habitability. Furthermore, the rotation period of an exoplanet will evolve towards the orbital period due to tidal forces exerted by the star it orbits, especially for potentially habitable exoplanets in close-in orbits around low-mass stars (Kasting et al. 1993). Barnes (2017) calculated that approximately half of the habitable Kepler planets and most of the habitable Transiting Exoplanet Survey Satellite (TESS) planets should be tidally locked within 1 Gyr. Detecting the rotation period of an exoplanet, and determining whether it is tidally locked, will therefore put constraints on the age of an exoplanetary system.

A number of methods are currently being used to detect the rotation period of exoplanets. The first method is to use the rotational broadening and Doppler shift of lines in the planetary atmosphere to determine the rotational velocity of the exoplanet. For example, Snellen et al. (2014) used the CO spectrum to constrain the rotational velocity of the gas giant β Pictoris b and Brogi et al. (2016) used the CO and H₂O spectra to constrain the rotational velocity of HD 189733b. The second method is to infer the rotation period of an exoplanet from the magnetic-field-induced radio emission from the extrasolar system. For example, Hess and Zarka (2011) modeled the dynamic radio spectra from an exoplanet and its parent star to show that physical information about the system, including the magnetic field and the rotation period of the exoplanet, can be obtained from radio observations.

These two methods are optimal for hot Jupiters and directly imaged wide-separation gas giants, which are likely to have high rotation rates, strong absorption of certain gases, or

strong magnetic fields. However, these methods are not suitable for detecting the rotation period of Earth-like exoplanets. In the foreseeable future, the most promising strategy for detecting the rotation period of an Earth-like exoplanet is to analyze the single-pixel observations of reflected starlight from the exoplanet, which can be used to retrieve surface features (Jiang et al., 2018; Fan et al., 2019; Aizawa et al., 2020; Gu et al., 2021). Although the reflected starlight of an Earth-like exoplanet will be extremely faint compared to its star, high-contrast imaging capabilities such as a coronagraph or starshade (an external occulter in a telescope designed to suppress the light from the star; Cash, 2006; Vanderbei et al., 2007) will allow us to directly image Earth-like exoplanets. For example, in an overview of the noise budget of starshade-assisted exoplanet imaging, Hu et al. (2021) showed that for some nearby stars (for example, tau Ceti and epsilon Indi A), a signal-to-noise ratio of 20 in a narrow spectral band can be achieved for an Earth-size planet in the habitable zone of its host star with an integration time of several hours using a HabEx-like telescope. The integration time would be shorter for a wider bandpass. It should therefore be feasible to detect the rotation period of Earth-like exoplanets in the near future.

In this study, we explore the detectability of the rotation period of an Earth-like exoplanet. We use the exoplanetary community atmospheric model (ExoCAM) global climate model (GCM) to simulate the atmospheric dynamics and radiative transfer for an Earth-like exoplanet with different rotation periods. Using the simulation results, we mimic future observations of an exoplanet and study which parameters of the exoplanet determine the detectability of its rotation period. We also explore the orbital geometry, wavelength, time duration, and frequency of simulated observations. We describe the ExoCAM model setup in Section 5.4. In Section 5.5, we show how we mimic exoplanet observations and obtain the rotation period from them. We investigate the influence of different parameters on the detectability of the rotation period in Section 5.5. We present a summary and discussion in Section 5.6.

5.3 ExoCAM GCM

We use the global climate model (GCM) ExoCAM (Wolf & Toon, 2015; Kopparapu et al., 2016, 2017; Wolf et al., 2017; Wolf, 2017) to simulate the atmosphere of Earth-like exoplanets. ExoCAM is modified from the Community Atmosphere Model version 4 (CAM4). It uses correlated-k radiative transfer with updated spectral coefficients using the HITRAN 2012 database and a novel treatment of water vapor continuum absorption. Crucially for this project, ExoCAM provides radiative output in 68 wavelength bins. ExoCAM calculates variable clouds as functions of time and space. We use the Rasch and Kristjánsson (1998) subgrid parameterization and the Zhang and McFarlane (1995) convection. ExoCAM has previously been used for a wide variety of studies of the atmospheric circulation and climate of terrestrial exoplanets, including cloud behavior (Wolf & Toon, 2015; Kopparapu et al., 2016, 2017; Wolf et al., 2017; Wolf, 2017; Haqq-Misra et al., 2018; Komacek & Abbot, 2019; Yang et al., 2019a, May et al., 2021).

Since there is nothing special about Earth's rotation period (one day), we conduct two GCM experiments which are equivalent except that they have different rotation periods (one day and two days). Each simulation has an Earth-like ocean-land distribution, planetary radius, surface gravity, obliquity (23.5°), orbital eccentricity (0.0167) and orbital period. The atmosphere is composed purely of nitrogen gas, N_2 . The irradiation is equivalent to that of Earth (1360 W/m^2) and the incident stellar spectrum is the same as the Sun's. The ocean is simulated with a 50-meter-deep slab-ocean model with thermodynamic sea ice (Bitz et al. 2012). We use a horizontal grid of $4^\circ \times 5^\circ$ with 40 vertical layers (Komacek & Abbot 2019). The experiments have a typical duration of approximately 15 years with a time step of 15 minutes. We run the simulations until the annual and global-mean temperature converges, then we output 2-hourly averaged radiation data over a range of wavenumbers (1 cm^{-1} - 42087 cm^{-1}). In what follows, we simulate reflected starlight observations with the output from these two GCM experiments.

5.4 Deriving the Rotation Period from Reflected Light Time Series

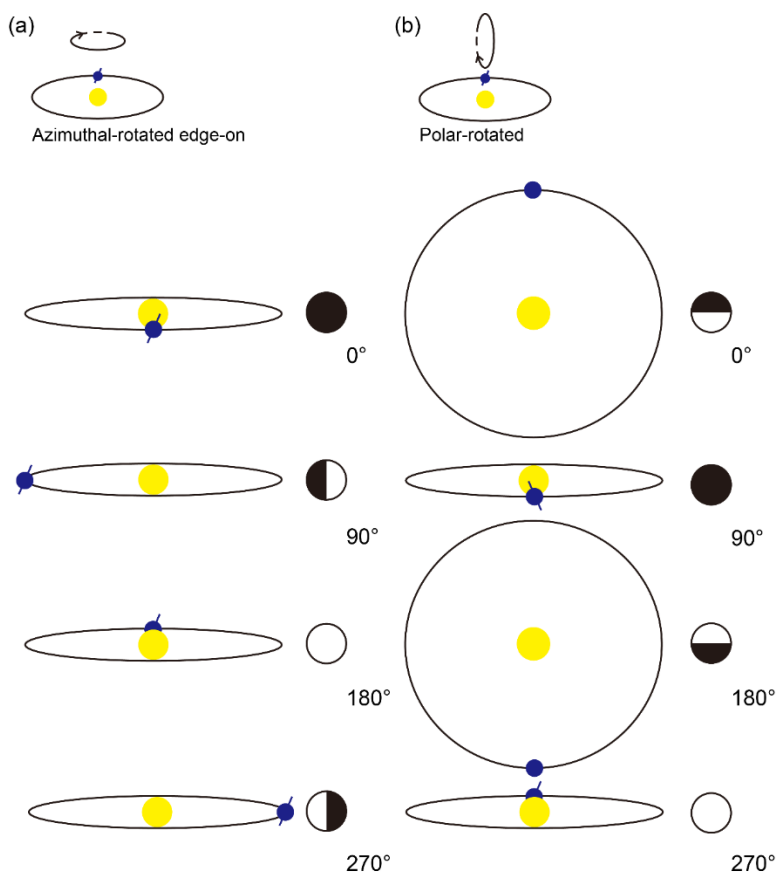


Figure 5.1: Two divergent sets of orbital geometries used in this study. On the top of each panel, the small diagram shows how we rotate the orbit to obtain different orbital geometries. The diagrams below show the correspondence between the angles and the orbital geometries. (a) The exoplanet is in an azimuthal-rotated edge-on orbit. (b) The exoplanet is in a polar-rotated orbit. The markers next to each diagram represent the orientation of the sunlit disc in the view of the observer.

We calculate the disc-averaged reflected stellar flux of the simulated exoplanet to mimic a real observation. The ExoCAM simulation provides us with the reflected stellar flux as a function of wavelength, latitude, and longitude. To calculate a time series of the disc-averaged flux, we first need to pick an orbital geometry. It should be noted that any orbital geometry is possible for an unknown exoplanet. Therefore, we use two divergent sets of orbital geometries in our analysis (Figure 5.1). In the first set of orbital geometries, the orbit of the exoplanet is edge-on in the perspective of the observer (hereafter referred as azimuthal-rotated edge-on orbit). The transit configuration is defined as 0° , while the secondary eclipse

configuration is defined as 180° (see Figure 5.1a). In the second set of orbital geometries (hereafter referred to as polar-rotated orbit), the orbit of the exoplanet is polarly rotated starting from a face-on orbit. The face-on orbit with the northern/southern hemisphere exposed to the observer is defined as $0^\circ/180^\circ$, while the transit and secondary eclipse configurations are defined as 90° and 270° , respectively (see Figure 5.1b). We note that azimuthally and polarly rotating an orbit will generate all possible orbital geometries. It should also be noted that we pick the orbital geometry at the start of the time series. Because of the revolution of the planet, the immediate orbital geometry will change with time. Once an orbital geometry and a specific wavelength range are chosen, a time series of the disc-averaged reflected solar flux can be calculated from the simulation results. The original resolution of the time series is 2 hours, which is the same as the time resolution of the model output. By averaging nearby data points, the resolution of the time series can be arbitrarily decreased. We also add simulated Gaussian observational errors to the time series in order to mimic real observations.

Figure 5.2a presents an example of a time series of simulated reflected starlight created from model output. In this case, we use the 1-Earth-day rotation period simulation output in the wavelength range between 540 nm and 550 nm and the length of the time series is 25 days. The orbital geometry at $t = 0$ is set at 220° of the azimuthal-rotated edge-on orbit and the time resolution is 2 hours. The standard deviation of the observational error is set to be 5% of the disc-averaged flux, which approximately corresponds to a signal-to-noise ratio of 20 for the telescope. We also show the detrended time series, the Fast Fourier transform (FFT) of the detrended time series, and the signal-to-noise ratio in Figure 5.2. The signal-to-noise ratio, which is the power density of the signal divided by the variance of the normally distributed observational error (Scargle 1982), is calculated from the time series (shown in Figure 5.2d). To report a signal with high confidence (low false alarm probability), the signal-to-noise ratio must exceed a certain threshold. In Figure 5.2d, the red line represents the 99% confidence signal-to-noise ratio threshold calculated according to Scargle (1982). It should be noted that this threshold is a function of the length of the time series. Based on Figure 5.2d, there are two signals detected with $>99\%$ confidence ($<1\%$ false alarm probability).

The periods of the highest and the second highest peaks are 1.0 day and 0.5 day, respectively. The 1.0-day signal corresponds to the rotation period while the 0.5-day signal corresponds to possible periodic patterns associated with land-ocean contrast or cloud distribution. It is possible for the highest peak to occur at 0.5 day, 0.33 day or even 0.25 day rather than 1.0 day. Therefore, we propose the following algorithm to obtain the rotation period from a time series:

- (1) Pick the highest peak in the FFT result, then check if the signal-to-noise ratio of this peak is above the 99% confidence threshold.
- (2) If not, then we consider that the rotation period cannot be detected from this time series. If yes, then check if there is another peak that is above the signal-to-noise threshold and has the period that is an integral multiple of the period of the highest peak.
- (3) If not, the rotation period we detect is the period of the highest peak. If yes, the rotation period we detect is this integral multiple of the period of the highest peak.
- (4) Finally, check if the rotation period we detect is the actual rotation period of the simulated exoplanet. If yes, we consider that the rotation period can be detected from this time series.

Figure 5.3 contains a flowchart illustrating our algorithm. With steps (1) to (4), we can determine whether the rotation period of the exoplanet can be detected from a simulated time series. When we alter the parameters of the simulated observation (e.g., orbital geometry, wavelength range, etc.), the time series and the detectability of the rotation period change. In the next section, we will explore how different parameters influence the detectability of the rotation period of an Earth-like exoplanet.

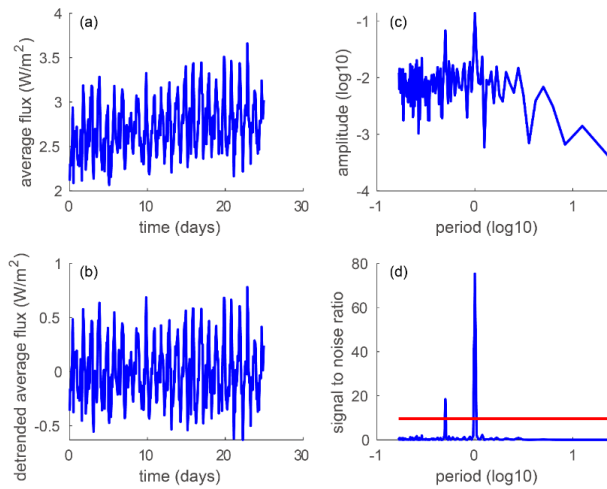


Figure 5.2: How we derive the rotation period from a time series. (a) A simulated time series of reflected star light for the 1-day rotation period experiment. (b) The detrended time series. (c) Fourier transform of the detrended time series. (d) Signal-to-noise ratio as a function of period. The red line indicates the signal-to-noise threshold for 99% confidence.

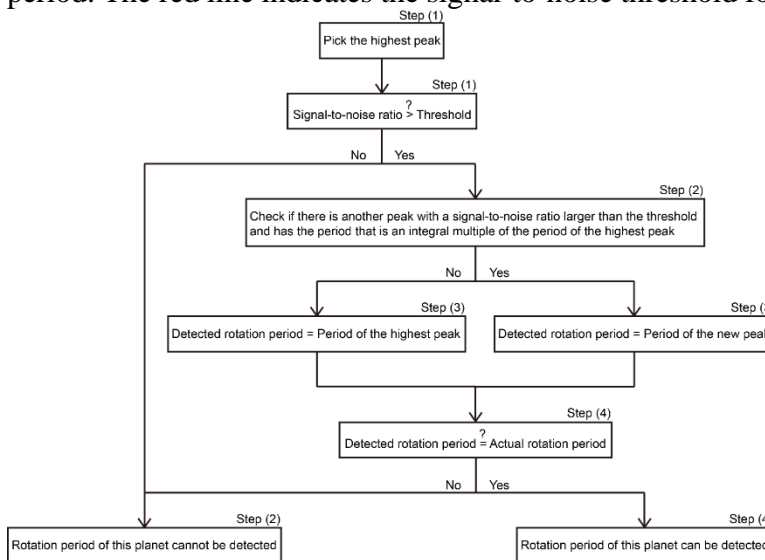


Figure 5.3: The flowchart of the algorithm that is used to determine whether the rotation period of the exoplanet can be detected from a simulated time series.

5.5 Sensitivity of the Detectability of the Rotation Period to Parameters

To understand the conditions under which the rotation period of an Earth-like exoplanet is likely to be detectable, here we consider 7 important factors that affect the observations.

5.5.1 Length of Observation

We find that it is generally easier to detect the rotation period with longer lengths of observation. Figure 5.4 shows a time series that is obtained under the same condition as the time series in Figure 5.2 except that the length of this time series is only 4 days. From Figure 5.4d, we clearly see that this time series does not meet our criteria for rotation period detection. Therefore, under a given condition, the minimum length of observation needed to detect the real rotation period is a key parameter that measures the detectability of the rotation period.

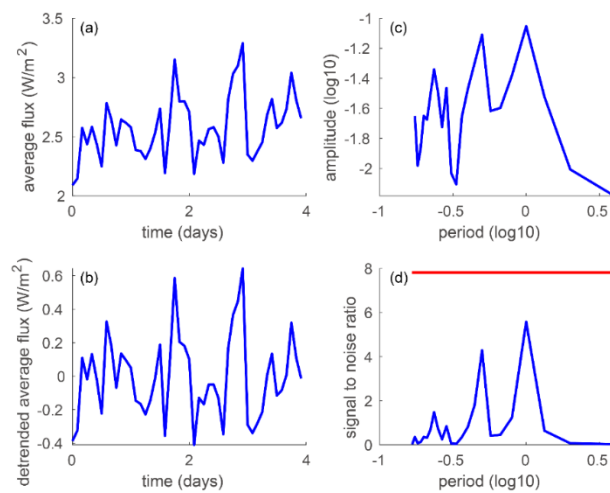


Figure 5.4: As Figure 5.2, except the length of the time series is 4 days. The 99% confidence threshold in panel (d) is lower than the threshold in Figure 5.2d due to the shorter time series.

5.5.2 Rotation Period

Since the detectability of the rotation period depends on how many periods are contained in the time series, the minimum length of observation needed to detect the rotation period should be measured in periods instead of days. In Section 5.4, we used 1 per 2 hours, 1 per 4 hours, etc. to represent the time resolution of the time series. Since hour and day are Earth-specific units, a more sophisticated way to describe the time resolution is the number of data points in one period. In other words, 1 per 2 hours for a 1-day rotation period and 1 per 4 hours for a 2-day rotation period dataset are equivalent, each corresponding to 12 data points per period. Ideally the minimum observation length needed to detect the rotation period should be a constant number of rotational periods. However, our analysis shows that sometimes the minimum length of observation (in rotational periods) needed for the 1-day

rotation period dataset and the minimum length of observation needed for the 2-day rotation period dataset are not always equal due to the differing climates. In what follows we will regard the minimum length of observation needed to detect the rotation period under a given condition as the larger minimum length of observation obtained from the two datasets.

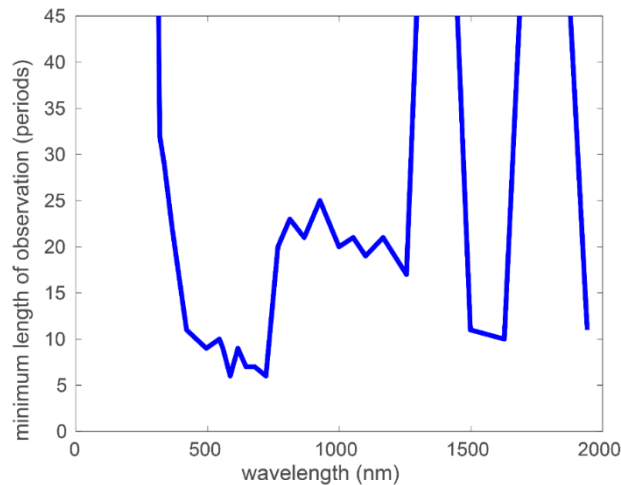


Figure 5.5: An example of the minimum length of observation needed to detect the rotation period as a function of wavelength. We combine 1- and 2-day period data here (see Section 5.5.2) and use a 99% confidence threshold. The orbital geometry is 180° of the azimuthal-rotated edge-on orbit, the time resolution 12 data points per period, and the observational error is 5%.

5.5.3 Wavelength

The detectability of the rotation period may vary with the wavelength used to observe the exoplanet. Here we fix the orbital geometry at 180° of the azimuthal-rotated edge-on orbit, the time resolution at 12 data points per period and the observational error at 5%. We then calculate the minimum length of observation needed to detect the rotation period for different wavelength ranges (Figure 5.5). If the rotation period cannot be obtained from an observational length of 45 rotation periods, we consider the rotation period to not be detectable under this condition. In Figure 5.5, we can see that the minimum length of observation needed in the visible channels (500 to 700 nm) is less than 10 periods, much shorter than the minimum length of observation needed for the ultraviolet and near-infrared channels. This is mainly because the reflectance of land, ocean and cloud are more diverse in the visible channels than in other channels (Xu et al., 2015; Kokaly et al., 2017).

5.5.4 Orbital Geometries

If the exoplanet is near secondary eclipse, the observer can see almost the entire sunlit disc (as long as the star is not blocking the planet), which will provide a smooth variation in reflected light. If the exoplanet is near transit, the observer can see very little reflected starlight from the exoplanet, which will make the variation in reflected light rather random. Therefore, the orbital geometry clearly influences the detectability of the rotation period. In the following, we fix the time resolution at 12 data points per period and the observational error at 5%, then find the minimum length of observation needed to detect the rotation period as a function of wavelength and orbital geometry (shown in Figure 5.6). For the near infrared channels below $1.3 \mu\text{m}$, in a range of $\sim 100^\circ$ in both azimuthal and polar angle around the secondary eclipse, the rotation period is detectable with ~ 20 -30 periods of observation. In the visible channels, the rotation period is detectable with less than 15 periods of observation in a much larger geometry range. As expected, the rotation period of the exoplanet is only difficult to detect near transit. For the ultraviolet channels with wavelengths above 285 nm, the rotation period is detectable near the secondary eclipse with more than 25 periods of observation. The rotation period is undetectable at wavelengths less than 285 nm. In Figure 5.6a, we can see that the most detectable/undetectable orbital geometries are not exactly at secondary eclipse/transit. That is because the orbital geometry is picked at $t = 0$ and will change due to the revolution of the planet.

5.5.5 Time Resolution

To evaluate the influence of time resolution on the detectability of the rotation period, we repeat the analysis from Section 5.5.4 with coarser time resolutions of 6 data points per period (Figure 5.7a), 4 data points per period (Figure 5.7b), and 3 data points per period (Figure 5.7c). With 6 data points per period, the rotation period is still detectable in a large geometry range in visible channels, but the minimum length of observation needed to detect the rotation period becomes about 2 times longer than the higher resolution scenario (Figure 5.7a). In contrast, the rotation period becomes undetectable at other wavelengths. If the time resolution is decreased to 3 data points per period, the rotation period is only detectable near transit (Figure 5.7c). This is consistent with Jiang et al. (2018), who showed that when the

time resolution is lower than 2 data points per period, the probability of detecting the rotation period drops dramatically regardless the total observation length.

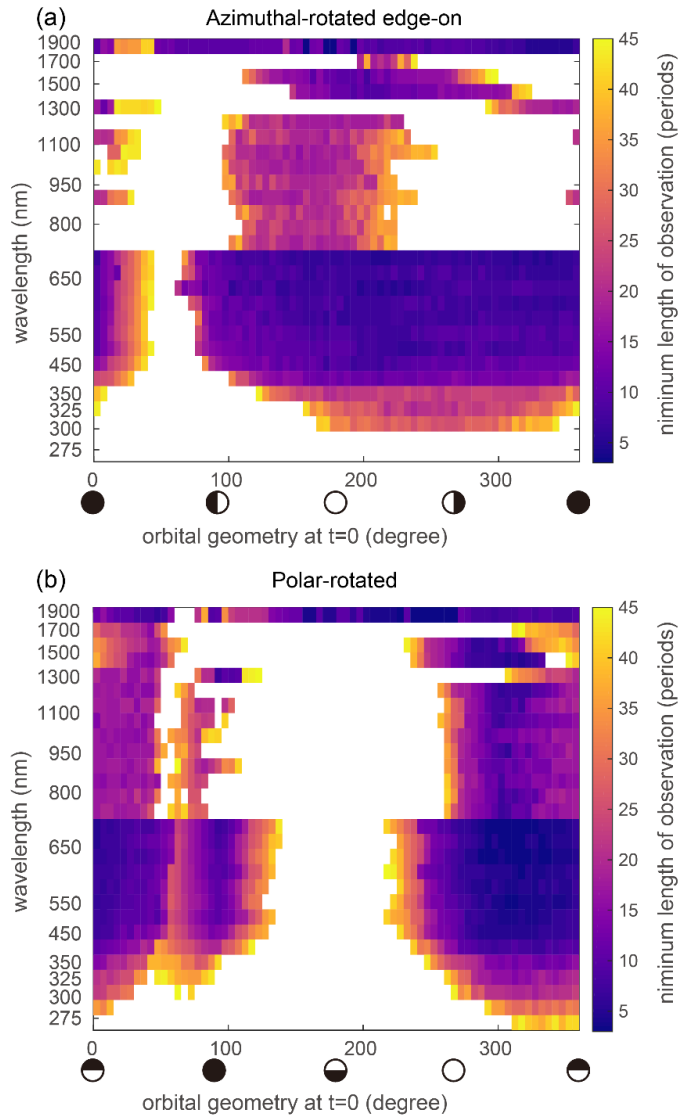


Figure 5.6: The minimum length of observation needed to detect the rotation period as functions of the wavelength and orbital geometry. We combine 1- and 2-day period data here (see Section 5.5.2) and use a 99% confidence threshold. The time resolution is 12 data points per period. The observational error is 5%. (a) Azimuthal-rotated edge-on orbital geometries (see Figure 5.1). (b) Polar-rotated orbital geometries. The color white indicates that the rotation period is not detectable.

5.5.6. Observational Error

In the previous analysis, we fixed the standard deviation of the observational error added to the time series at 5% of the disc-averaged flux, which approximately corresponds to a signal-

to-noise ratio (S/N) of 20 for each integration. To evaluate the influence of the S/N on the detectability of the rotation period, we recreate our analysis from Section 5.5.4, but change the S/N to 40 and 10 (Figure 5.8). When the S/N is 40, the detectability is significantly enhanced in all channels (Figure 5.8a). In the visible and near-infrared channels, the minimum length of observation needed to detect the rotation period is less than 10 periods for most of the orbital geometries. Moreover, even the ultraviolet channels at wavelengths below 285 nm become detectable. On the contrary, when the S/N is 10 (Figure 5.8b), the rotation period is undetectable for most of the ultraviolet and near-infrared channels. Although the rotation period is still detectable for the visible channels, it requires more than 20 to 25 periods of observation.

5.5.7 Land Fraction

The fractions of land and ocean on Earth's northern hemisphere are comparable, whereas on Earth's southern hemisphere the ocean covers more than 80% of the surface. Therefore, the southern hemisphere of the Earth is more like an aqua planet (i.e., a planet with full ocean coverage). We can exploit this asymmetry to investigate how land fraction influences the detectability of the rotation period. For example, when the observer focuses on the northern hemisphere (around 0° of the second set of orbital geometries), the rotation period is detectable for most of the channels (Figure 5.6b). In contrast, when the observer focuses on the southern hemisphere (around 180° of the second set of orbital geometries), the rotation period becomes undetectable. This result implies that the rotation period of an exoplanet with no land is unlikely to be detected using the observational technique outlined here. In other words, an exoplanet whose rotation period can be detected is likely to have a mix of continents and ocean, which may be used to infer information about the planet's geophysical and geochemical context that would otherwise be hidden.

5.6 Conclusion and Discussion

In this study, we simulate observations of ExoCAM output, a GCM that includes clouds, to evaluate the detectability of a terrestrial exoplanet's rotation period through an FFT analysis of reflected starlight. Our work shows that to better detect the rotation period, one needs to

plan the observation so that each individual integration would yield a $S/N > 10$, while keeping the integration time shorter than $1/6 - 1/4$ of the rotation period of the planet. The best wavelength range to carry out this observation will be between $500 - 700$ nm, and in this wavelength range, the rotation period may be obtained with an observation campaign that lasts for ~ 10 rotation periods. Using Earth as an analog, the quantities above correspond to repeating the integration every $< 4 - 6$ hours for ~ 10 days. There are trade-offs between the integration time (and thus the S/N per integration) and the total duration of the observation. The optimal timing of this type of observation will be when the planet moves into an orbital phase where much of the planetary surface is illuminated by starlight.

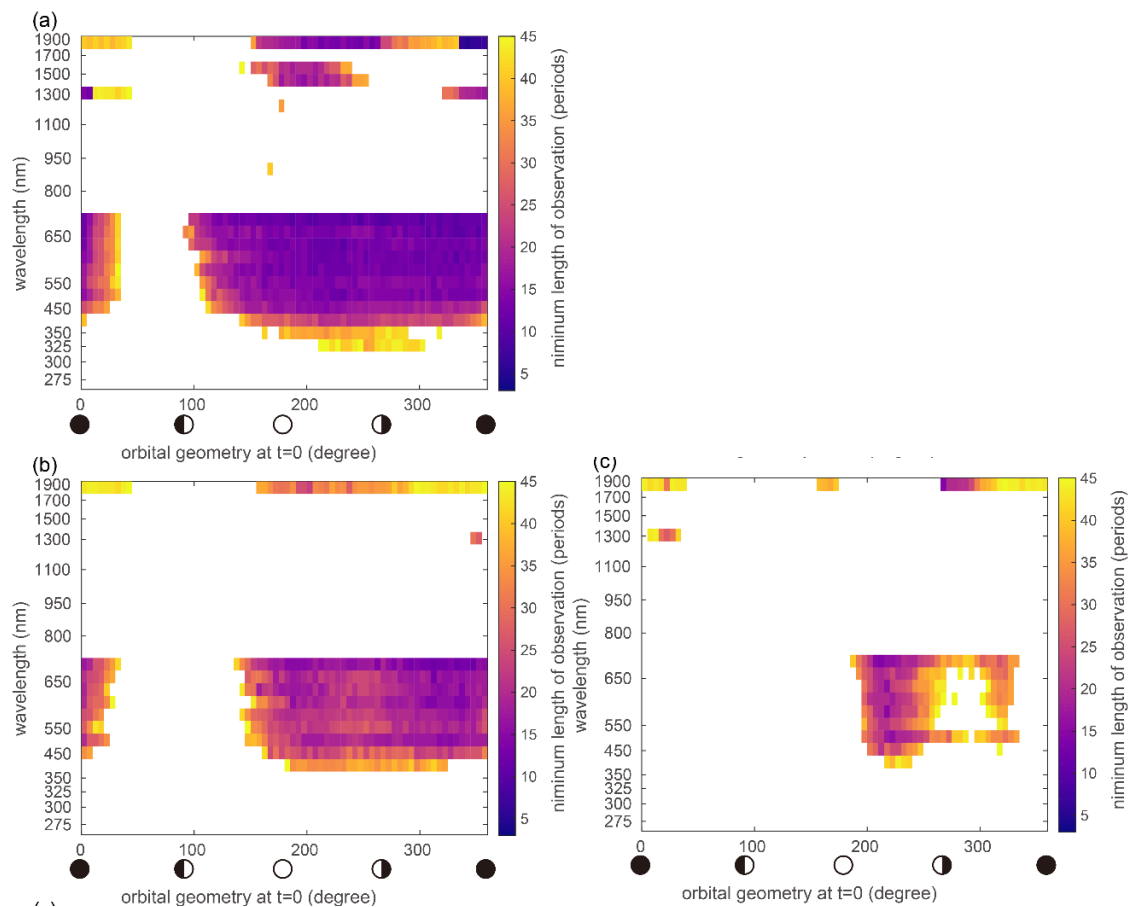


Figure 5.7: Exploration on time resolution. (a) Same as Figure 5.6a, except that the time resolution is 6 data points per period. (b) Same as Figure 5.6a, except that the time resolution is 4 data points per period. (c) Same as Figure 5.6a, except that the time resolution is 3 data points per period.

When dealing with a real observation, since we would not know the rotation period, one should follow the steps in Section 5.4 to get a preliminary rotation period from the observed time series. With the preliminary rotation period, the observer will be able to convert the time resolution to units of number per period and the length of the time series to a multiple of the rotation periods. By comparing the parameters of the observation (time resolution, S/N, length of observation, etc.) to the parameter space explored in Section 5.5, one can tell whether this preliminary rotation period is likely to be the true rotation period or not.

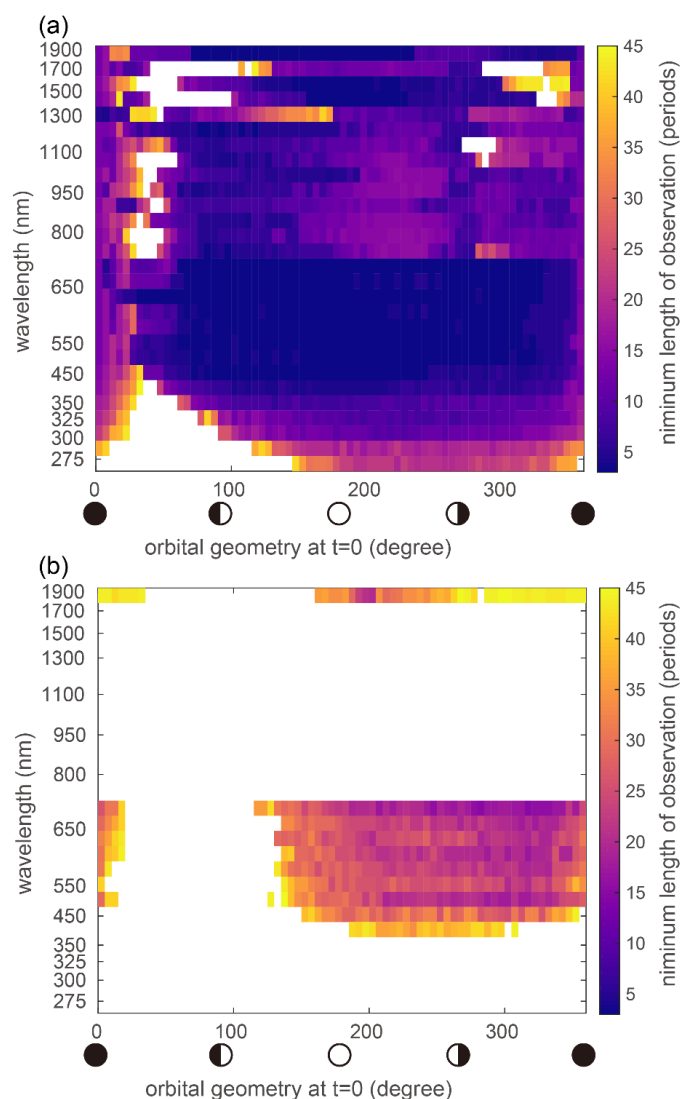


Figure 5.8: Exploration on S/N. (a) Same as Figure 5.6a, except that the S/N is 40. (b) Same as Figure 5.6a, except that the S/N is 10.

Future space telescopes being planned may provide the required conditions to detect the rotation periods of terrestrial planets in the habitable zone of some nearby stars. For example, a HabEx-like telescope would achieve an $S/N=20$ per 5-nm spectral channel in 500 – 700 nm for an Earth-like planet in the habitable-zone of the nearest stars (distance $< 4\text{pc}$, e.g., tau Ceti, epsilon Indi A) in ~ 10 hours (Hu et al., 2021). This translates to an integration time of ~ 6 hours per ~ 10 -nm spectral channel, corresponding to the simulation shown in this paper. The rotation period would thus be detectable if Earth analogs are found in these systems and ~ 10 days of the mission time are dedicated to the campaign. Given the importance of the rotation period (it is one of the basic planetary parameters aside from mass and radius) and possible science that can be achieved at the same time (e.g., surface composition mapping, Cowan et al., 2009; Fan et al., 2019), a ~ 10 -day campaign may be favorable. The requirement will be less stringent for planets larger than Earth or closer to their host star, for which the endeavor of detecting the planetary rotation period may be extended to stars further away. A larger space telescope (e.g., the LUVOIR mission concept) would enable rotation period detection in more systems.

The detectability of rotation period is mainly due to the differences between the reflectance of ocean, land, and persistent cloud. In general, clouds block land and ocean from the observer, making the rotation period more difficult to detect. In a test run, we removed the cloud from the simulated planet and found that the minimum length of observation needed to detect the rotation period was shorter than it was for the cloud-covered planet. While the impact of clouds is essential, the modeling of clouds is highly uncertain (Yang et al., 2019b). Future work exploring alternative cloud schemes is needed. For Earth-like exoplanets, since the planet is not entirely covered by cloud, its surface features can be seen by the observer so that the rotation period is detectable. For exoplanets with more substantial cloud coverage than Earth, the rotation period may become undetectable. For example, Lee et al. (2020) found that a periodogram analysis of the light curve of Venus reveals two strong signals at 3.7 and 4.6 days, which correspond to the rotation of the atmosphere rather than the rotation of Venus itself.

In Section 5.5.7, we proposed that the rotation period of an aqua exoplanet is likely undetectable. However, this is based on the precondition that we only have photometric observations of the exoplanet. Ocean glint, which has been shown to facilitate surface mapping of potential habitable exoplanets (Lustig-Yaeger et al., 2018), is highly polarized. Kopparla et al. (2018) model the polarization signal of the TRAPPIST-1 system and show that the polarization signal from an ocean-covered exoplanet is stronger and easier to detect than the intensity signal. Since the polarization observation of an aqua exoplanet is dependent on the surface roughness of the ocean, a non-uniform surface roughness distribution of the aqua exoplanet could cause diurnal variation in a polarization observation. If a direct-imaged polarization observation of an exoplanet were available, the rotation period of an aqua exoplanet might still be detectable. In concert with photometric observations, a polarization observation may also improve the detectability of the rotation period of Earth-like exoplanets.

In this paper, we have studied fast-rotating exoplanets, whose rotation period is much smaller than its orbital period. For Venus-like, slowly-rotating exoplanets whose rotation period is comparable to their orbital period, the variation of the reflected starlight caused by its rotation would be coupled with the variation caused by its revolution so that the signal of the rotation period may be hard to detect. Further studies are required to address this problem.

In summary, we find that it will be possible to detect the rotation period of a terrestrial exoplanet using direct imaging if the planet is observed in favorable conditions. The detection of the rotation period of Earth-like exoplanets will help us identify habitable exoplanets and provide us with information on the dynamical evolution of exoplanetary systems.

5.7 Acknowledgements

We thank Eric Wolf for developing, maintaining, and making publicly available ExoCAM. This work is supported by the Jet Propulsion Laboratory, California Institute of Technology, under contract with NASA. We acknowledge the funding support from the NASA Exoplanet

Research Program NNH18ZDA001N-2XRP. This work is also supported by the NASA Astrobiology Program grant No. 80NSSC18K0829 and benefited from participation in the NASA Nexus for Exoplanet Systems Science research coordination network. This work was completed with resources provided by the University of Chicago Research Computing Center. T. D. K. acknowledges support from the 51 Pegasi b fellowship in Planetary Astronomy sponsored by the Heising-Simons Foundation. Y. L. Y. was supported in part by an NAI Virtual Planetary Laboratory grant from the University of Washington (YLY.001377-1-JPL.1616476).

References

- Aizawa, M., Kawahara, H., & Fan, S. (2020). Global mapping of an exo-Earth using sparse modeling. *The Astrophysical Journal*, 896, 22.
- Barnes, R. (2017). Tidal locking of habitable exoplanets. *Celestial Mechanics and Dynamical Astronomy*, 129, 509.
- Bitz, C. M., Shell, K. M., Gent, P. R., et al. (2012). Climate sensitivity of the community climate system model, version 4. *Journal of Climate*, 25, 3053.
- Brogi, M., De Kok, R. J., Albrecht, S., et al. (2016). Rotation and winds of exoplanet HD 189733 b measured with high-dispersion transmission spectroscopy. *The Astrophysical Journal*, 817, 106.
- Cash, W. (2006). Detection of Earth-like planets around nearby stars using a petal-shaped occulter. *Nature*, 442, 51.
- Fan, S., Li, C., Li, J. Z., et al. (2019). Earth as an exoplanet: A two-dimensional alien map. *The Astrophysical Journal Letters*, 882, L1.
- Forget, F., & Leconte, J. (2014). Possible climates on terrestrial exoplanets. *Philosophical Transactions of the Royal Society A: Mathematical, Physical and Engineering Sciences*, 372, 20130084.
- Gu, L., Fan, S., Li, J., et al. (2021). Earth as a proxy exoplanet: Deconstructing and reconstructing spectrophotometric light curves. *The Astronomical Journal*, 161, 122.

- Haqq-Misra, J., Wolf, E. T., Joshi, M., et al. (2018). Demarcating circulation regimes of synchronously rotating terrestrial planets within the habitable zone. *The Astrophysical Journal*, 852, 67.
- Hess, S. L. G., & Zarka, P. (2011). Modeling the radio signature of the orbital parameters, rotation, and magnetic field of exoplanets. *Astronomy & Astrophysics*, 531, A29.
- Hu, R., Lisman, D., Shaklan, S., et al. (2021). Overview and reassessment of noise budget of starshade exoplanet imaging. *Journal of Astronomical Telescopes, Instruments, and Systems*, 7, 021205.
- Jiang, J. H., Zhai, A. J., Herman, J., et al. (2018). Using deep space climate observatory measurements to study the Earth as an exoplanet. *The Astronomical Journal*, 156, 26.
- Kaspi, Y., & Showman, A. P. (2015). Atmospheric dynamics of terrestrial exoplanets over a wide range of orbital and atmospheric parameters. *The Astrophysical Journal*, 804, 60.
- Kasting, J. F., Whitmire, D. P., & Reynolds, R. T. (1993). Habitable zones around main sequence stars. *Icarus*, 101, 108.
- Kokaly, R. F., Clark, R. N., Swayze, G. A., et al. (2017). *USGS spectral library version 7* (No. 1035). US Geological Survey.
- Komacek, T. D., & Abbot, D. S. (2019). The atmospheric circulation and climate of terrestrial planets orbiting Sun-like and M dwarf stars over a broad range of planetary parameters. *The Astrophysical Journal*, 871, 245.
- Kopparapu, R. K., Wolf, E. T., Haqq-Misra, J., et al. (2016). The inner edge of the habitable zone for synchronously rotating planets around low-mass stars using general circulation models. *The Astrophysical Journal*, 819, 84.
- Kopparapu, R. K., Wolf, E. T., Arney, G., et al. (2017). Habitable moist atmospheres on terrestrial planets near the inner edge of the habitable zone around M dwarfs. *The Astrophysical Journal*, 845, 5.
- Kopparla, P., Natraj, V., Crisp, D., et al. (2018). Observing oceans in tightly packed planetary systems: Perspectives from polarization modeling of the TRAPPIST-1 system. *The Astronomical Journal*, 156, 143.

- Lee, Y. J., Muñoz, A. G., Imamura, T., et al. (2020). Brightness modulations of our nearest terrestrial planet Venus reveal atmospheric super-rotation rather than surface features. *Nature Communications*, *11*, 1.
- Lustig-Yaeger, J., Meadows, V. S., Mendoza, G. T., et al. (2018). Detecting ocean glint on exoplanets using multiphase mapping. *The Astronomical Journal*, *156*, 301.
- May, E. M., Taylor, J., Komacek, T. D., et al. (2021). Water ice cloud variability and multi-epoch transmission spectra of TRAPPIST-1e. *The Astrophysical Journal Letters*, *911*, L30.
- Rasch, P. J., & Kristjánsson, J. E. (1998). A comparison of the CCM3 model climate using diagnosed and predicted condensate parameterizations. *Journal of Climate*, *11*, 1587.
- Scargle, J. D. (1982). Studies in astronomical time series analysis. II-Statistical aspects of spectral analysis of unevenly spaced data. *The Astrophysical Journal*, *263*, 835.
- Showman, A. P., Wordsworth, R. D., Merlis, T. M., et al. (2013). Atmospheric circulation of terrestrial exoplanets. *Comparative Climatology of Terrestrial Planets*, *1*, 277.
- Snellen, I. A., Brandl, B. R., de Kok, R. J., et al. (2014). Fast spin of the young extrasolar planet β Pictoris b. *Nature*, *509*, 63.
- Vanderbei, R. J., Cady, E., & Kasdin, N. J. (2007). Optimal occulter design for finding extrasolar planets. *The Astrophysical Journal*, *665*, 794.
- Way, M. J., Del Genio, A. D., Kiang, N. Y., et al. (2016). Was Venus the first habitable world of our solar system? *Geophysical Research Letters*, *43*(16), 8376-8383.
- Wolf, E. T., & Toon, O. B. (2015). The evolution of habitable climates under the brightening Sun. *Journal of Geophysical Research: Atmospheres*, *120*, 5775.
- Wolf, E. T., Shields, A. L., Kopparapu, R. K., et al. (2017). Constraints on climate and habitability for Earth-like exoplanets determined from a general circulation model. *The Astrophysical Journal*, *837*, 107.
- Wolf, E. T. (2017). Assessing the habitability of the TRAPPIST-1 system using a 3D climate model. *The Astrophysical Journal Letters*, *839*, L1.
- Xu, M., Pickering, M., Plaza, A. J., et al. (2015). Thin cloud removal based on signal transmission principles and spectral mixture analysis. *IEEE Transactions on Geoscience and Remote Sensing*, *54*, 1659.

- Yang, J., Boué, G., Fabrycky, D. C., et al. (2014). Strong dependence of the inner edge of the habitable zone on planetary rotation rate. *The Astrophysical Journal Letters*, 787, L2.
- Yang, J., Abbot, D. S., Koll, D. D., et al. (2019a). Ocean dynamics and the inner edge of the habitable zone for tidally locked terrestrial planets. *The Astrophysical Journal*, 871, 29.
- Yang, J., Leconte, J., Wolf, E. T., et al. (2019b). Simulations of water vapor and clouds on rapidly rotating and tidally locked planets: A 3D model intercomparison. *The Astrophysical Journal*, 875, 46.
- Zhang, G. J., & McFarlane, N. A. (1995). Role of convective scale momentum transport in climate simulation. *Journal of Geophysical Research: Atmospheres*, 100, 1417.